8-2014

Investigation of Concurrent Energy Harvesting from Ambient Vibrations and Wind

Amin Bibo
Clemson University, abibo@clemson.edu

Investigation of Concurrent Energy Harvesting from Ambient Vibrations and Wind

---

A Dissertation
Presented to
the Graduate School of
Clemson University

In Partial Fulfillment
of the Requirements for the Degree
Doctor of Philosophy
Mechanical Engineering

---

by
Amin S. Bibo
August 2014

Accepted by:
Dr. Mohammed Daqaq, Committee Chair
Dr. Ardalan Vahidi
Dr. Gang Li
Dr. Richard Figliola

Abstract

In recent years, many new concepts for micro-power generation have been introduced to harness wasted energy from the environment and maintain low-power electronics including wireless sensors, data transmitters, controllers, and medical implants. Generally, such systems aim to provide a cheap and compact alternative energy source for applications where battery charging or replacement is expensive, time consuming, and/or cumbersome.

Within the vast field of micro-power generation, utilizing the piezoelectric effect to generate an electric potential in response to mechanical stimuli has recently flourished as a major thrust area. Based on the nature of the ambient excitation, piezoelectric energy harvesters are divided into two major categories: the first deals with harvesting energy from ambient vibrations; while the second focuses on harvesting energy from aerodynamic flow fields such as wind or other moving fluids. This Dissertation aims to investigate the potential of integrating both sources of excitation into a single energy harvester. To that end, the Dissertation presents reduced-order models that can be used to capture the nonlinear response of piezoelectric energy harvesters under the combination of external base and aerodynamic excitations; and provides approximate analytical solutions of these models using perturbation theory. The analytical solutions are used, subsequently, to identify the important parameters af-

fecting the response under the combined loading and to develop an understanding of the conditions under which the combined loading can be used to enhance efficacy and performance. As a platform to achieve these goals, the Dissertation considers two energy harvesters; the first consisting of a piezoelectric cantilever beam rigidly attached to a bluff body at the free end to permit galloping-type responses, while the second consists of a piezoelectric cantilever beam augmented with an airfoil at its tip. The airfoil is allowed to plunge and pitch around an elastic axis to enable flutter-type responses. Theoretical and experimental studies are presented with the goal of comparing the performance of a single integrated harvester to two separate devices harvesting energy independently from the two available energy sources.

It is demonstrated that, under some clearly identified conditions, using a single piezoelectric harvester for energy harvesting under the combined loading can improve its transduction capability and the overall power density. Even when the wind velocity is below the cut-in wind speed of the harvester, i.e. galloping or flutter speed, using the integrated harvester amplifies the influence of the base excitation which enhances the output power as compared to using one aeroelastic and one vibratory energy harvesters. When the wind speed is above the cut-in wind speed, the performance of the integrated harvester becomes dependent on the excitation's frequency and its magnitude with maximum improvements occurring near resonance and for large base excitation levels.

Dedication

To my wonderful parents, who made all of this possible, for their endless love, encouragement, and patience.

Acknowledgments

First and foremost, I thank God for all the blessings he bestowed on me during my life, and for giving me such a great opportunity, along with the patience and enthusiasm necessary to complete this Ph.D dissertation.

Secondly, I especially thank my Thesis advisor, Dr. Mohammed F. Daqaq, for his invaluable support and advice throughout my time in Clemson. I am very blessed to have him as a friend and a mentor. I thank him for patiently teaching me innumerable lessons pertinent to research and also for motivating and inspiring me towards new possibilities of life. Without his thorough guidance, the completion of this work would not have been possible.

I thank my advising committee members Dr. Gang Li, Dr. Ardalan Vahidi and Dr. Richard Figliola for their encouraging and constructive feedback. I also thank all the professors I have taken courses with: Dr. Mohammed Daqaq, Dr. Nader Jalili, Dr. Gang Li, Dr. Ardalan Vahidi, Dr. Hyesuk Lee, Dr. Jan Medlock, Dr. Earl Wagener, Dr. Beshaw Ayalew, Dr. Georges Fadel, Dr. Brian Fralix, and Dr. Robert Lund.

I acknowledge the generous support of National Science Foundation and the Department of Mechanical Engineering at Clemson University for providing the necessary funding to pursue my research.

Sincere thanks also go to the Departmental staff for their excellent work and endless help in the last six years.

I feel privileged to have been surrounded by brilliant colleagues -Dr. Yousef Qaroush, Dr. Ravindra Masana, Dr. James Gibert, Dr. Gregory Batt, Shyam Panyam, Clodoaldo Silva, Thiago Seuaciuc-Osrio, Christopher Stabler, Tugba Demir, Qifan He, Yuhao Wang, Xiyuan Liu, Amanda King, Donovan Bode, Michael Lacour, Raveen Kumar, Saad Alazemi, Abdaouf Abusoua, and Ali Alhadidi. I thank all of them for making my life as a graduate student a memorable one.

Without doubt, my deepest gratitude goes to my family, without whom, I would not have been able to reach this point: My father, Mr. Saleh Bibo, and my mother Mrs. Ietedal Bibo, for their endless love, kindness, support, encouragement, and continuous care. My brothers and sisters, Amani, Eman, Amneh, Ala, Arwa, Ayman, and Ashraf for their endless love and encouragement.

Special thanks are due to the following persons: Dr. Mohammed Al-Nimr for being more than a brother and for his continuous encouragement and belief in me; Dr. Yousef Qaroush for his great friendship and endless help. I also would like to give my gratitude for my roommates over the last six years: Dr. Jouad Meziani, Dr. Ali Al-Ahmar, Mr. Khaled Trabelsi, Mr. Mahmoud Abdel-Hamid, Mr. Malek Aljamaliah, and Mr. Nidal Alzboun.

Finally, I take this opportunity to express my very sincere gratitude to Ms. Dorothy Puma, Randie Puma, Ashlie Puma, and Jessie Puma for their family-like support, generous care and the home feeling whenever i was in need during my stay in Clemson.

Table of Contents

List of Figures

List of Tables

Chapter 1

Introduction

1.1 Motivations

Only a decade ago, the concept of micropower generation would have been ridiculed because output power levels in the range of a few microwatts to several milliwatts were considered unusable. However, today and as a result of recent advances in circuit design and micro-fabrication technologies, many critical electronics, such as health-monitoring sensors [1, 2], pace makers [3], spinal stimulators [4], electric pain relievers [5], wireless sensors [6, 7, 8], micro-electromechanical systems [9, 10], etc., require minimal amounts of power to function. For instance, a wireless transponder for data transmission can operate efficiently with less than 1 mW of power [11, 12]. A sensor interface chip for health monitoring that consists of a sensor and a microcontroller has an average power consumption of 48 μW [13, 14]. Such devices have, for long time, relied on batteries that have not kept pace with the devices' demands, especially in terms of energy density [15]. In addition, batteries have a finite life span, adverse environmental impacts, and require regular replacement or recharging, which, in many

of the previously mentioned examples, is a very cumbersome and expensive process. One area that is currently suffering from battery technology's shortcomings is active implantable medical devices [16]. The long-anticipated artificial pancreas to treat diabetes operates on batteries that must be replaced every nine months posing a significant risk of infection that can claim lives, thereby rendering this life-saving technology inefficient. Other devices, like cochlear ear implants are too small to contain batteries [16].

In light of such challenges, scavenging otherwise wasted energy from the environment can provide a solution to lower our dependence on batteries and advance many life-saving technologies. While the process of harnessing energy, also known as energy harvesting, is not new and has been historically practised by humans in the form of windmills, sailing ships, and waterwheels; today, and due to many recent and critical advances in manufacturing electronics that made low-power consumption devices a reality; researchers are taking this same old approach into new domains where the goal is to design compact and scalable generators that can harvest minute amounts of energy to run and maintain low-power consumption electronics [17, 18, 19].

1.2 Current Approaches for Micro-power Generation

To power, maintain, and allow autonomous operations of low-power consumption devices, the concept of micro-power generators (MPGs) was introduced [20, 21, 22, 23, 24]. Micro-power generators are essentially compact and scalable energy harvesting devices that can transform wasted ambient energy, e.g., thermal, solar, wind, and vi-

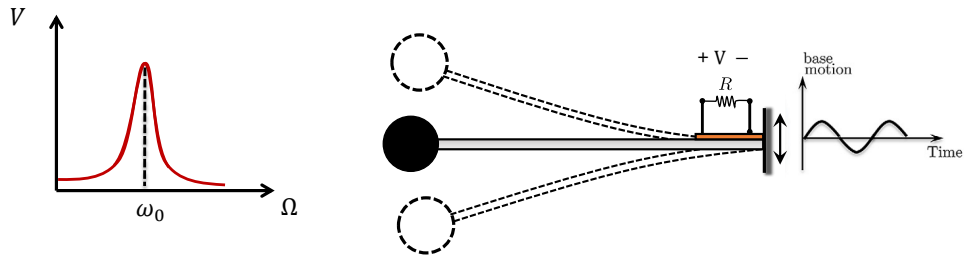

Figure 1.1: Schematic of a piezoelectric vibratory energy harvester and its associated linear frequency response.

brations into electricity. Among such approaches, vibratory energy harvesting (VEH) has flourished as a major thrust area. Various devices have been developed to transform mechanical motions directly into electricity by exploiting the ability of active materials and some mechanisms (such as piezoelectric, magnetostrictive, ferroelectric, electrostatic, and electromagnetic) to generate an electric potential in response to mechanical stimuli and external vibrations [17, 18, 19]. However, the concept of VEH has a critical shortcoming in its operation. Specifically, as shown in Fig. 1.1, vibratory energy harvesters operate efficiently only within a narrow frequency bandwidth where the excitation frequency, Ω, is very close to the fundamental frequency of the harvester, ω_0 (resonance condition). Small variations in the excitation frequency around the harvester's fundamental frequency drop its small energy output even further making the energy harvesting process inefficient [25, 26, 27, 28, 29, 30]. This issue becomes even more pressing when one realizes that most environmental excitations have a broad-band or time-dependent characteristics in which the energy is distributed over a wide spectrum of frequencies or the dominant frequencies drift with time. As such, many viable excitation sources such as structural and machine vibrations, ocean waves, acoustic excitations, running, walking, among other motions are considered impractical due to their inherent randomness or non-stationarities.

Several investigations on modeling and analyzing the response under harmonic and random excitations have been performed to improve the performance of VEHs by maximizing the output power and more importantly achieving a broad frequency bandwidth. Different techniques have been employed for this purpose including magnetic coupling, multi degree-of-freedom harvesting, and bistable configurations [31, 32, 33, 34, 35, 36].

Another approach for micro-power generation which has been receiving a growing interest in recent years is flow energy harvesting (FEH). This new research field aims to provide efficient, scalable, and easy to fabricate harvesters that outperform small-scale wind turbines. Unfortunately, traditional wind turbine designs that are based on rotary-type generation concepts are known to suffer from two critical problems. First, they have scalability issues because their performance drops significantly as their size decreases. Mitcheson et al. [37] reported that the power coefficient can drop from 0.59 which corresponds to the Betz limit to less than 0.1 as the size of the turbine gets smaller. This is a result of *i*) relatively high viscous drag on the blades at low Reynolds numbers [38], *ii*) bearing and thermal losses which increase significantly as size decreases, and *iii*) high electromagnetic interferences. In addition to performance issues, design and fabrication of traditional small-scale rotary-type generators that require a rotor, a stator, magnets, wirings, and blades is a very complex and expensive process. This makes their actual implementation for compact applications such as those mentioned previously a difficult task.

The basic principle of FEH lies in replacing rotary type generators by simpler yet more efficient designs that can channel energy from a moving fluid to a mechanical oscillator by coupling the dynamic forces culminating from the motion of the fluid past the oscillator to its natural modes of vibration. As a result of this coupling, the oscillator

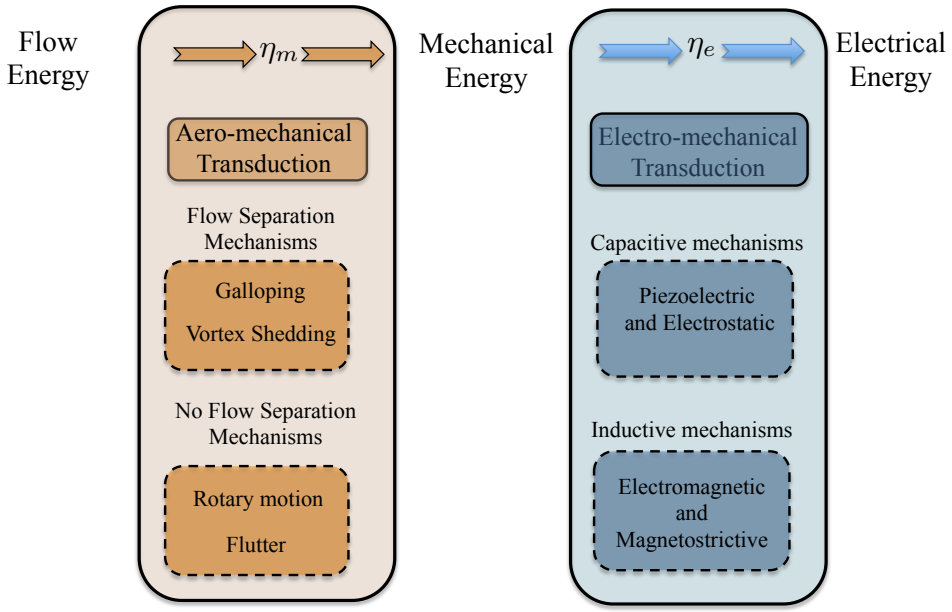

Figure 1.2: An overview of flow energy harvesting.

undergoes large amplitude motion which can be transformed into electricity using an electromechanical transduction mechanism, e.g., piezoelectric, electromagnetic, or electrostatic. An overview of the mutual interaction between the fluid, mechanical, and electrical domains can be seen in Fig. 1.2. In the first stage, the kinetic energy of the moving fluid is converted into strain energy in the elastic structure in the form of large amplitude oscillations. These oscillations, arise from distinct fluid-dynamic phenomena/instabilities that can be classified by the nature of the flow patterns around the structure. These patterns depend on the characteristics of the structure or the mechanical oscillator such as its shape and dimensions as well as the ongoing flow conditions, e.g., steadiness, velocity, and angle of attack. In the second stage, the elastic energy is converted into electrical energy via an electro-mechanical transduction mechanism.

In general, the efficacy of a FEH mechanism depends on the strength of the coupling

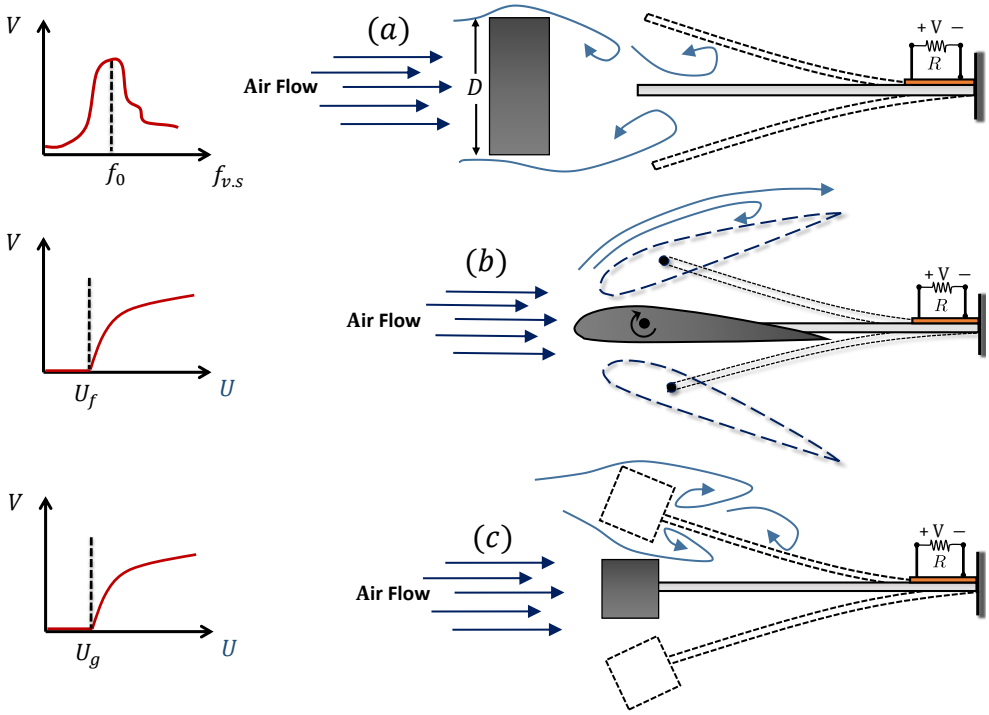

Figure 1.3: Several widely-used mechanisms for flow energy harvesting: (a) vortex-induced vibrations, (b) flutter, and (c) galloping.

between the dynamic fluid forces and the restoring forces of the oscillator (harvester). This coupling determines the portion of the kinetic energy of the flow which is converted into elastic energy, and subsequently transformed into electricity. Figure 1.3 depicts three different coupling mechanisms for piezoelectric FEH in uniform and steady flow. The first approach is known as wake-galloping or vortex-induced vibrations and is based on placing the harvester– here a flexible cantilever beam with piezoelectric laminate attached to a resistive load, R– in the wake of a bluff body. When the flow separates on the bluff body, vortices are shed from first one side and then the other forming the so called Kármán vortex street. As the vortices move downstream, surface pressures are imposed on the beam as shown in Fig. 1.3 (a). The oscillating pressures cause the beam to vibrate in a periodic manner at a fre-

quency equals the vortex shedding frequency which is given by $f_{v.s} = S_t U/D$, where S_t is the Strouhal number and D is the cross-flow frontal dimension of the body. The output power, in this case, is also a function of the vortex shedding frequency which is proportional to the wind speed. The maximum output power occurs at the wind speed for which the shedding frequency matches or locks onto the first modal frequency of the piezoelectric beam, f_0. Away from that frequency, the output power drops significantly similar to the resonant behavior of vibratory energy harvesters as shown in Fig. 1.3 (a).

The second approach represents energy harvesting through a two-degree-of-freedom instability known as flutter. The harvesting beam, in this case, is attached to an airfoil section which is allowed to plunge in the vertical direction and to pitch about an elastic axis. In general, the two-degree-of-freedom motion is coupled inertially, and aerodynamically through an instantaneous angle of attack which includes the effects of both torsion and plunge of the airfoil. This generates lift and moment loads on the airfoil. When the airflow approaches the wind speed of the flutter instability, U_f, at which the energy input by the aerodynamic loading balances the energy dissipated by the damping, the two modal frequencies of the plunge and the pitch degrees-of-freedom converge to form a single frequency-coupled mode allowing self-sustained oscillations to emerge. The steady-state amplitude of these oscillations increases as the wind speed is increased as shown in Fig. 1.3 (b).

The third approach is known as galloping and can be treated as a special case of flutter. In this case, a bluff body which is only allowed to plunge or translate vertically is attached to the free end of the piezoelectric beam representing a one degree-of-freedom instability. The incoming flow generates a drag force on the bluff body and as the flow separates on both sides, inner circulation flow forms under the two shear

layers. This circulation produces surface pressures which causes a net lift on the body. As the wind speed exceeds the onset speed of galloping, U_g, the resulting aerodynamic loads overcome the intrinsic damping in the system causing the structure to vibrate transversally. The motion of the structure increases the effective angle of attack which, in turn, increases the aerodynamic loading. This increasing load then amplifies the oscillations resulting in a self-feeding or sustained vibrations that build up until its limited by the hardening nonlinearities. As the wind speed is further increased, the amplitude of the self-sustained oscillations increases as shown in Fig. 1.3 (c).

Just like vibration-based energy harvesting, several investigations have been carried out on flow energy harvesting employing the previous mechanisms of aerodynamic loading: wake-galloping [39, 40, 41], galloping [42, 43, 44, 45, 46, 47], and flutter [48, 49, 50, 51, 52]. Other configurations have also been designed using two or more harvesters each with a cylindrical bluff body placed in a tandem arrangement such that the downstream harvester can oscillate in the wake of an upstream harvester as in [53].

From performance perspective, the attachment of the airfoil or prismatic structure to the flexible piezoelectric beam as in the second and third approaches increases the aeroelastic coupling due to the fact that the dynamic loads on the tip body are transmitted directly to the beam. This improves the fluid-elastic conversion efficiency by two orders of magnitude larger than the vortex-induced vibrations case as reported in [45]. Another advantage is that, for flutter-based and galloping harvesters, the onset of instability is followed by a monotonic increase in the output power of the harvester as the wind speed is increased. Therefore, the harvester does not exhibit the resonant behavior typical of wake-galloping oscillators. As such, it is obvious that FEH using the first mechanism is not preferred. In fact, in the third approach, and depending

Figure 1.4: The I-35W Mississippi River bridge collapse. Picture taken by Kevin Rofidal, United States Coast Guard.

on the size and the shape of the tip body and the associated Strouhal's number, a harvester can experience vortex-induced and galloping oscillations separately or in combination.

1.3 Thesis Objectives

While previous research studies have only considered one source of excitation, i.e., vibratory or flow excitations, the primary objective of this thesis is to investigate the potential of integrating both sources of excitation into a single energy harvester. Such device can find potential applications especially for powering wireless electronics where coexisting vibrations and ambient flows are available. One scope of application is the health monitoring of structures such as bridges and aircrafts. During the last two decades, more than 500 bridge failures were reported in the United States [54]. Some of these, similar to the I-35W Mississippi River bridge collapse in 2007,

were sudden catastrophic failures claiming human lives and resulting in millions of dollars in damage as shown in Fig. 1.4. One way to avoid such disasters is to implement an early warning system using structural health-monitoring sensor networks. The sensor nodes provide measurements of performance parameters such as vibration, load, strain, displacement, temperature, corrosion and tilt/inclination. These measurements can then be analyzed to detect structural damage by monitoring slow or sudden changes in the response of structures to various environmental stimuli. Traditionally, information is gathered using sensor nodes that are hard wired to data acquisition systems. However, this conventional approach has many drawbacks including high installation and maintenance costs. In addition, having wires spread all over the structure make them very prone to failure and tampering and could as well disturb the normal operation of the system. To avoid these problems, wireless health-monitoring sensor networks (WHMSN) have been recently proposed and are currently being implemented as a replacement for the older hard-wired systems. Such networks provide similar functionalities of efficient and real-time monitoring and inspection at a much lower cost and, because of the absence of wires, provide higher spatial density of sensor's distribution [55]. It has been recently demonstrated, that the energy harvested from wind loading and vibrations caused by the flow of traffic over bridges, the swaying of a building due to wind, or even earthquakes is feasible to power WHMSN [56, 57].

The thesis contributions towards achieving the primary objective of investigating the concept of concurrent energy harvesting under vibratory and flow inputs can be outlined as follows:

- **Investigating piezoelectric energy harvesting under the combination of base and galloping excitations.** To achieve this goal, *i*) an energy har-

vester which consists of a thin cantilever beam with piezoelectric patch attached to its upper surface is considered. To permit galloping excitation, a bluff body is rigidly attached at the free end of the piezoelectric beam similar to the scenario shown in Fig. 1.3 (c). A nonlinear electromechanical distributed-parameter model of the harvester under the combined excitation is derived using the energy approach and by adopting the nonlinear Euler-Bernoulli beam theory, linear constitutive relations for the piezoelectric transduction, and the quasi-steady assumption for the aerodynamic loading; *ii*) the partial differential equations of the system are discretized and a reduced-order-model is obtained; *iii*) the mathematical model is validated experimentally under different loading conditions represented by wind speed, base excitation amplitude, and excitation frequency around the primary resonance; and *iv*) results of the combined systems are then compared to a scenario where two separate energy harvesters, one VEH and a FEH, are used to independently harvest energy from their respective excitation source. In other words, the VEH is designed to only harvest energy from the available base excitation, while the FEH can only harvest energy from the air flow. Two cases are discussed; the first compares the performance when the wind speed is below the speed of galloping instability, while the second case represents comparison for wind speeds above the galloping speed. Results are presented to determine whether a single integrated harvester can outperform the two separate harvesters and to demonstrate the regions of enhanced performance.

- **Implementing a systematic analysis to understand the role of the design parameters on the performance characteristics of galloping FEH.** It has been observed that the process of improving the performance of FEHs,

which involves minimizing the cut-on wind speed and maximizing the output power, can be very complicated because it requires investigating and optimizing the influence of a myriad of design parameters taking into consideration all of the three constituting domains, i.e. the aerodynamic, structural, and electrical domains. In this thesis, a nonlinear analysis is carried out to obtain an approximate analytical solution that provides a deeper insight into the physics of the problem and an explicit understanding of the effects of the system parameters. Two cases are considered; the first is for a harvester subjected to galloping excitations only, while the second treats a harvester under concurrent galloping and base excitations. In addition to deriving and experimentally validating the analytical approximations, a dimensional analysis is performed to identify the important parameters that affect the system's response in both cases.

- **Investigating piezoelectric energy harvesting under the combination of vibratory base and flutter aeroelastic excitations.** This task is very similar in structure to the first task with the main difference that a flutter based two-degree-of-freedom harvester is used instead of the galloping harvester. *i*) An energy harvester which consists of a rigid airfoil supported by nonlinear flexural and torsional springs is considered. The harvester is placed in an incompressible air flow and subjected to a harmonic base excitation in the plunge direction. To capture the qualitative behavior of the harvester, a five-dimensional lumped-parameter model which adopts nonlinear quasi-steady aerodynamics and accounts for the piezoelectric coupling in the plunge-mode is used; *ii*) a center manifold reduction is implemented to reduce the full model into one nonlinear first-order ordinary differential equation; *iii*) the method of normal form is then utilized to obtain an approximate analytical solution that

can be used to study slow modulation of the response amplitude and phase of the reduced system near the flutter instability. The availability of this solution is essential for in-depth understanding of the effects of the combined loading and of the design parameters on the energy harvesting process. Numerical integration of the five-dimensional equations of motion is a very time-consuming and a cumbersome process which cannot be used solely to draw definitive conclusions about the effects of the design and the excitation parameters; and *iv*) theoretical and experimental results are presented to demonstrate the role of the wind speed, excitation amplitude as well as excitation frequency on the output power.

1.4 Dissertation Outline

The rest of the manuscript is organized as follows:

In Chapter 2, the potential of utilizing a FEH to scavenge energy from combination of vibratory base excitations and aerodynamic loading is investigated. A distributed-parameter nonlinear electromechanical model of a harvester subjected to galloping and harmonic base excitations is derived. A reduced-order model which can be used to obtain an in-depth understanding of the behavior of the system's response in terms of the harvested output power and the excitation parameters is then obtained.

In Chapter 3, experimental results validating the theoretical analysis of the harvester's response to primary resonance excitations are provided for wind speeds below and above the galloping speed.

In Chapter 4, an approximate analytical solution to the dynamic problem of the

harvester subjected to galloping and base excitations is obtained using the method of multiple scales. This solution is validated numerically and experimentally and then utilized in an optimization analysis for the galloping excitation case. Results are presented to provide new insights into the optimal performance conditions.

Chapter 5 investigates the transduction of a piezoaeroelastic energy harvester under the combination of flutter and vibratory base excitations. A five-dimensional lumped-parameter model which adopts nonlinear quasi-steady aerodynamics is used. A center manifold reduction is implemented to reduce the full model into one nonlinear first-order ordinary differential equation. The normal form of the reduced system is then derived to study slow modulation of the response amplitude and phase near the flutter instability.

Finally, Chapter 6 presents the main conclusions and directions for future research.

Chapter 2

Mathematical Modeling Under Galloping and Base Excitations

In this Chapter, we obtain a mathematical model that represents the dynamics of a piezoelectric energy harvester under a combination of vibratory base and galloping excitations. The availability of this model is essential to fully characterize the response behavior of the harvester and to optimize the design parameters for enhanced performance. To achieve this goal, a non-linear distributed-parameter model is derived. Subsequently, a Galerkin descritization is utilized to obtain a reduced-order model of the system.

2.1 Nonlinear Distributed-Parameter Model

As shown in Fig. 5.2, the energy harvester under investigation consists of a thin cantilever beam with a piezoelectric patch bonded to its upper surface. The piezoelectric beam is rigidly attached at the free end to a square-sectioned tip body with a cross-

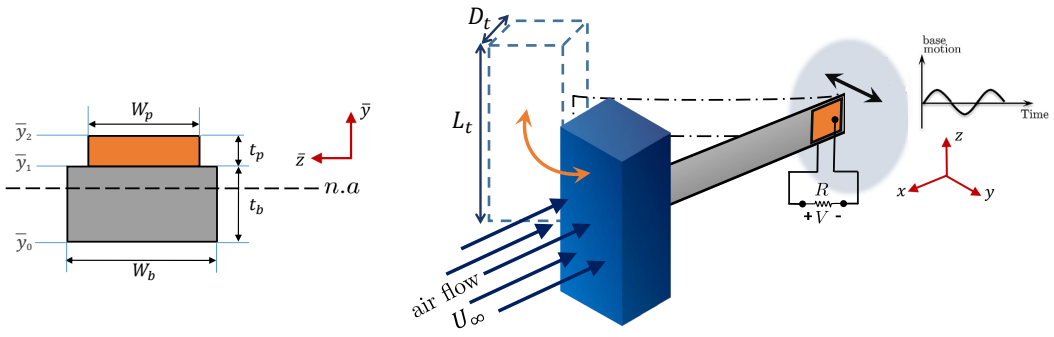

Figure 2.1: A schematic diagram of the energy harvester and piezoelectric beam section.

flow width, D_t, and length, L_t. The harvester is subjected to an external harmonic base motion, y_b, and is placed in a uniform air flow with mean flow speed, U_∞. When the flow speed exceeds the onset speed of galloping, U_*, the harvester can undergo steady-state limit-cycle oscillations in the cross-flow direction, y, in addition to the oscillations induced by the base motion. These oscillations strain the piezoelectric element, which in turn, generates a voltage, V, across an electric load, R.

2.1.1 Strain-Displacement Relationship

This section presents the development of a distributed-parameter model which captures the nonlinear dynamics of the harvester. Towards that end, we start by developing the strain-displacement relationships of the beam. For a slender beam uni-morph similar to the one considered here, shear deformations and rotary inertia can be neglected allowing for the adoption of the nonlinear Euler-Bernoulli's beam theory to model the beam's response. According to Euler's theory, the flexural dynamics of the beam can be described using a longitudinal displacement, $u(s,t)$, and a transversal displacement, $w(s,t)$, as depicted in Fig. 2.2, where, s, denotes the arclength and, t, denotes time. To describe a beam element before and after deformation, two carte-

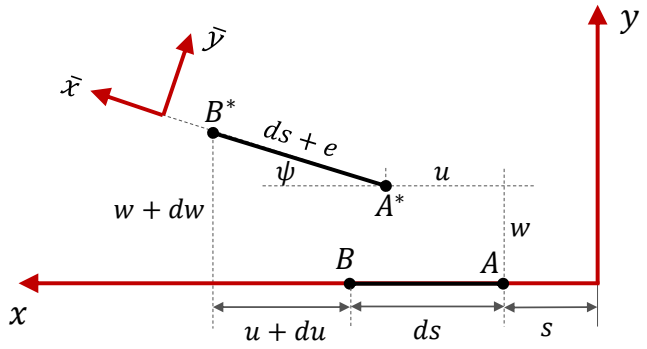

Figure 2.2: Deformation of a differential beam element.

sian coordinate systems are utilized: the (x, y, z) is considered to be global, while the $(\bar{x}, \bar{y}, \bar{z})$ is a local system, and they are related through a transformation matrix corresponding to the rotation around the $\bar{z}$-axis. Using Fig. 2.2, it follows that the longitudinal elongation of the beam element can be written as [58]:

$$e = \sqrt{(ds + du)^2 + dw^2} - ds. \tag{2.1}$$

Dividing Equation (2.1) by the element length, ds, the strain along the neutral axis of the differential element becomes

$$\epsilon_0 = \sqrt{(1 + u')^2 + w'^2} - 1, \tag{2.2}$$

where the over-prime denotes a derivative with respect to the arclength, s. Due to rotation of the differential beam element, the strain at a point located a distance $\bar{y}$ relative to the neutral axis can be written in terms of the beam's curvature as

$$\epsilon_r = -\bar{y}\frac{d\psi}{ds}, \tag{2.3}$$

where, ψ, is the rotation angle of the differential beam element, which can be further related to the beams deflection using

$$\psi = \tan^{-1}\left[\frac{w'}{1+u'}\right], \tag{2.4}$$

Substituting Equation (2.4) into Equation (2.3), and adding the resulting expression to Equation (2.2) yields the total strain at a given point along the beam's thickness. Upon expanding the resulting expression in a Taylor series up to cubic terms, we obtain

$$\epsilon_x = \epsilon_0 + \epsilon_r = u' + \frac{w'^2}{2} - \frac{u'w'^2}{2} - \bar{z}\left[w'' - w''u' - w'u'' - w''w'^2\right]. \tag{2.5}$$

For cantilever beams, with zero geometric boundary condition at one end, it can be safely assumed that the beam is inextensible, i.e. the relative elongation along the neutral axis is equal zero, $\epsilon_0 = 0$, [58]. Using a Taylor series expansion up to quadratic terms, the extensibility condition can be used to relate the longitudinal displacement to the transverse displacement via

$$u' = -\frac{1}{2}w'^2, \text{ or } \quad u = -\frac{1}{2}\int_0^s w'^2 ds. \tag{2.6}$$

2.1.2 Constitutive Relationships

Considering planar bending vibrations, the axial stress, σ_x, and strain, ϵ_x, of the beam and the piezoelectric layer are assumed to, respectively, follow the following linear constitutive relationships:

$$\sigma_x^b = Y^b \epsilon_x^b, \tag{2.7}$$

$$\sigma_x^p = Y^p \left[\epsilon_x^p - d_{31} E_3\right], \tag{2.8}$$

in which, the superscripts/subscripts b and p stand for the structural and piezoelectric layers, respectively; Y is Young's modulus, d_{31} is the piezoelectric constant, and E_3 is the electric field which can be related to the voltage, $V(t)$, developed across a piezoelectric layer of thickness, t_p, according to $E_3 = V(t)/t_p$. Considering a harvesting circuit with a purely resistive electric load, R, the harvested voltage can be related to the current via Ohm's law as $V(t) = R\dot{Q}_R(t)$, where $\dot{Q}_R(t)$ is the current passing through the load and the over-dot indicates a derivative with respect to time. Substituting the aforementioned relations back into Equation (2.8), yields the following constitutive relation for the piezoelectric element:

$$\sigma_x^p = Y^p \left[\epsilon_x^p + \frac{d_{31}}{t_p} R\dot{Q}_R(t)\right]. \tag{2.9}$$

2.1.3 Equations of Motion and Boundary Conditions

To obtain the equations of motion, we use Hamilton's variational principle which states that

$$\int_{t_1}^{t_2} \delta\mathcal{L} + \delta\mathcal{W}^{ext} dt = 0, \tag{2.10}$$

where t_1 to t_2 is any arbitrary time interval, δ is the variational operator, $\mathcal{L} = T - U$ is the Lagrangian, and $\mathcal{W}^{ext}$ is a non-conservative work term. The kinetic energy, T,

of the system can be expressed as

$$T = \frac{1}{2}\int_0^{L_b} M(s)\left\{\left[\frac{\partial}{\partial t}\int_0^s \frac{1}{2}w'^2 ds\right]^2 + \left(\dot{y}_b + \dot{w}\right)^2\right\} ds + \frac{1}{2}I_t\,\dot{w}'\big|_{L_b}{}^2 + \frac{1}{2}M_t\left[\left(\dot{y}_b + \dot{w}|_{L_b} + L_c\,\dot{w}'\big|_{L_b}\right)^2 + \left(\frac{\partial}{\partial t}\int_0^{L_b}\frac{1}{2}w'^2 ds - L_c\,\dot{w}'\big|_{L_b}\,w'|_{L_b}\right)^2\right]. \tag{2.11}$$

The first term in Equation (2.11) represents the translational kinetic energy distributed along the piezoelectric beam and resulting from the beam's relative deflection and base displacement in the transverse y-direction, and the longitudinal deflection in the x-direction. It should be noted that the effect of the beam rotary inertia is neglected in this term since it is of the same order as the effect of shear deformations. The mass per unit length of the beam, $M(s)$, is given by

$$M(s) = m_b + m_p\left[H(s) - H(s - L_p)\right], \quad m_b = \rho^b W_b t_b, \quad m_p = \rho^p W_p t_p,$$

where, ρ, is the mass density, t, W, and L are the associated thickness, width, and length of the layer as shown in Fig. 5.2, and $H(s)$ is the Heaviside function.

The second term in Equation (2.11) represents the rotational kinetic energy of the tip body. Here, the angular velocity is a result of the rotation of the beam at the free end with angle $w'|_{L_b}$, and, I_t, is the moment of inertia of the tip body around its center of mass. Finally, the third term represents the translational kinetic energy of the tip body of mass M_t. The total translational motion of the body's center of mass corresponds to the deflection of the beam at the free end in addition to the motion resulting from the rotation and the offset between the body's center of mass and the

beam's free end, L_c.

The total potential energy of the system, U, consists of the strain energy of the composite beam in addition to the electric potential stored in the capacitive piezoelectric layer. These can be expressed as

$$U = \frac{1}{2}\int_{\mathcal{V}} \left(\sigma_x^b \epsilon_x^b + \sigma_x^p \epsilon_x^p\right) d\mathcal{V} - \frac{1}{2}\int_{\mathcal{V}} E_3 D_3 d\mathcal{V}, \tag{2.12}$$

where, $\mathcal{V}$, is the domain and, D_3, is the electric displacement given by the following linear piezoelectric constitutive relation:

$$D_3 = d_{31} Y^p \epsilon_x^p - e_{33} E_3, \tag{2.13}$$

where e_{33} is the permittivity at constant strain.

Replacing the electric field, E_3, in Equation (2.13) again by $-R\dot{Q}_R/t_p$, then substituting Equations (2.5), (2.6) (2.7), (2.9), and (2.13) back into Equation (2.12), and carrying the integration over the cross-sectional area of each layer, we obtain up to quartic terms:

$$\begin{aligned} U = \frac{1}{2}\int_0^{L_b} \Big\{ YI(s)\left(w''^2 + w''^2 w'^2\right) + \theta(s)\left(w'' + \frac{1}{2}w''w'^2\right) R\dot{Q}_R \Big\} ds \\ + \frac{1}{2} C_p \left(R\dot{Q}_R\right)^2, \end{aligned} \tag{2.14}$$

where $YI(s)$, $\theta(s)$, and C_p are, respectively, the bending stiffness, the electromechan-

ical coupling, and the piezoelectric capacitance

$$\begin{aligned} YI(s) =& \frac{1}{3}\left(W_b Y^b\left(\bar{y}_1^3-\bar{y}_0^3\right)+W_p Y^p\left(\bar{y}_2^3-\bar{y}_1^3\right)\right)\left[H\left(s\right)-H\left(s-L_p\right)\right] \\ &+Y^b I_b\left[H\left(s-L_p\right)-H\left(s-L_b\right)\right], \quad I_b=\frac{W_b t_b^3}{12}, \\ \theta(s) =& \frac{-W_p Y^p d_{31}}{2t_p}\left(\bar{y}_2^2-\bar{y}_1^2\right)\left[H(s)-H(s-L_p)\right], \quad C_p=\frac{e_{33} W_p L_p}{t_p}. \end{aligned}$$

Here, $\bar{y}_0, \bar{y}_1$, and, $\bar{y}_2$, are the thickness boundaries measured from the neutral axis of the beam as depicted in Fig. 5.2. The location of the neutral axis is determined relative to the bottom surface of the composite beam by recalling that stresses through the cross section must be in equilibrium. This yields

$$\bar{y}_0=-\frac{1}{2}\frac{Y^b W_b t_b^2+2Y^p W_p t_p t_b+Y^p W_p t_p^2}{Y^b W_b t_b+Y^p W_p t_p}, \quad \bar{y}_1=t_b+\bar{y}_0, \quad \bar{y}_2=t_p+\bar{y}_1. \tag{2.15}$$

2.1.3.1 Non-Conservative Forces:

The work done by nonconservative forces is divided into three parts, namely, the work done by the aerodynamic lateral force, F_y, the work done by mechanical viscous damping, c_a, and that done to extract the electric energy and dissipate it into the resistive load, R. With that, the nonconservative virtual work term can be expressed as

$$\delta \mathcal{W}^{ext}=F_y\,\delta w|_{L_b}+F_y L_c\,\delta w'|_{L_b}-\int_0^{L_b}\left[c_a\left(\dot{w}+\dot{y}_b\right)\delta w\right]ds-R\dot{Q}_R(t)\delta Q_R, \tag{2.16}$$

To model the aerodynamic forces, F_y, we use the quasi-steady assumption which states that the aerodynamic forces acting on the moving tip body with center velocity, $\dot{y}_t$, are produced by relative wind velocity, U_{rel}, at an effective angle of attack, α, as

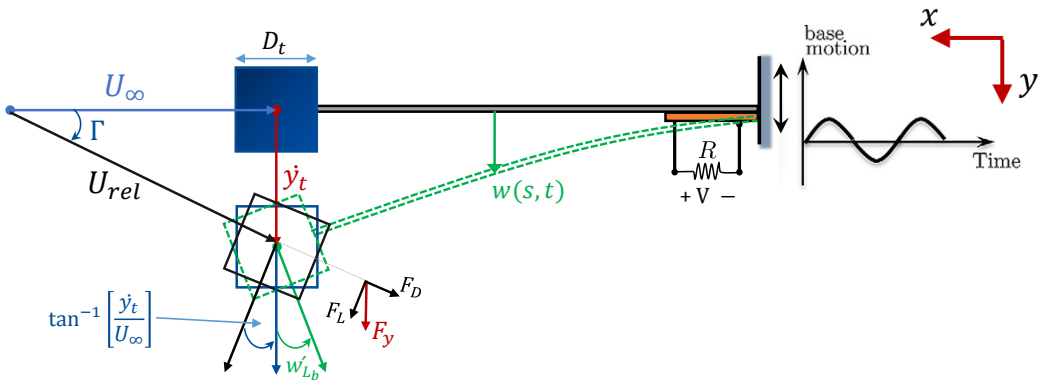

Figure 2.3: Tip body cross section in flow.

shown in Fig 4.3. These are given by

$$U_{rel} = \sqrt{U_\infty^2 + \dot{y}_t^2}, \quad \alpha = \Gamma + w'|_{L_b}, \quad \Gamma = \tan^{-1}\left[\frac{\dot{y}_t}{U_\infty}\right], \tag{2.17}$$

where

$$\dot{y}_t = \left[\dot{y}_b + \dot{w}|_{L_b} + L_c\, \dot{w'}\big|_{L_b} \cos\left(w'|_{L_b}\right)\right].$$

The corresponding drag and lift force components can be expressed as [59]

$$F_D = \frac{1}{2}\rho_a C_{F_D}(\alpha) D_t L_t U_{rel}^2, \quad F_L = \frac{1}{2}\rho_a C_{F_L}(\alpha) D_t L_t U_{rel}^2, \tag{2.18}$$

where, ρ_a, is the air density, C_{F_D} and C_{F_L} are, respectively, the drag and lift coefficients obtained experimentally by static wind-tunnel tests for a given bluff body. These coefficients can be approximated by polynomial functions of α according to Parkinson and Brooks [59]. The normal force acting in the y-direction can be, therefore, written as

$$F_y = \frac{1}{2}\rho_a C_{F_y}(\alpha) D_t L_t U_\infty^2, \quad \text{where} \quad C_{F_y} = -\left[C_{F_D} \tan\Gamma + C_{F_L}\right] \sec\Gamma \tag{2.19}$$

in which, we assume that the resulting lateral force coefficient, C_{F_y}, can be expanded in powers of α as

$$C_{F_y} = a_1\alpha + a_3\alpha^3, \quad \alpha = w'|_{L_b} + (\dot{y}_b + \dot{w}|_{L_b})/U_\infty, \tag{2.20}$$

where a_1 and a_3 are empirical coefficients obtained by curve fitting. It should be mentioned that the fluid-structure interaction on the piezoelectric beam is assumed to have little influence on the dynamics when compared to that resulting from the bluff body, and is therefore neglected. To account for these effects, one can use the vortex lattice method as in [60, 61].

Substituting Equations (2.11), (2.14), and (2.16) back into Hamilton's equation, (2.10), then applying the δ operator and setting the coefficients of δw and δQ_R to zero, we obtain the following equations and boundary conditions governing the dynamics of the beam's transverse deflection, $w(s,t)$, and harvested voltage, $V(t)$, as:

$$\begin{aligned} &M(s)\ddot{w} + c_a\dot{w} + [YI(s)w'']'' + [w'(YI(s)w'w'')']' + \left[\theta(s)(1+\frac{1}{2}w'^2)\right]'' V(t) \\ &+ \left[w' \int_{L_b}^{s} M(s) \left[\frac{1}{2}\int_0^s (\ddot{w}')^2 ds\right] ds\right]' = -c_a\dot{y}_b - M(s)\ddot{y}_b \\ &-M_t\left[\delta(s-L_b) - L_c\delta'(s-L_b)\right]\ddot{y}_b + F_y\left[\delta(s-L_b) - L_c\delta'(s-L_b)\right], \end{aligned} \tag{2.21}$$

$$C_p\dot{V}(t) + \frac{1}{R}V(t) = \frac{\partial}{\partial t}\left[\int_0^{L_b} \theta(s)w''(1+\frac{1}{2}w'^2)ds\right], \tag{2.22}$$

where $\delta(s)$ is the Dirac-delta function. The associated boundary conditions, after

ignoring tip body inertia nonlinearity, are given by

$$\{w = 0,\ w' = 0\}|_{s=0}\,,$$
$$\left\{YI(s)w'' = -M_t L_c \ddot{w} - \left[I_t + M_t L_c^2\right]\ddot{w}',\ YI(s)w''' = M_t\left[\ddot{w} + L_c\ddot{w}'\right]\right\}\Big|_{s=L_b}.$$

2.2 Reduced-Order Model

In order to solve Equations (2.21) and (2.22), we utilize a Galerkin expansion to discretize the partial differential equations. To that end, we express the spatio-temporal function representing the transversal vibrations of the beam, $w(s,t)$, in the form of a convergent series of eigenfunctions multiplied by unknown temporal coordinates, i.e., we let

$$w(s,t) = \sum_{i=1}^{\infty} \phi_i(s) q_i(t), \tag{2.23}$$

where $q_i(t)$ are the generalized time-dependent coordinates and $\phi_i(s)$ are chosen as the set of mass-normalized orthonormal admissible functions representing the mode shapes of a clamped-free uniform beam with a tip mass rigidly attached at the free end. These are obtained by solving the differential eigenvalue problem and can be written as

$$\phi_i(s) = A_i\left[\cos\frac{\lambda_i}{L_b}s - \cosh\frac{\lambda_i}{L_b}s + \xi_i\left(\sin\frac{\lambda_i}{L_b}s - \sinh\frac{\lambda_i}{L_b}s\right)\right] \tag{2.24}$$

where

$$\xi_i = \frac{(\sin\lambda_i - \sinh\lambda_i) + R_1\lambda_i\left[\cos\lambda_i - \cosh\lambda_i - R_2\lambda_i\left(\sin\lambda_i + \sinh\lambda_i\right)\right]}{(\cos\lambda_i - \cosh\lambda_i) - R_1\lambda_i\left[\sin\lambda_i - \sinh\lambda_i + R_2\lambda_i\left(\cos\lambda_i - \cosh\lambda_i\right)\right]}$$

The eigenvalue of the i$^{\text{th}}$ mode denoted by λ_i represents the dimensionless free-undamped modal frequency expressed as

$$\omega_i = \lambda_i^2 \sqrt{\frac{Y^b I_b}{m_b L_b^4}} \tag{2.25}$$

The values of λ_i's can be obtained by solving the following characteristic equation associated of the differential eigenvalue problem:

$$\begin{aligned} &R_1 R_3 \left[1 - \cos\lambda_i \cosh\lambda_i\right] \lambda_i^4 - \left(R_1 R_2^2 + R_3\right) \left[\sin\lambda_i \cosh\lambda_i + \sinh\lambda_i \cos\lambda_i\right] \lambda_i^3 \\ &-2R_1 R_2 \left[\sin\lambda_i \sinh\lambda_i\right] \lambda_i^2 + R_1 \left[\cos\lambda_i \sinh\lambda_i - \cosh\lambda_i \sin\lambda_i\right] \lambda_i \\ &+ \left[1 + \cos\lambda_i \cosh\lambda_i\right] = 0, \end{aligned} \tag{2.26}$$

where R_1, R_2, and R_3 are, respectively, the mass, length, and rotary inertia ratios given by

$$R_1 = \frac{M_t}{m_b L_b}, \quad R_2 = \frac{L_c}{L_b}, \quad R_3 = \frac{I_t}{m_b L_b^3}. \tag{2.27}$$

The modal constant, A_i, is obtained by enforcing the following orthogonality condition:

$$\int_0^{L_b} \phi_i M(s) \phi_j ds + \left[\phi_i M_t \phi_j + \left(\phi_i M_t L_c \phi_j\right)' + \phi_i' \left(I_t + M_t L_{c.g}^2\right) \phi_j'\right]\Big|_{s=L_b} = \delta_{ij}, \tag{2.28}$$

where δ_{ij} is the Kronecker delta.

Substituting Equation (2.23) into Equation (2.21), multiplying by $\phi_n(s)$, integrating over the length of the beam, and using the orthonormality properties of the chosen mode shapes yields the following linearly-decoupled set of nonlinear ordinary differ-

ential equations ($n = 1, 2, 3, ...$):

$$\ddot{q}_n + 2\zeta_n\omega_n\dot{q}_n + \omega_n^2 q_n + \theta_n^* V(t) + \sum_{i,j}^{\infty} \mathcal{A}_{nij} q_i q_j V(t) + \sum_{i,j,k}^{\infty} \mathcal{B}_{nijk} q_i (\ddot{q}_j q_k + 2\dot{q}_j \dot{q}_k + q_j \ddot{q}_k)$$
$$+ \sum_{i,j,k}^{\infty} \mathcal{C}_{nijk} q_i q_j q_k = \mathcal{D}_n \ddot{y}_b + \mathcal{F}_n(q, \dot{q}, \dot{y}_b), \tag{2.29}$$

where ζ_n and ω_n are, respectively, the modal damping ratio and frequency; θ^* and $\mathcal{A}$ are the linear and nonlinear electromechanical coupling; $\mathcal{B}$ and $\mathcal{C}$ are the inertia and geometric nonlinearities; $\mathcal{D}_n$ and $\mathcal{F}_n$ are the external base excitation coefficient and the aerodynamic forcing term. Here, it is assumed that the modal damping ratio of a desired mode, ζ_n, can be identified directly through experimental modal analysis, the rest of the parameters are given by

$$\omega_n^2 = \int_0^{L_b} YI(s)\phi_n''^2 ds, \quad \theta_n^* = \int_0^{L_b} \phi_n \theta''(s) ds, \quad \mathcal{A}_{nij} = \frac{1}{2}\int_0^{L_b} \phi_n'' \theta(s) \phi_i' \phi_j' ds,$$
$$\mathcal{B}_{nijk} = \int_0^{L_b} \frac{\phi_n}{2} \left[\phi_i' \int_L^s M(s) \left(\int_0^s \phi_j' \phi_k' ds \right) ds \right]' ds,$$
$$\mathcal{C}_{nijk} = \int_0^{L_b} \phi_n \left[\phi_i' (YI(s)\phi_j' \phi_k'')' \right]' ds, \quad \mathcal{D}_n = -\int_0^{L_b} \phi_n M(s) ds - M_t \mathcal{E}_n,$$
$$\mathcal{E}_n = \left(\phi_n(L_b) + L_c \phi_n'(L_b) \right), \quad \mathcal{F}_n = \frac{1}{2}\mathcal{E}_n \rho_a D_t L_t U_\infty^2 \left(a_1 \alpha^* + a_3 {\alpha^*}^3 \right),$$
$$\alpha^* = \sum_i^{\infty} \phi_i'(L_b) q_i + \frac{1}{U_\infty} \left(\dot{y}_b + \sum_i^{\infty} \phi_i(L_b) \dot{q}_i \right).$$

Also, substituting Equation (2.23) into Equation (2.22), we obtain the following set

of modal equations governing the circuit dynamics:

$$C_p\dot{V}(t) + \frac{1}{R}V(t) = \sum_{n}^{\infty} \theta_n^* \dot{q}_n + \sum_{nij}^{\infty} \mathcal{A}_{nij}(\dot{q}_n q_i q_j + q_n \dot{q}_i q_j + q_n q_i \dot{q}_j). \tag{2.30}$$

Chapter 3

Experimental Validations

This Chapter describes the series of experiments conducted to assess the validity of the model derived in Chapter 2 and to enable parameter identification. Two cases are discussed; the first studies the performance of the harvester under combined loading when the wind speed is below the speed of galloping instability, while the second case studies the performance for wind speeds above the galloping speed.

3.1 Experimental Setup

Figure 5.17 shows the experimental setup used to investigate the harvester's response. The harvester consists of a Steel cantilever beam attached to a square-sectioned cylinder at the free end. A piezoelectric Macro Fiber Composite layer (MFC-M8514-P2, Smart Material Corporation) is laminated to the beam and connected to a resistive load to provide the electromechanical transduction. An electrodynamic shaker along with a signal generator is used to produce the harmonic base displacement. The acceleration level is measured by an accelerometer and used as a feedback to the

signal generator to maintain the base acceleration at a fixed level while varying the frequency. The velocity response of the cantilever is recorded by a laser vibrometer. The experimental setup is placed in a controlled air flow environment to produce the aerodynamic excitation such that the bluff body is facing the airflow. The average wind speed in the vicinity of the harvester is measured using an anemometer. The generated voltage and other captured data are acquired through a dSpace data acquisition system.

The geometric and material properties of the harvester are listed in Table 5.2. Before delving into the experimental validations, a convergence analysis is conducted to determine the minimum number of modes to be kept in the Galerkin expansion such that the addition of any more modes does not affect the predictions of the response. Towards that end, the equations of motion are integrated numerically using a single- and three-mode expansions. The resulting RMS tip deflection as function of wind

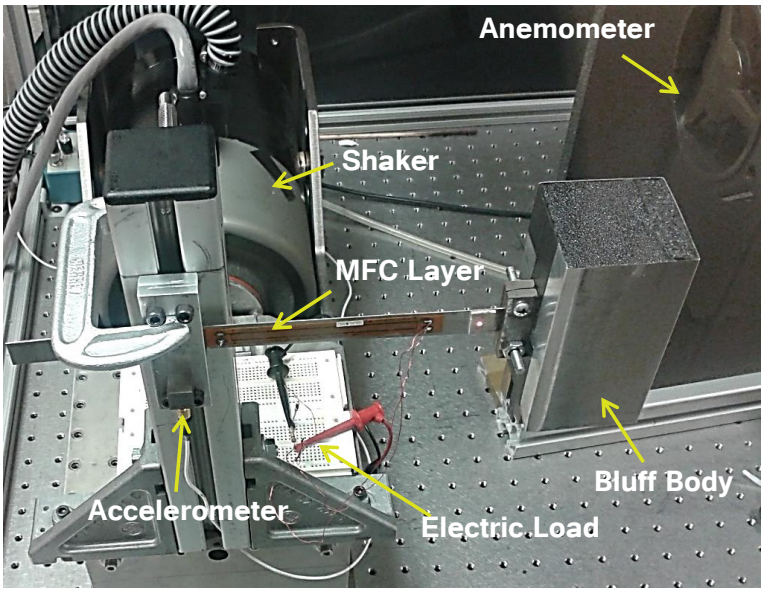

Figure 3.1: A view of the experimental setup.

speed is shown in Fig. 3.2 (a). The figure clearly demonstrates negligible differences between the single- and three-mode response with a maximum error of less than 0.35%. This indicates that a single-mode is sufficient to capture the dynamics of the response. As such, further analysis presented in this manuscript will be based on a reduced-order model consisting of a single mode. Initially, the mechanical damping

Table 3.1: Geometric and material properties of the piezoelectric galloping energy harvester.

Physical properties	
Structural member	
Young's modulus, (E_b)	190 GPa
Mass density, (ρ_b)	9873 kg/m^3
Length, (L_b)	14.5 cm
Width, (W_b)	1.4 cm
Thickness, (t_b)	0.51 mm
Piezoelectric member	
Young's modulus, (E_p)	15.86 GPa
Mass density, (ρ_p)	5440 kg/m^3
Length, (L_p)	8.5 cm
Width, (W_p)	7 mm
Thickness, (t_p)	0.3 mm
Permittivity, (e_{33})	19.36 nF/m
Piezoelectric constant, (d_{31})	-170 pm/V
Bluff body	
Mass, (M_t)	102.3 g
Moment of inertia, (I_t)	2614.3 g.cm^2
Width, (D_t)	5.08 cm
Length, (L_t)	10.16 cm
Other	
Air density, (ρ_a)	1.24 kg/m^3
Electric load, (R)	100 kΩ

ratio is identified experimentally by matching the peaks of the deflection frequency response curves for low base excitation level and short circuit conditions as shown

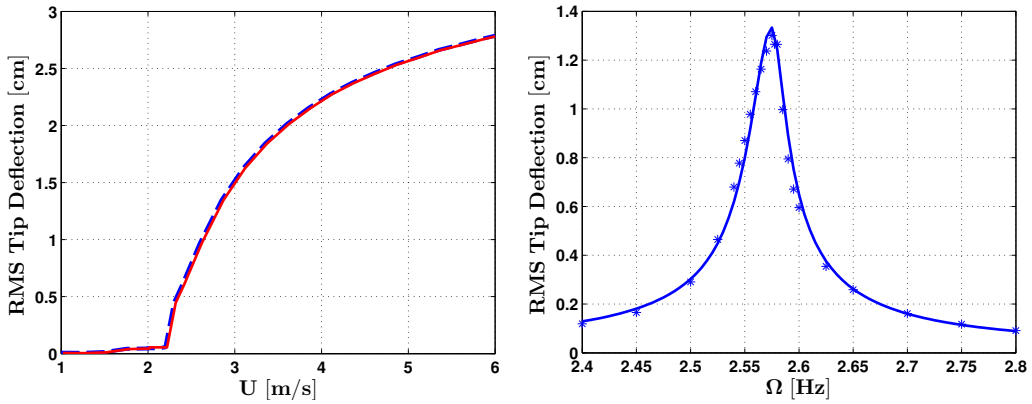

(a) (b)

Figure 3.2: Variation of the RMS tip deflection with (a) wind speed: Single-mode approximation (solid) and a three-mode reduced order model (dashed) and (b) excitation frequency for a base excitation of 0.08 m/s^2: Theoretical (solid-line), and experimental (asterisks).

in Fig. 3.2 (b). The estimated value is found to be $\zeta = 0.0063$. Furthermore, the parameters associated with the aerodynamic normal force are identified by conducting wind velocity sweeps in the absence of the base excitation. The linear coefficient, a_1, is then predicted by Den Hartog's criterion at the galloping speed, at which the negative damping from airflow balances the positive damping of the harvester. The cubic term, a_3, on the other hand, is estimated by matching the experimental response with theoretical simulations in the range above the galloping speed. The estimated values are found to be, $a_1 = 3.75$, and $a_3 = -14.8$.

3.2 Galloping Speed

To determine the galloping speed, variation of the harvester's response with the wind speed is first investigated in the absence of base excitation. The experimental and

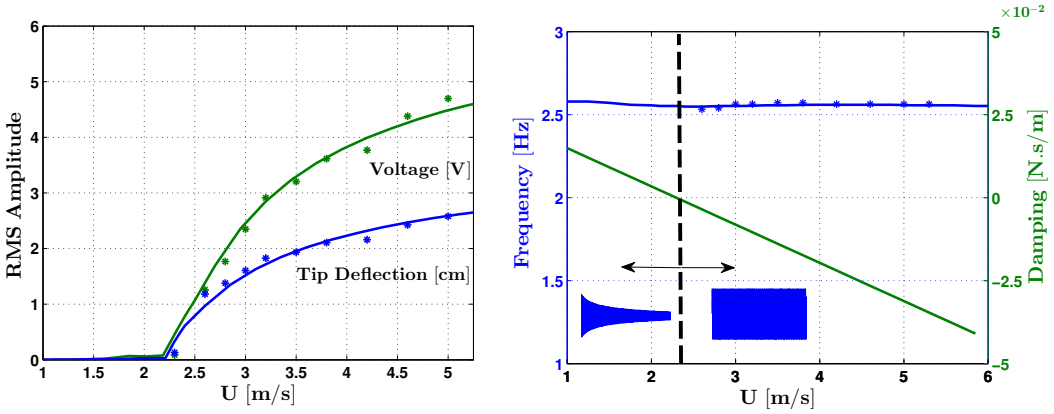

Figure 3.3: Variation with wind speed (a) the steady-state RMS amplitude of the beam tip deflection and output voltage and (b) the response frequency and the effective damping. Asterisks represent experimental data.

predicted values of the steady-state root mean square (RMS) beam tip deflection and the generated voltage are plotted and compared as shown in Fig. 3.3 (a). Results demonstrate that the harvester is capable of maintaining fixed amplitude steady-state motions as long as the wind speed is slightly above 2.3 m/s which corresponds to the onset speed of galloping. This can be further seen in Fig. 3.3 (b) which shows variation of the effective damping of the harvester with the wind speed. As the wind speed is increased beyond 2.3 m/s, the effective damping becomes negative giving rise to galloping oscillations. The figure also shows that the frequency of galloping oscillations is always consistent with the first modal frequency of the harvester further justifying the use of a single-mode reduced-order model.

3.3 Response Behavior Below the Galloping Speed

Next, the performance of the harvester under combined loading is assessed by integrating Equations (2.29) and (2.30) numerically and generating the response when the harvester is subjected to harmonic base excitation and wind speeds below the galloping speed. Figure 3.4 depicts variation of the frequency response curves of the RMS tip deflection and the harvested voltage when a constant base acceleration of 0.11 m/s^2 is applied at the base while the wind speed is kept below the galloping speed. In this case, self-sustained oscillations resulting from the aerodynamic forces cannot be excited and the response is always periodic containing only the frequency of excitation, Ω. For a wind speed of 2 m/s, a substantial amplification in the harvester's response is observed when compared to the frequency response curve in the absence of any aerodynamic loads, $U = 0$ m/s. The amplification, which emanates from a reduction in the effective damping of the system due to the aerodynamic loads, increases the output voltage by as much as 55%, which clearly demonstrates the enhanced performance of the harvester under dual loading at low wind speeds. In fact, if not for the hardening nonlinearities present in the beam's restoring force and aerodynamic loading which limit the growth of the steady-state response, a much more significant amplification of the response can be achieved since the linear damping approaches zero when the wind speed approaches the galloping speed. These results are validated through experimental measurements of the harvester's response under the same loading conditions as depicted in Fig. 3.5.

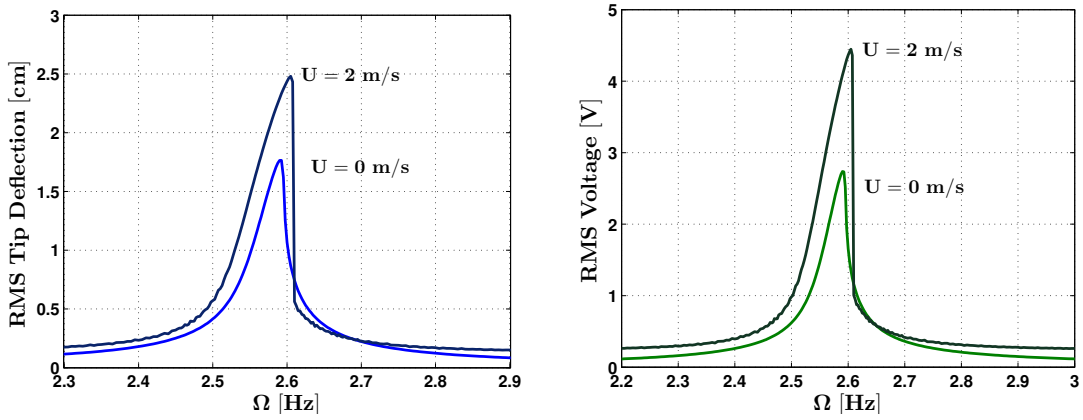

(a) (b)

Figure 3.4: Variation of the theoretical response with the excitation frequency for different wind speeds above the onset speed of galloping: (a) RMS tip deflection and (b) RMS output voltage.

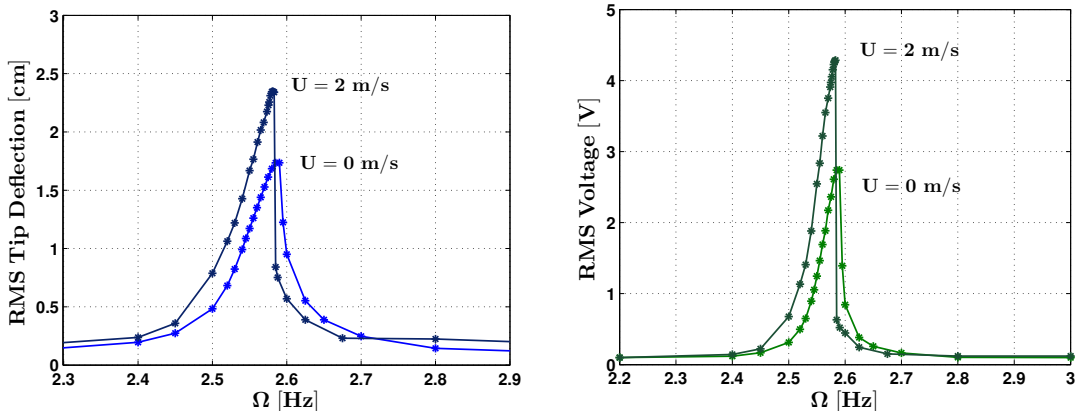

(a) (b)

Figure 3.5: Variation of the experimental response with the excitation frequency for different wind speeds above the onset speed of galloping: (a) RMS tip deflection and (b) RMS output voltage.

3.4 Response Behavior Above the Galloping Speed

When the wind speed is increased beyond 2.3 m/s, the harvester's response can be periodic or quasi-periodic due to the presence of two frequencies in the response;

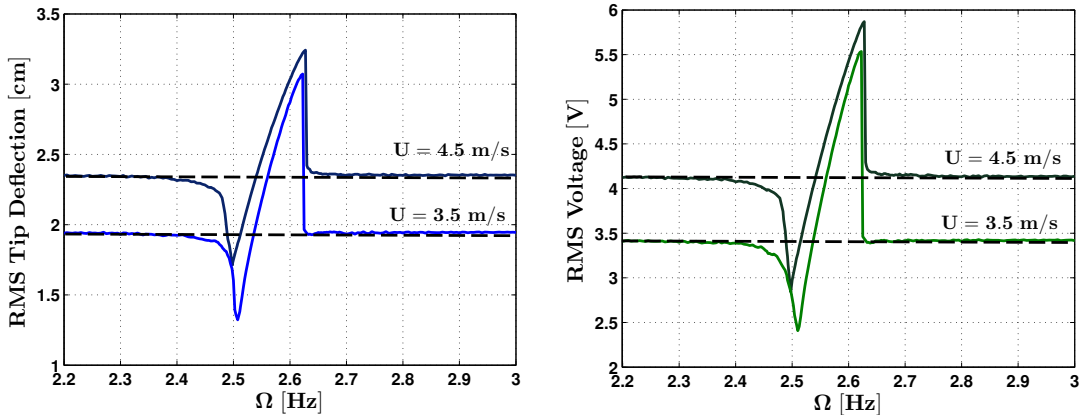

(a) (b)

Figure 3.6: Variation of the theoretical response with the excitation frequency for different wind speeds below the onset speed of galloping: (a) RMS tip deflection and (b) RMS output voltage.

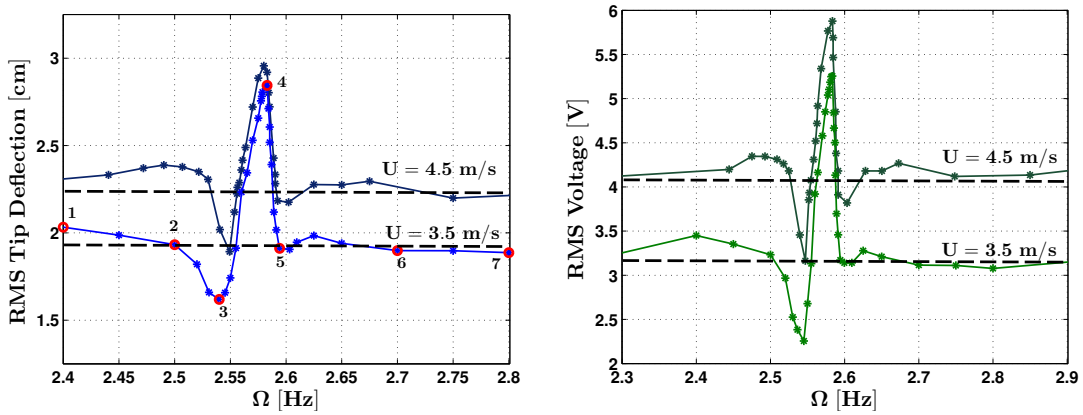

(a) (b)

Figure 3.7: Variation of the experimental response with the excitation frequency for different wind speeds below the onset speed of galloping: (a) RMS tip deflection and (b) RMS output voltage.

namely those resulting from the base excitation and self-sustained galloping oscillations. Hence, for a given wind speed and base acceleration, the overall performance of the harvester can be analyzed based on the nearness of the two frequencies. Towards investigating the influence of these parameters, Equations (2.29) and (2.30) are inte-

grated numerically to generate the RMS frequency-response curves of the harvester's response at a constant base acceleration of 0.15 m/s^2 and different wind speed above 2.3 m/s as depicted in Fig. 3.6. For performance comparison purposes, the RMS value of the harvester's response corresponding to galloping excitations only is also shown in the figure by dashed lines.

When the excitation frequency is away from resonance, the resulting response is quasi-periodic. In this range of frequency, the effect of the base excitation diminishes and the steady-state RMS response resulting from the combined loading approaches that resulting from the aerodynamic loads alone. For excitation frequencies that are closer to the resonance frequency but still outside the resonance bandwidth, the RMS response drops below that obtained using the aerodynamic loading alone. Due to the hardening nonlinearity, the dip in the response amplitude is slightly lower for frequencies above resonance. Finally, when the response is periodic and the excitation frequency is very close to the natural frequency, the two frequencies lock into each other resulting in a periodic response. In this region, a significant improvement in the harvester's output voltage is observed. The percentage improvement relative to the galloping response decreases as the wind speed is increased for the same base acceleration level.

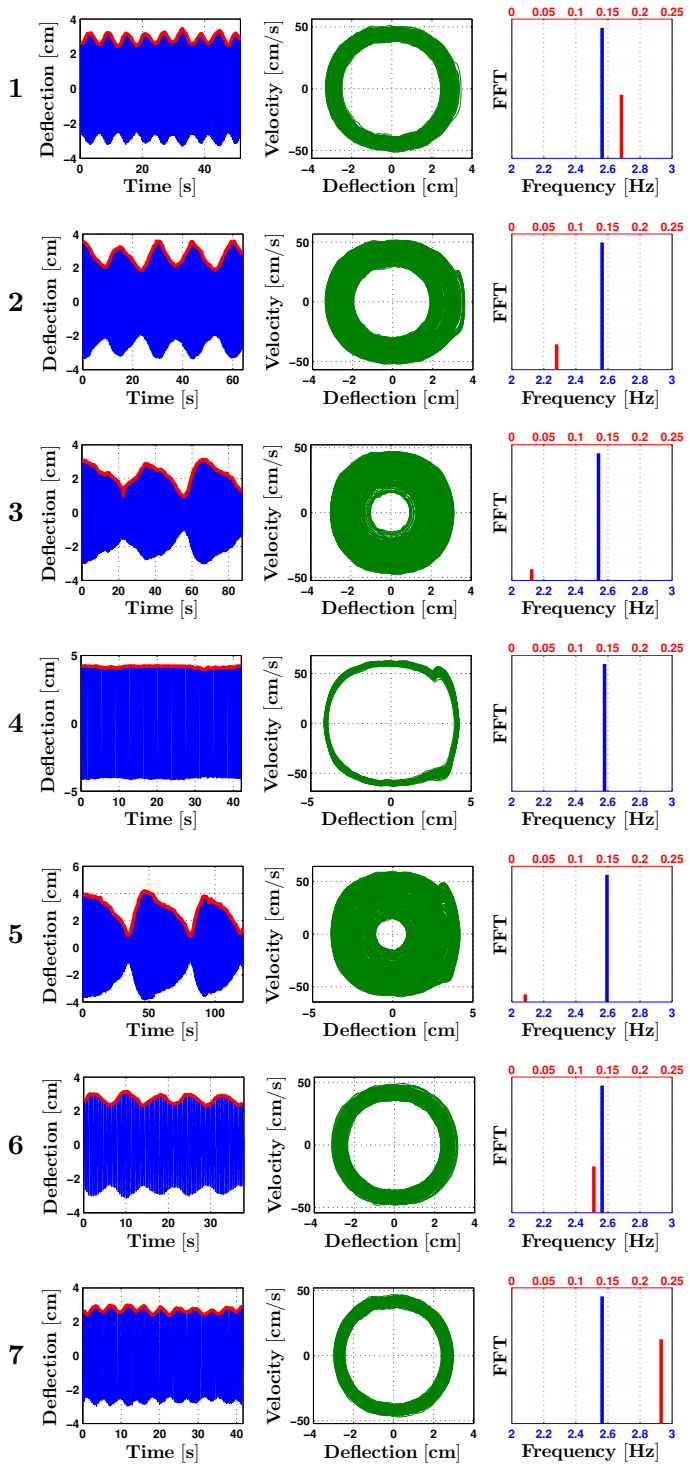

Figure 3.8: (Color online) Experimental time histories, phase portraits, and power spectra of the harvester at points (1)-(7) shown in Fig. 3.7(a).

These results are confirmed experimentally as depicted in Fig. 3.7. The overall agreement between the numerical and experimental results over the frequency range of interest is reasonable. This again demonstrates that a single-mode reduced-order model of the system is sufficient to predict the response behavior. The transition from periodic to quasiperiodic responses or vice versa is further demonstrated in Fig. 3.8 by plotting the time history, phase portrait, and the fast Fourier transform (FFT) of the deflection at different excitation frequencies corresponding to the points numbered from 1 to 7 in Fig. 3.7 (a). The figure clearly shows that the maximum improvement in the harvester's response under combined loading occurs at point 4 which represents the resonant peak in the periodic response region.

Variation of the RMS frequency-response curves for the tip deflection and the output voltage at a constant wind speed of 3.8 m/s and different base accelerations is shown in Fig. 3.9. As mentioned previously, when the excitation frequency is away from resonance, the base excitation has a negligible influence on the harvester's response and the total RMS responses under combined loading approach that resulting from the galloping excitation alone regardless of the base acceleration level.

When the excitation frequency is closer to the resonance bandwidth, four different scenarios can occur as the base acceleration is increased. The first scenario involves a transition between two different quasi-periodic responses, for instance, at $\Omega = 2.45$ Hz. In this case, increasing the base acceleration has a negative influence on the performance of the harvester and reduces the output power. In the second scenario, a transition between two different periodic responses occurs as the base acceleration is increased. This improves the performance of the harvester as can be seen at $\Omega = 2.55$ Hz. The third scenario occurs at frequencies slightly above the peak frequency. In this case, increasing the base acceleration quenches the quasi-periodic

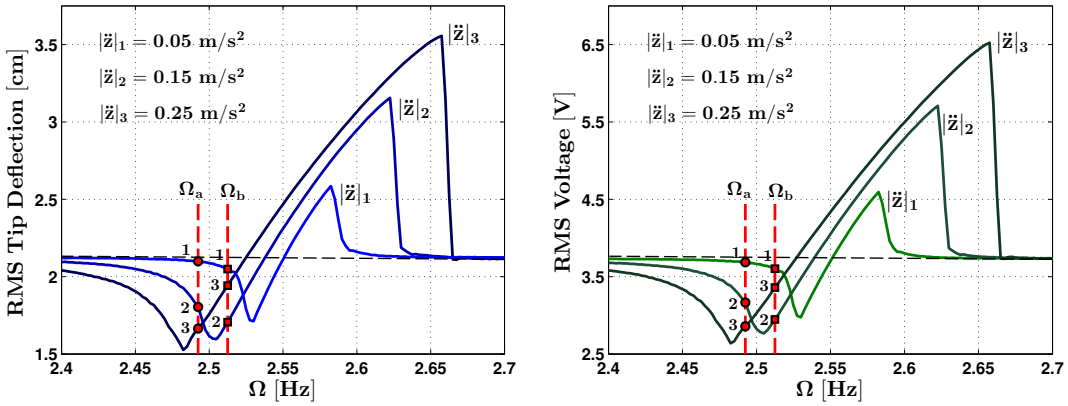

(a) (b)

Figure 3.9: (Color online) Variation of the harvester's response with the excitation frequency at constant wind speed of 3.8 m/s and different base acceleration amplitudes: (a) RMS tip deflection and (b) RMS output voltage.

response leading to a periodic response. This process improves the harvester's output power tremendously as can be seen when increasing the base acceleration from $|\ddot{z}|_1$ to $|\ddot{z}|_2$ at $\Omega = 2.6$ Hz. The last scenario occurs when increasing the base acceleration leads to a transition from periodic to a quasi-periodic response or vice versa. This takes place at frequencies below the peak frequency where the two responses coexist depending on the excitation level, for instance at Ω_a and Ω_b. In this case, the RMS value of the response can either increase or decrease as the base acceleration level is increased. This is further demonstrated by studying variation of the RMS tip deflection and the output voltage at Ω_a and Ω_b with the base acceleration level as depicted numerically and experimentally in Fig. 3.10. It should be noted that, as the acceleration level is increased, the maximum performance enhancement of a harvester under combined excitations as compared to galloping alone, only occurs in the second and third scenarios for frequencies slightly above and below the peak frequencies.

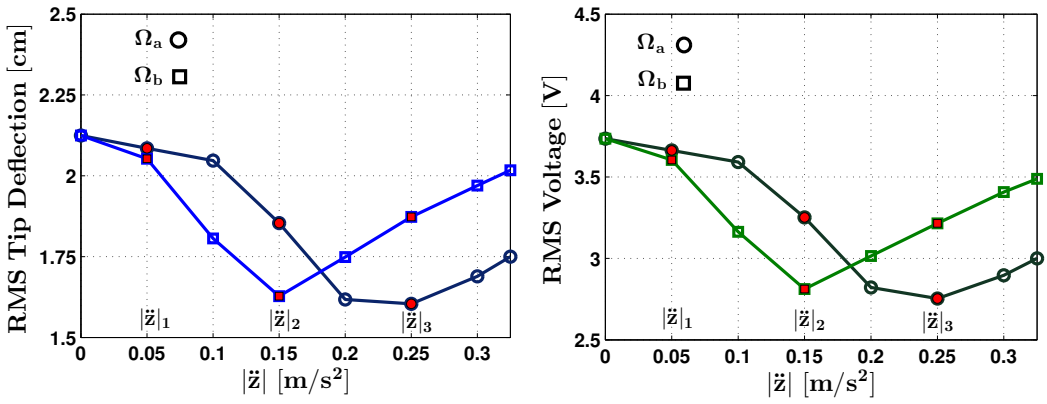

(a)

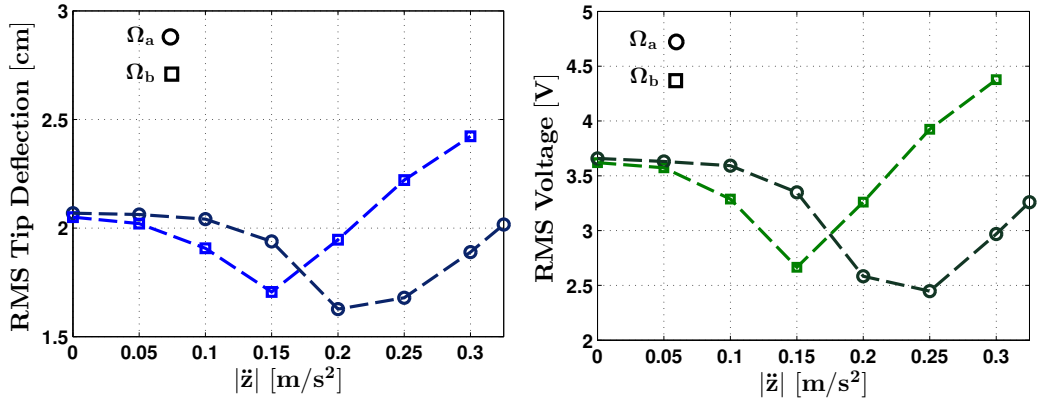

(b)

Figure 3.10: (Color online) Variation of the RMS tip deflection and output voltage with the base excitation at a constant wind speed of 3.8 m/s and different excitation frequencies: (a) numerical and (b) experimental.

Chapter 4

Nonlinear Analysis of Galloping-based Energy Harvesters

The open literature contains a large number of examples describing the design and characterization of FEHs incorporating the galloping mechanism [44, 45, 46, 47, 62]. Results have been presented for different prismatic bodies, geometric, and material properties of the oscillator, as well as different transduction mechanisms and circuit designs. However, as of today, there is no clear understanding of the relative performance of these devices, or which combination of design parameters yield the optimal performance of the harvester for a given flow conditions. This Chapter aims to fill this void by presenting a generalized analytical formulation which can simplify the analysis and performance optimization of galloping energy harvesters. We hope that the analytical analysis presented here will provide additional insights towards designing more efficient galloping FEHs.

4.1 General Formulation

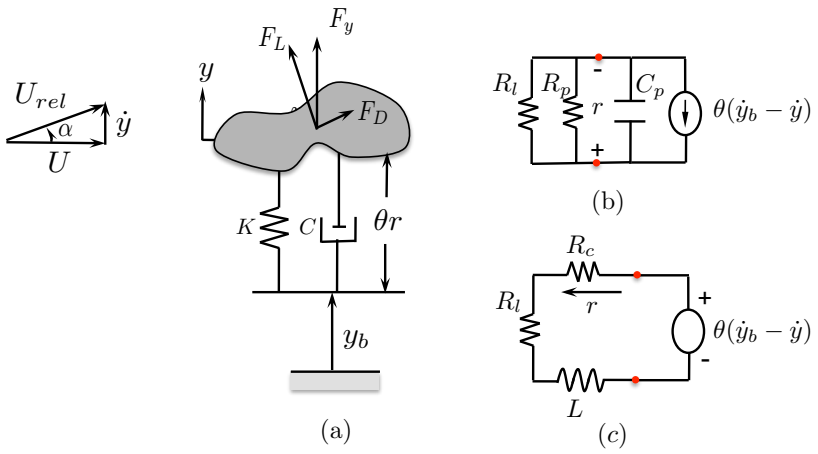

Figure 4.1: A schematic diagram of the single-mode flow energy harvester.

Based on the experimental validation results, its shown that a single-mode reduced-order model is sufficient to predict the response behavior of the system and, hence, is utilized in conducting a nonlinear analysis to obtain an approximate analytical solution which can be used to gain a better qualitative understanding of the effect of design parameters. After ignoring the geometric, inertia, and electromechanical coupling nonlinearities, which are generally very small as compared to the other terms, the model can be written as

$$M\ddot{y} + C\dot{y} + Ky - \theta V = F_y + Ky_b + C\dot{y}_b, \tag{4.1}$$

$$\begin{aligned} C_p\dot{r} + \frac{r}{R} + \theta\left(\dot{y} - \dot{y}_b\right) = 0, \ \text{(piezoelectric)}, \\ L\dot{r} + Rr + \theta\left(\dot{y} - \dot{y}_b\right) = 0, \ \text{(electromagnetic)}, \end{aligned} \tag{4.2}$$

Here, the dot represents a derivative with respect to time, t. The effective mass of the

bluff body and the supporting structure is represented by M; while K, C, and θ are, respectively, the linear stiffness, damping, and electromechanical coupling coefficients as shown in Fig. 4.1 (a). These values can be obtained by relating the terms to their corresponding modal parameters in Equation 2.29.

Equations (5.1a) and (5.1c) represent a linear mechanical oscillator coupled to an electric circuit through either a first-order RC circuit representing a piezoelectric transduction mechanism or a first-order RL circuit representing an electromagnetic transduction as shown in Fig. 4.1 (b) and (c), respectively. Here, C_p is the capacitance of the piezoelectric element, and L is the inductance of the harvesting coil.

In addition to dynamic flow forces, F_y, corresponding to wind speed U, the harvester is subjected to a base excitation, y_b. Due to the combined loading, the mass oscillates in the cross flow direction with an absolute displacement, y. These oscillations produce an electric output, r, across an electric load, R. The electric output, r, represents the voltage in piezoelectric energy harvesters and the current in electromagnetic ones. The load, R, is the parallel equivalent of the piezoelectric resistance, R_p, and the load resistance, R_l, for piezoelectric transduction, and the series equivalent of the load and coil resistance, R_c, for electromagnetic transduction.

For generality, the vertical component of the aerodynamic force, F_y, acting on the bluff body is modeled using a quasi-steady assumption with a m^{th}-order polynomial approximation in $\frac{\dot{y}}{U}$ such that [59]

$$F_y = \frac{1}{2}\rho_a U^2 L_t D_t C_{\dot{y}}, \tag{4.3}$$

where

$$C_{\dot{y}} = \sum_{n:\text{odd}}^{m} A_n \left(\frac{\dot{y}}{U}\right)^n + \sum_{n:\text{even}}^{m} A_n \left(\frac{\dot{y}}{U}\right)^n \frac{\dot{y}}{|\dot{y}|}, \qquad n \geq 1. \tag{4.4}$$

The coefficients, A_n, are dependent on the general geometry and aspect ratio of the bluff body. These are usually obtained empirically from normal aerodynamic force measurements on a static bluff body at different angles of attack [59].

4.1.1 Non-dimensional Model

To obtain a dimensionless form of Equations (5.1a) and (5.1c), we introduce the following non-dimensional parameters

$$\begin{aligned}
&\bar{y} = \frac{y}{D_t}, \qquad \bar{y}_b = \frac{y_b}{D_t}, \qquad \mu = \frac{\rho_a L_t D_t^2}{4M}, \qquad \bar{U} = \frac{U}{\omega_n D_t}, \\
&\bar{r} = \frac{C_p}{\theta D_t} r, \qquad \kappa = \frac{\theta^2}{K C_p}, \quad \alpha = \frac{1}{R C_p \omega_n}, \quad \text{(piezoelectric)} \\
&\bar{r} = \frac{L}{\theta D_t} r, \qquad \kappa = \frac{\theta^2}{K L}, \quad \alpha = \frac{R}{L \omega_n}, \quad \text{(electromagnetic)}
\end{aligned}$$

where $\bar{y}$, $\bar{y}_b$, and $\bar{r}$ represent the dimensionless transverse displacement, base displacement, and electric quantity, respectively, μ is the flow to harvester mass ratio, $\bar{U}$ is the reduced wind speed, κ is the dimensionless electromechanical coupling, α is the mechanical to electrical time-constant ratio. The natural frequency of the harvester at short-circuit conditions is given by $\omega_n = \sqrt{K/M}$ and used to introduce the non-dimensional time as $\bar{t} = \omega_n t$; whereas the mechanical damping ratio, ζ_m, is defined by $C = 2\zeta_m M \omega_n$. Equations (5.1a) and (5.1c) can be rewritten in terms of the non-dimensional parameters as

$$\bar{y}'' + 2\zeta_m \bar{y}' + \bar{y} - \kappa \bar{r} = 2\mu \bar{U}^2 C_{\bar{y}} + \bar{y}_b + 2\zeta_m \bar{y}_b', \tag{4.5}$$

$$\bar{r}' + \alpha\bar{r} + (\bar{y}' - \bar{y}_b') = 0. \tag{4.6}$$

Here, the prime denotes a derivative with respect to non-dimensional time, $\bar{t}$ and the non-dimensional lateral force coefficient is given by

$$C_{\bar{y}} = \sum_{n:\text{odd}} A_n \left(\frac{\bar{y}'}{\bar{U}}\right)^n + \sum_{n:\text{even}} A_n \left(\frac{\bar{y}'}{\bar{U}}\right)^n \frac{\bar{y}'}{|\bar{y}'|}, \qquad n \geq 1. \tag{4.7}$$

4.1.2 Model Assumptions

The general model presented here invokes several assumptions on the fluid-structural interaction problem that are worth mentioning:

1. The quasi-steady assumption: This is a very common assumption that simplifies the modeling of the fluid interactions with the bluff body [63]. Quasi-steadiness essentially implies that the motion of the bluff body is too slow compared to the motion of the fluid such that vertical force stays constant for a given angle of attack. This assumption requires that $U/(\omega_n D_t) \geq 10$

2. The effect of added mass and fluid damping is neglected. This is a valid assumption for low density and low viscosity fluids such as air.

Additionally, the restoring force is assumed to be a linear function of the displacement. This implies that the geometric nonlinearities in the structure can be neglected which is an accurate assumption for sufficiently small deflections.

4.2 Approximate Analytical Solution

In an attempt to understand the dynamics described by Equations (4.5) and (4.6), we present an approximate analytical solution of these equations utilizing the method of multiple scales. Towards that end, the time dependence is expanded into fast and slow time scales in the form $T_0 = \bar{t}$ and $T_1 = \epsilon\bar{t}$, respectively, where ϵ is a scaling parameter. Using the new time scales the time derivatives can be expressed as

$$\frac{d}{d\bar{t}} = D_0 + \epsilon D_1 + O(\epsilon^2), \qquad \frac{d^2}{d\bar{t}^2} = D_0^2 + 2\epsilon D_0 D_1 + O(\epsilon^2), \tag{4.8}$$

where $D_n = \frac{\partial}{\partial T_n}$. Furthermore, we expand $\bar{y}$ and $\bar{V}$ in the following forms:

$$\begin{aligned} \bar{y}(\bar{t}) &= \bar{y}_0(T_0, T_1) + \epsilon\bar{y}_1(T_0, T_1) + O(\epsilon^2), \\ \bar{r}(\bar{t}) &= \bar{r}_0(T_0, T_1) + \epsilon\bar{r}_1(T_0, T_1) + O(\epsilon^2), \end{aligned} \tag{4.9}$$

The constant coefficients in Equation (4.5) are scaled such that the effect of viscous damping, electromechanical coupling, and aerodynamic forcing appear at the same order of the perturbation problem. In other words, we let

$$\zeta_m = \epsilon\zeta_m, \qquad \kappa = \epsilon\kappa, \qquad \text{and} \qquad \mu = \epsilon\mu. \tag{4.10}$$

Since the influence of the base excitations is dominant near the natural frequency of the harvester, only its primary-resonant influence is analyzed; that is, the excitation frequency is assumed to be close to the natural frequency of the harvester. Therefore, a detuning parameter, σ, is introduced to describe the nearness of theses two frequencies by letting $\omega = (1 + \epsilon\sigma)\omega_n$, or $\Omega = \frac{\omega}{\omega_n} = (1 + \epsilon\sigma)$. Moreover, we order the amplitude of base excitation so that it appears in the same perturbation equation as

the previously scaled parameters. Thus, we assume the excitation to have the form

$$\bar{y}_b = \epsilon|\bar{y}_b|\cos(\Omega\bar{t}) = \epsilon|\bar{y}_b|\cos(T_0 + \sigma T_1). \tag{4.11}$$

Substituting the time scaling, its derivatives, and the scaled parameters back into Equations (4.5) and (4.6) then collecting terms of equal powers of ϵ yields
$O(\epsilon^0)$:

$$D_0^2\bar{y}_0 + \bar{y}_0 = 0, \tag{4.12}$$

$$D_0\bar{r}_0 + \alpha\bar{r}_0 = -D_0\bar{y}_0, \tag{4.13}$$

$O(\epsilon^1)$:

$$D_0^2\bar{y}_1 + \bar{y}_1 = -2D_0D_1\bar{y}_0 - 2\zeta_m D_0\bar{y}_0 + \kappa\bar{r}_0 + 2\mu\bar{U}^2C_{\bar{y}_0} + |\bar{y}_b|\cos(T_0 + \sigma T_1), \tag{4.14}$$

$$D_0\bar{r}_1 + \alpha\bar{r}_1 = -D_1\bar{r}_0 - D_1\bar{y}_0 - D_0\bar{y}_1 - |\bar{y}_b|\sin(T_0 + \sigma T_1), \tag{4.15}$$

where

$$C_{\bar{y}_0} = \sum_{n:\text{odd}} A_n\left(\frac{D_0\bar{y}_0}{\bar{U}}\right)^n + \sum_{n:\text{even}} A_n\left(\frac{D_0\bar{y}_0}{\bar{U}}\right)^n \frac{D_0\bar{y}_0}{|D_0\bar{y}_0|}, \qquad n \geq 1. \tag{4.16}$$

The solution of the zeroth-order perturbation problem can be written as

$$\bar{y}_0 = a\left(T_1\right)\cos\phi, \tag{4.17}$$

$$\bar{r}_0 = \gamma a\left(T_1\right)\sin\left[\phi - \psi\right], \quad \gamma = \frac{1}{\sqrt{1+\alpha^2}}, \quad \psi = \sin^{-1}\gamma, \tag{4.18}$$

where $\phi = [T_0 + \beta(T_1)]$; while $a\left(T_1\right)$ and $\beta\left(T_1\right)$ are, respectively, slowly varying amplitude and phase functions to be determined at the next step. Substituting Equations

(4.17) and (4.18) into Equation (4.14) and eliminating the secular terms (terms that have the factor $\cos[\phi]$ or $\sin[\phi]$), yields

$$
\begin{aligned}
a' = &-\frac{1}{\pi}\int_0^{2\pi}\left\{\zeta_m a\sin\phi + \frac{\kappa}{2}\gamma a\sin[\phi-\psi] + \frac{|\bar{y}_b|}{2}\cos[\phi-\beta+\sigma T_1]\right\}\sin\phi d\phi \\
&-\frac{\mu\bar{U}^2}{\pi}\sum_{n:\text{even}} A_n\left(\frac{a}{\bar{U}}\right)^n\int_0^{2\pi}\sin^n\phi\frac{-\sin\phi}{|-\sin\phi|}\sin\phi d\phi \\
&-\frac{\mu\bar{U}^2}{\pi}\sum_{n:\text{odd}} A_n\left(\frac{a}{\bar{U}}\right)^n\int_0^{2\pi}\sin^n\phi\sin\phi d\phi, \qquad (4.19)\\
a\beta' = &-\frac{1}{\pi}\int_0^{2\pi}\left\{\zeta_m a\sin\phi + \frac{\kappa}{2}\gamma a\sin[\phi-\psi] + \frac{|\bar{y}_b|}{2}\cos[\phi-\beta+\sigma T_1]\right\}\cos\phi d\phi \\
&-\frac{\mu\bar{U}^2}{\pi}\sum_{n:\text{even}} A_n\left(\frac{a}{\bar{U}}\right)^n\int_0^{2\pi}\sin^n\phi\frac{-\sin\phi}{|-\sin\phi|}\cos\phi d\phi \\
&-\frac{\mu\bar{U}^2}{\pi}\sum_{n:\text{odd}} A_n\left(\frac{a}{\bar{U}}\right)^n\int_0^{2\pi}\sin^n\phi\cos\phi d\phi. \qquad (4.20)
\end{aligned}
$$

Using De Moivre's formula, Euler's formula and binomial theorem [64], one can write

$$
\sin^n\phi = \frac{1}{2^n}\binom{n}{\frac{n}{2}} + \frac{2}{2^n}\sum_{k=0}^{\frac{n}{2}-1}(-1)^{\left(\frac{n}{2}-k\right)}\binom{n}{k}\cos[(n-2k)\phi], \quad \text{if n is even} \qquad (4.21)
$$

$$
\sin^n\phi = \frac{2}{2^n}\sum_{k=0}^{\frac{n-1}{2}}(-1)^{\left(\frac{n-1}{2}-k\right)}\binom{n}{k}\sin[(n-2k)\phi], \quad \text{if n is odd.} \qquad (4.22)
$$

Carrying out the integration in Equations (4.19) and (4.20), we obtain

$$a' = -\zeta_T a + \mu \bar{U}^2 C_a + \frac{|\bar{y}_b|}{2} \sin\delta, \tag{4.23}$$

$$a\delta' = \left(\sigma - \frac{\zeta_e}{\alpha}\right) a + \frac{|\bar{y}_b|}{2} \cos\delta, \tag{4.24}$$

where $\delta = \sigma T_1 - \beta$. The parameter $\zeta_T = \zeta_m + \zeta_e$ represents the total damping in the system, in which the electrical damping component is given by $\zeta_e = \alpha\kappa/\left[2(1+\alpha^2)\right]$. The lateral force coefficient, for $n \geq 1$, is expressed as a polynomial function of a as

$$C_a = \left[\sum_{n:\text{even}} \frac{4A_n}{\pi} \left(\frac{a}{2\bar{U}}\right)^n \sum_{k=0}^{n/2} \frac{(-1)^{\frac{n}{2}-k}}{(n+1-2k)} \binom{n+1}{k} + \sum_{n:\text{odd}} A_n \left(\frac{a}{2\bar{U}}\right)^n \binom{n+1}{\frac{n+1}{2}} \right], \tag{4.25}$$

4.3 Asymptotic Response

At steady-state, the fixed points of Equations (4.23) and (4.24), a_0 and δ_0, respectively, correspond to the steady-state amplitude and phase of the periodic solutions of the original Equations, i.e. Equations (4.5) and (4.6). Therefore, the non-dimensional displacement and voltage can be written, to the first approximation, as

$$\bar{y} = a_0 \cos\left(\Omega\bar{t} - \delta_0\right) + O(\epsilon), \qquad \bar{r} = \gamma a_0 \sin\left[\Omega\bar{t} - (\delta_0 + \psi)\right] + O(\epsilon). \tag{4.26}$$

The fixed points, a_0 and δ_0 are obtained by setting the time derivatives in Equations (4.23) and (4.24) to zero, i.e. $a' = \delta' = 0$. Squaring and adding the resulting

expressions yields the flow-frequency-response equation:

$$(\Omega^* a^*)^2 + \left[U^{*2} C_{a^*} - a^*\right]^2 = |\bar{y}_b|^{*2}, \tag{4.27}$$

where

$$\Omega^* = \frac{\sigma - \zeta_e/\alpha}{\zeta_T}, \qquad a^* = \frac{a\mu}{\zeta_T}, \qquad U^* = \frac{\bar{U}\mu}{\zeta_T}, \qquad |\bar{y}_b|^* = \frac{|\bar{y}_b|\mu}{2\zeta_T^2},$$

$$C_{a^*} = \left[\sum_{n:\text{even}} \frac{4A_n}{\pi} \left(\frac{a^*}{2U^*}\right)^n \sum_{k=0}^{n/2} \frac{(-1)^{\frac{n}{2}-k}}{(n+1-2k)} \binom{n+1}{k} + \sum_{n:\text{odd}} A_n \left(\frac{a^*}{2U^*}\right)^n \binom{n+1}{\frac{n+1}{2}}\right],$$

4.4 Stability Analysis

The stability of the resulting asymptotic solutions can be assessed by evaluating the eigenvalues of the Jacobain matrix associated with Equations (4.23) and (4.24), which is given by

$$J = \begin{bmatrix} \zeta_T \left(U^{*2} \frac{dC_{a^*}}{da^*} - 1\right) & \zeta_T^2 |\bar{y}_b^*| \cos\left(\zeta_T \delta^*\right) \\ -\frac{|\bar{y}_b^*|}{a^{*2}} \cos\left(\zeta_T \delta^*\right) & -\zeta_T \frac{|\bar{y}_b^*|}{a^*} \sin\left(\zeta_T \delta^*\right) \end{bmatrix}.$$

The eigenvalues of the Jacobian matrix, λ_i, are then obtained by taking the determinant of the Jacobian matrix which yields the following characteristic equation:

$$\lambda_i^2 - \zeta_T \left[U^{*2} \left(\frac{C_{a^*}}{a^*} + \frac{dC_{a^*}}{da^*}\right) - 2\right] \lambda_i + \zeta_T^2 \left[\Omega^{*2} + \left(U^{*2} \frac{C_{a^*}}{a^*} - 1\right) \left(U^{*2} \frac{dC_{a^*}}{da^*} - 1\right)\right] = 0. \tag{4.28}$$

By inspecting Equation (4.28), it can be noted that stable fixed points, and thereby, stable periodic solutions exist when

$$U^{*2}\left[\frac{C_{a^*}}{a^*}+\frac{dC_{a^*}}{da^*}\right]<2, \qquad \left[\Omega^{*2}+\left(U^{*2}\frac{C_{a^*}}{a^*}-1\right)\left(U^{*2}\frac{dC_{a^*}}{da^*}-1\right)\right]>0. \quad (4.29)$$

4.5 Numerical Validation

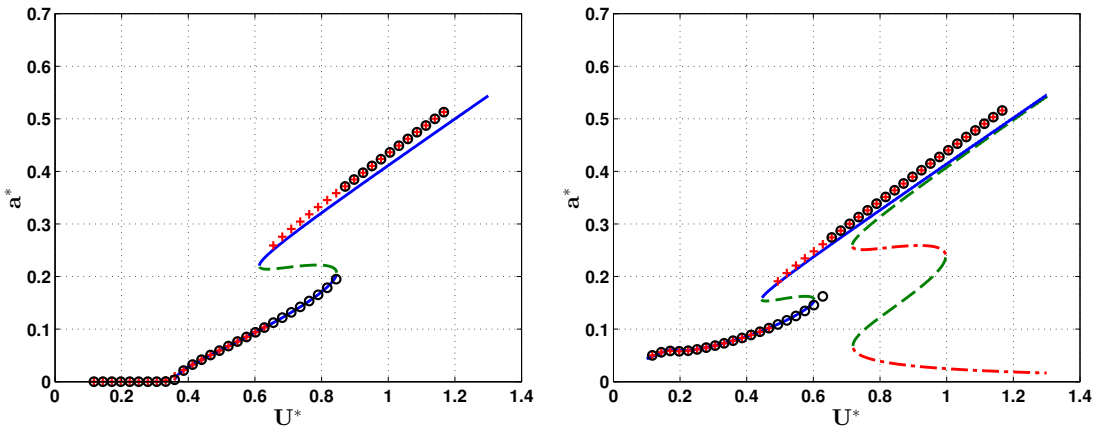

(a) (b)

Figure 4.2: Variation of the dimensionless amplitude of the response with the dimensionless wind speed: (a) without base excitation and (b) with base excitation. Lines represent analytical results: (solid) for stable solutions, (dash-dot) for quasi-periodic solutions and (dash) for saddles. Markers represent numerical results for the periodic responses only: (circle) for forward sweep and (plus) for backward sweep.

To validate the asymptotic analytical solutions, the results of the perturbation analysis are compared to a numerical integration of the equations of motion. Two sets of results are presented here to validate the solution with and without the base excitation term as depicted in Fig. 4.2 (a) and (b), respectively. Results presnetd in Fig. 4.2 are obtained for a harvester with a bluff body of a trapezoidal cross-section

(cross-stream rear to front face ratio 3/4, depth to front face ratio 1) whose normal aerodynamic force can be presented using a seventh order polynomial with coefficients given as $A_1 = 2.79$, $A_2 = 0$, $A3 = -84.5$, $A_4 = 0$, $A_5 = 1.2388 \times 10^3$, $A_6 = 0$, and $A_7 = -4.994 \times 10^3$. For the combined loading case, Fig. 4.2 (b), the dimensionless base displacement parameter is set to $|\bar{y}_b|^* = 4.35 \times 10^{-2}$ with $\sigma = 0$.

The results in Fig. 4.2 show excellent agreement between the analytical and numerical solutions with and without base excitations and for both branches of solutions generated by forward and backward sweeps of wind speed. This demonstrates the accuracy of the analytical approximation and its ability to predict the periodic responses of the harvester and the various bifurcations occurring in the parameters space. Specifically, it can be clearly seen that for the case considered here, and in the absence of the base excitation, the fixed points undergo a supercritical Hopf bifurcation near $U^* = 0.38$. As a result, the static solution loses stability giving way to a dynamic periodic solution whose amplitude increases with the wind speed. Near $U* = 0.82$ the dynamic solution undergoes a cyclic fold bifurcation and the response jumps to a larger-orbit period solution. Further increase in $U*$ causes a smooth increase in the harvester's output following the large orbit branch of solutions.

4.6 Response in the Absence of Base Excitations

When the harvester is subjected to flow excitations only, i.e., $|\bar{y}_b|^* = 0$, the response equation reduces to

$$U^{*2}\frac{C_{a^*}}{a^*} - 1 = 0, \tag{4.30}$$

with stable limit cycle solutions existing when

$$U^{*2}\frac{dC_{a^*}}{da^*} - 1 < 0. \tag{4.31}$$

Equation 4.30 contains only the aerodynamic constants A_n characterizing the cross section of the bluff body, while all the other geometric, mechanical, and electrical properties of the harvester are contained within the parameter, U^*. This leads to the important conclusion that the response of all galloping harvesters having the same aerodynamic constants (bluff body) can be described by a universal curve in the plane $U^* \times a^*$ irrespective of the other design parameters.

Figure 4.3 shows examples of normal force coefficient plots and the corresponding universal response curves of the harvester. To obtain the universal response curve of a certain bluff body, static wind tunnel tests are first conducted to characterize the cross-section by constructing the normal force coefficient versus angle of attack curve. This curve is then approximated in the form of a polynomial function of $\alpha_0 \approx \dot{y}/U$ using curve fitting. Once the empirical coefficients, A_n, are obtained, Equation (4.30) is solved to generate the universal response curve in the plane $U^* \times a^*$. The stability of the solutions is assessed by utilizing Equation (4.31).

Four different possibilities for the universal response curve can occur as demonstrated in Fig 4.3. The first possibility occurs when $A_1 = \left.\frac{dC_{F_y}}{d\alpha_0}\right|_{\alpha_0=0} > 0$ and the C_{F_y} curve is concave upward. In this case, as shown in Fig. 4.3 (a), the Hopf bifurcation is supercritical resulting in a smooth transition from the zero equilibrium point $a^* = 0$ to the limit-cycle oscillation near U_0^* .

The second case occurs when $A_1 > 0$ and the C_{F_y} curve is concave downward. In this scenario, a subcritical Hopf bifurcation occurs as shown in Fig. 4.3 (b). The third

possibility occurs when $A_1 > 0$ and there is an inflection point in the C_{F_y} curve. In this case, oscillation hysteresis due to cyclic fold bifurcation can occur in the response curve as demonstrated in the interval between U_1 and U_2 in Fig. 4.3 (c). When this hysteresis occurs, depending on the actual values of aerodynamic coefficients A_n, the separation between the bifurcation points is directly proportional to the ratio ζ_T/μ [65]. A such, this interval vanishes when the total damping, ζ_T approaches zero. Finally, a fourth possibility occurs when $A_1 \leq 0$ which represents the case of a hard oscillator. In this case, two branches of limit cycle oscillations are born at U_0^*, as shown in Fig. 4.3 (c). By checking the stability, it is found that the lower branch is unstable while the upper branch is stable. In this situation, the harvester can oscillate only if large initial conditions are applied. The limit cycle solutions of the four scenarios can further understood by inspecting the phase portraits of the response for different intervals as shown in Fig. 4.3.

4.6.1 The Universal Curve

In the previous section, we noted the presence of a universal curve for galloping oscillators which is basically a curve in the $U^* \times a^*$ plane that is only sensitive to the geometry of the bluff body, but is otherwise invariant under any changes in the design parameters. This universal curve was initially identified by Novak [65] in 1969 for galloping oscillators. Here, we show that this universal relation can be extend for galloping energy harvesters even in the presence of base excitations. We also show that this curve is an invaluable tool which allows a simple and direct comparative analysis of the performance of galloping energy harvesters. Towards that end, we considered an experimental study of a galloping energy harvester with a square bluff body. Using static wind tunnel tests, we characterized the normal coefficient and

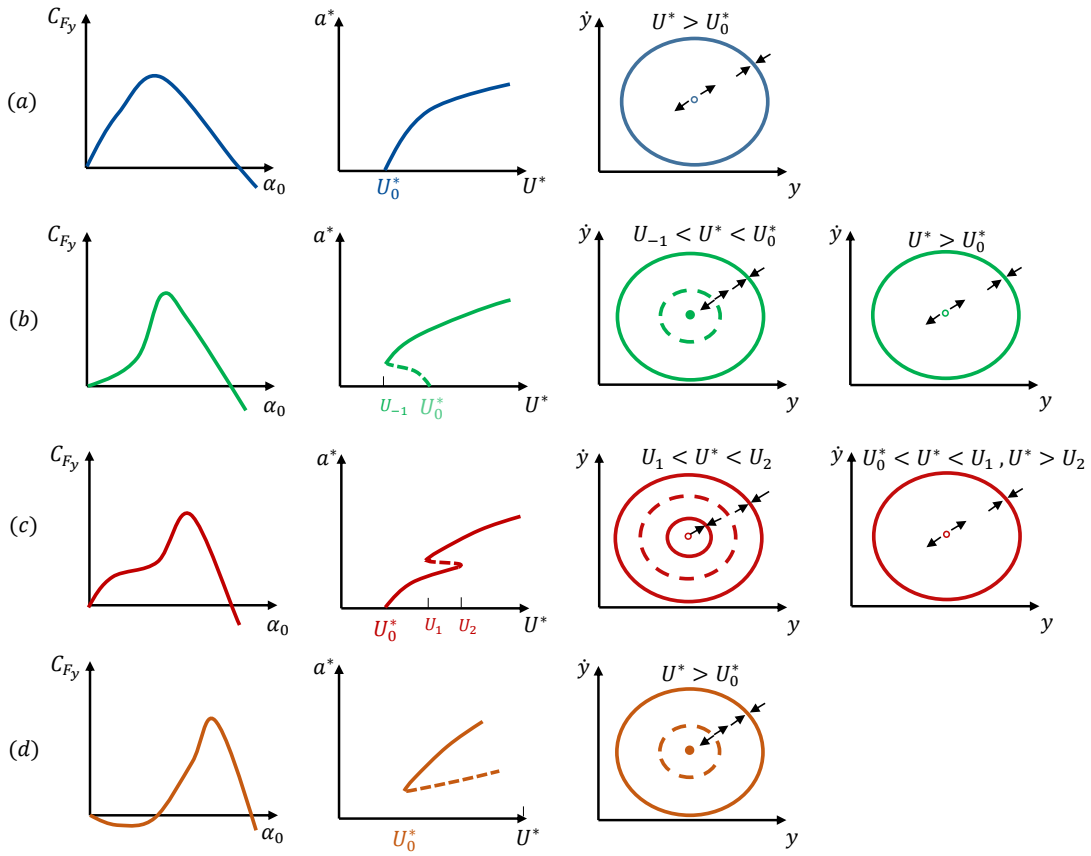

Figure 4.3: Typical Normal force coefficients and the corresponding types of harvester response and phase portraits: (a) $A_1 > 0$ and concave down, (b) $A_1 > 0$ and concave up, (c) $A_1 > 0$ with inflection point, and (d) $A_1 < 0$ and concave up. In phase portraits, solid-line represents a stable limit cycle while a dashed-line represents unstable limit cycle.

found that a cubic normal force coefficient of the form

$$C_{F_y} = A_1 \left(\frac{\dot{y}}{U}\right) - A_3 \left(\frac{\dot{y}}{U}\right)^3, \tag{4.32}$$

with the aerodynamic constants $A_1 = 2.5$ and $A_3 = 70$ is sufficient to accurately model the aerodynamic forces. In this case, Equation (4.30) can be solved to obtain the steady-state amplitudes of the transverse displacement, electric quantity, and

harvested power, P:

$$\frac{|y|}{y_0} = \frac{|r|}{r_0} = \frac{2}{\sqrt{3}}\sqrt{\frac{U^*}{A_3}\left(A_1 U^* - 1\right)}, \quad \frac{|P|}{P_0} = \left(\frac{|r|}{r_0}\right)^2, \tag{4.33}$$

where the corresponding dimensionless quantities are, respectively, given by

$$y_0 = \frac{\zeta_T D_t}{\mu}, \quad r_0 = \frac{\theta y_0}{C_p\sqrt{1+\alpha^2}} \text{ (piezoelectric)},$$
$$r_0 = \frac{\theta y_0}{L\sqrt{1+\alpha^2}} \text{ (electromagnetic)}, \quad P_0 = \frac{r_0^2}{R}.$$

Equation 4.33 is used to generate the universal curve for the non-dimensional displacement, electric quantity, and power for all galloping harvesters having the same square-sectioned bluff body as shown in Fig. 4.4. The figure clearly depicts the galloping speed of the harvester and the monotonic increase of the response amplitude with the reduced velocity within the typical range considered.

Next, to verify that this curve is actually universal for all energy harvesters with the same bluff body, experiments with five harvesters of different design parameters and a fixed bluff body are conducted. To change the other parameters of the harvester including its stiffness and damping, two beams with different materials are considered: Steel and Aluminum. For the Steel beam, three different lengths are used to study the influence of varying the stiffness in the range of 3.1 Hz to 4.1 Hz. The mechanical damping ratio was identified experimentally under short circuit condition using the logarithmic decrement method and is found to vary between 0.0039 and 0.0043. For the Aluminum beam, two different beam cuts are used to vary the frequency from 3.44 Hz to 4.04 Hz, and the estimated damping ratio is found to remain constant at 0.003. The wind speed is increased incrementally and the steady-state amplitude

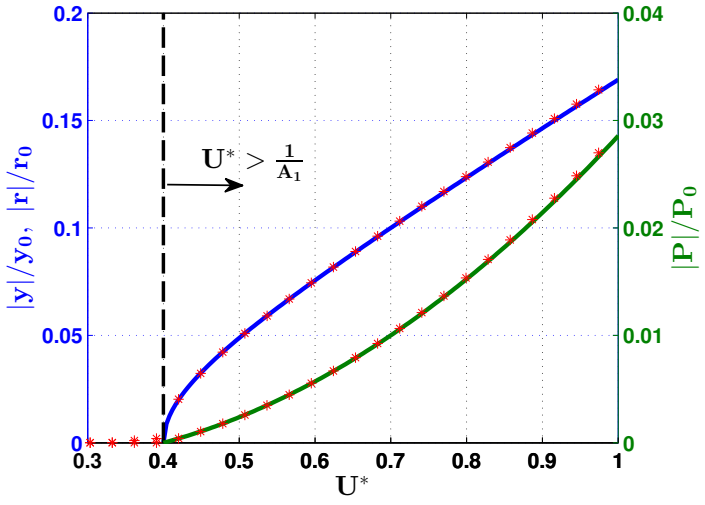

Figure 4.4: Universal response curves of the displacement, electric quantity, and power of a galloping harvester with a square-sectioned bluff body. Asterisks represent numerical results.

of the beam tip deflection is measured. The experimental results are then converted into the $U^* \times \frac{|y|}{y_0}$ plane as shown in Fig. 4.5 clearly indicating that the data collapse nicely onto effectively a single universal curve for all configurations.

An important note which can be deduced by inspecting Fig. 4.5 in view of Equation 4.33 is that the displacement measurements of a single beam, without electromechanical transduction components, can be used to estimate the aerodynamic force coefficients and construct the universal response curve of any cross sectional shape to avoid the static test measurements. This curve then, would be applicable to all harvesters with a bluff body of the same cross section and can be used to predict not only the displacement response, but also the voltage and output power for different scales, material properties, and circuit components provided that the quasi-steady assumption is valid and all inherent flow conditions remain the same.

As shown in Fig. 4.6, the universal curve also permits comparing performance of

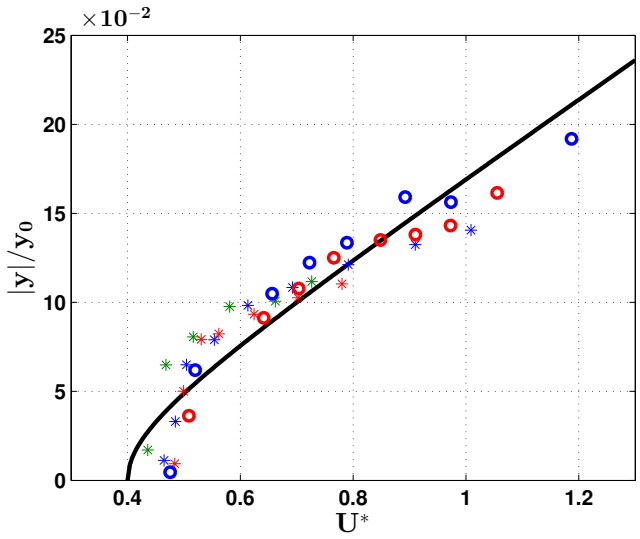

Figure 4.5: (Color online) Experimental universal response curve of galloping harvester with square-sectioned bluff body. Asterisks for Steel beam results: blue ($\omega_n = 3.09\ Hz$, $\zeta_m = 4.1 \times 10^{-3}$), green ($\omega_n = 3.59\ Hz$, $\zeta_m = 4.3 \times 10^{-3}$), and red ($\omega_n = 4.09\ Hz$, $\zeta_m = 3.9 \times 10^{-3}$). Circles for Aluminum beam results: blue ($\omega_n = 3.44\ Hz$, $\zeta_m = 3 \times 10^{-3}$), and red ($\omega_n = 3.44\ Hz$, $\zeta_m = 3 \times 10^{-3}$). Solid line represents theoretical results.

different bluff bodies by simply inspecting variation of y/y_0 versus U^* without the need to carry out experiments to determine the actual output voltage and power. For instance, by comparing the curves of Fig. 4.6, it can be directly concluded that there exists a set of mechanical and electrical design parameters for which an energy harvester with a squared-section bluff body will always outperform the ones with a D-shaped and triangular sections even when these are optimally designed. Similarly, it can be also concluded that, for larger wind speeds, a 53° isosceles-triangular section harvester can always be designed to outperform the D-shaped one if both were to be designed using the optimal parameters; whereas, the D-shaped section can always outperform the triangular one at the lower wind speeds provided that both are designed to operate optimally.

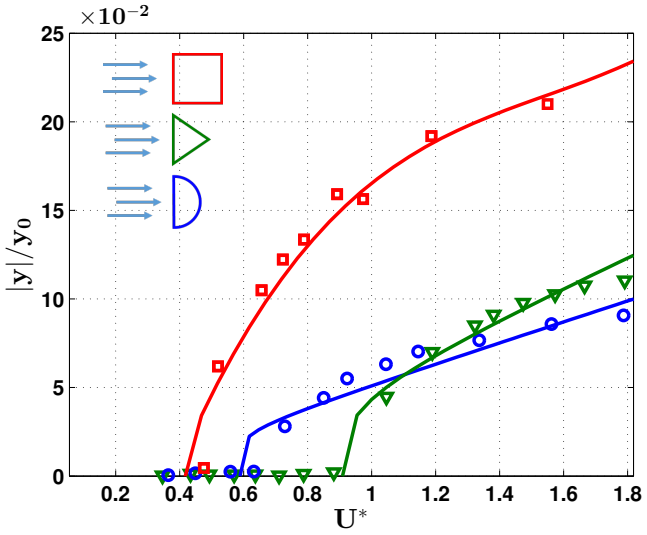

Figure 4.6: (Color online) Experimental universal response curves of galloping harvesters with different bluff bodies. Squares for a square section, circles for D-shaped section, and triangles for a 53° isosceles-triangular section. Solid lines represent theoretical predictions. In all cases, the bluff body is oriented with the flat surface facing the wind. The maximum turbulence intensity is 5%.

4.6.2 Optimization Analysis

The universal relationship of Equation (4.33) also provides significant insights into the optimal design parameters of galloping energy harvesters. The cut-in wind speed is governed by the simple relation $U^* A_1 = 1$. Hence, for a given bluff body characterized by A_1, reduction of the cut-in flow speed can be achieved by minimizing the quantity ζ_T/μ. This can be realized by minimizing the mechanical damping ratio or maximizing, μ, i.e., the flow to harvester's mass ratio. Similarly, the effects of different design parameters on the output power can be easily understood by studying their influence on U^* and P_0.

4.6.3 Optimal Harvesting Circuit Design Parameters

The influence of the electric parameters can be analyzed by investigating the electrical damping which contains the time constant ratio, α, and the electromechanical coupling, κ. The time constant ratio captures the influence of the electric load, R, while κ represents the strength of coupling between the mechanical and electrical subsystems. To study the influence of the electrical damping on the response of the harvester, one can rewrite the power expression in Equation (4.33) as

$$\frac{|P|}{P_0^*} = \frac{8}{3A_3} U_* \left(\frac{\zeta_e}{\zeta_m}\right) \left[A_1 U_* - \left(\frac{\zeta_e}{\zeta_m}\right) - 1\right]. \tag{4.34}$$

where $P_0^* = MD_t^2(\zeta_m \omega_n)^3/\mu^2$, and $U_* = \mu \bar{U}/\zeta_m$. By inspecting Equation (4.34), it becomes evident that the reduced cut-in wind speed of the harvester, U_c, can be obtained by setting the right hand side of the equation to zero; this yields $U_c = \frac{1}{A_1}\left[1 + \left(\frac{\zeta_e}{\zeta_m}\right)\right]$. As such, for a given design of the harvester, the minimum cut-in wind speed is attained when $\zeta_e = 0$, i.e. at short or open circuit for fixed κ. As the electric-to-mechanical damping ratio is increased, either by increasing the electromechanical coupling or as α approaches one as shown in Fig. 4.7 (b), the cut-in wind speed increases linearly as depicted in Fig. 4.7 (a).

Equation (4.34) can also be used to find the optimal electric-to-mechanical damping ratio at which maximum output power is harvested. This can be achieved by minimizing Equation (4.34) with respect to ζ_e/ζ_m which yields $\left(\frac{\zeta_e}{\zeta_m}\right)_{opt} = \frac{1}{2}(A_1 U_* - 1)$ at which the corresponding maximum output power P^* is $\frac{|P^*|}{P_0^*}_{opt} = \frac{2}{3A_3} U_* \left[A_1 U_* - 1\right]^2$.

As shown in Fig. 4.7 (c), the previous expressions reveal that the optimal ζ_e/ζ_m varies linearly with wind speed whereas the optimal power varies quadratically with it. Additionally, at the optimal value of ζ_e/ζ_m, the cut-in wind speed reduces to

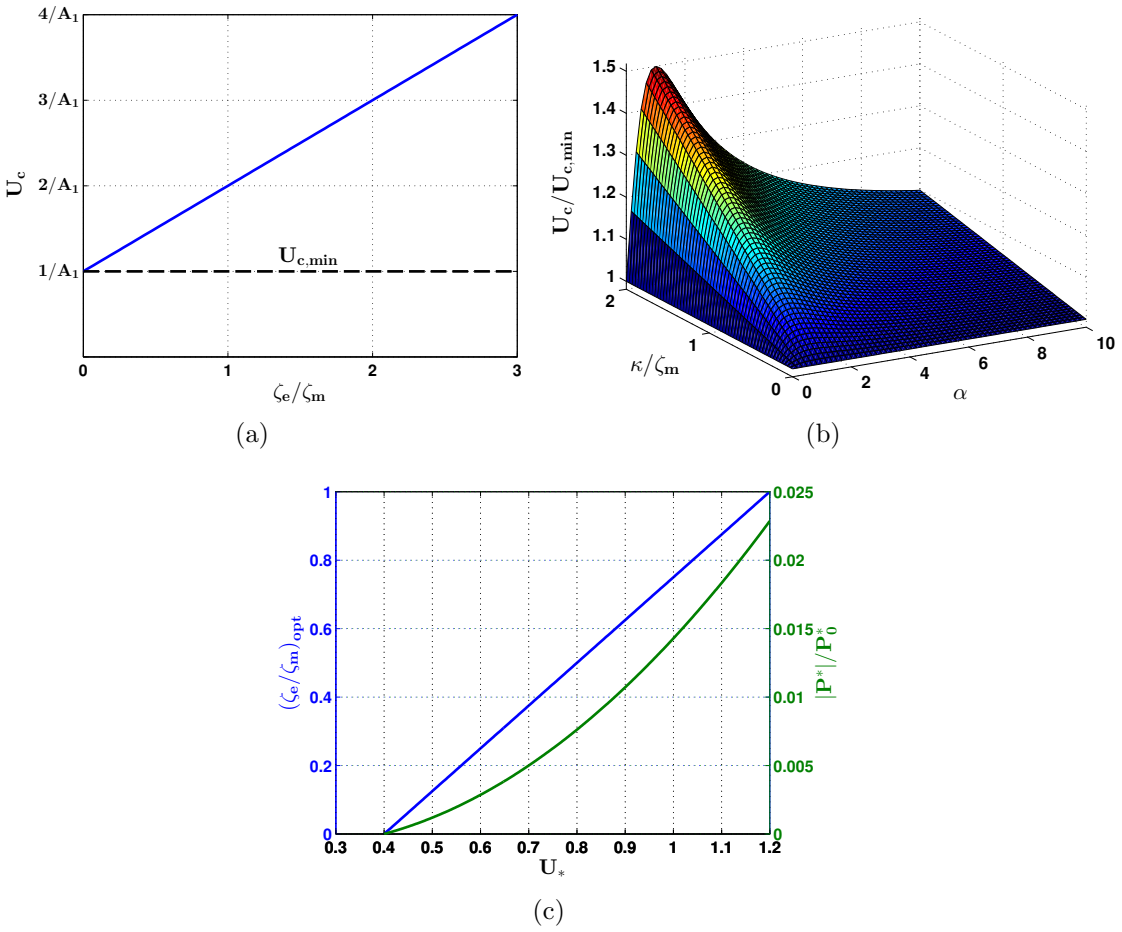

Figure 4.7: Variation of (a) the cut-in wind speed with the electric-to-mechanical damping ratio (b) the cut-in wind speed with time constant ratio and electromechanical coupling-to-mechanical damping ratio and (c) the optimal electric-to-mechanical damping ratio and the corresponding dimensionless maximum output power with wind speed. Results in (c) are obtained for square-sectioned bluff body with $A_1 = 2.5$ and $A_3 = 70$.

$U_c = 1/A_1$. This implies that, the optimal electric-to-mechanical damping ratio not only maximizes the harvested power but also minimizes the cut-in wind speed. However, from practical perspective, this is very hard to achieve because it requires additional circuit conditioning components to match the electric damping with its optimal value at each wind speed.

4.6.4 Optimal Electric Load

The electric load of the harvesting circuit represents one important parameter that is usually optimized to enhance the flow of energy from the environment. Optimizing the output power with respect to the electric load can be investigated by substituting $\zeta_e = \alpha\kappa/\left[2(1+\alpha^2)\right]$ back into the optimal electric-to-mechanical damping ratio relation and solving for α_{opt}. Analyzing the resulting solutions reveals that the ratio of the electromechanical coupling to the mechanical damping separates the optimization results into two distinctive regions. When $\left(\frac{\kappa}{\zeta_m}\right) < 2\left(A_1U_* - 1\right)$, the optimal load resistance embedded within the optimal time constant ratio, α_{opt}, and the corresponding maximum output power are given by

$$\begin{aligned} \alpha_{opt} &= 1, \\ \frac{|P^*|}{P_0^*} &= \frac{2}{3A_3}\left(\frac{\kappa}{\zeta_m}\right)U_*\left[A_1U_* - \frac{1}{4}\left(\frac{\kappa}{\zeta_m}\right) - 1\right]. \end{aligned} \tag{4.35}$$

In this region, the optimal load is a constant and represents that resulting from the traditional linear impedance matching. On the other hand, when $\left(\frac{\kappa}{\zeta_m}\right) > 2\left(A_1U_* - 1\right)$, the optimal load and the maximum output power are given by

$$\begin{aligned} \frac{1}{\alpha_{opt}} &= \frac{\left(\frac{\kappa}{\zeta_m}\right) \pm \sqrt{\left(\frac{\kappa}{\zeta_m}\right)^2 - 4\left(A_1U_* - 1\right)^2}}{2\left(A_1U_* - 1\right)}, \\ \frac{|P^*|}{P_0^*} &= \frac{2}{3A_3}U_*\left[A_1U_* - 1\right]^2. \end{aligned} \tag{4.36}$$

Here, the results of the optimization yield two different values for the optimal load, with both values providing the same maximum output power. Figure 4.8 (a) and (b) provide further insight into these optimization results. For small values of κ/ζ_m, the

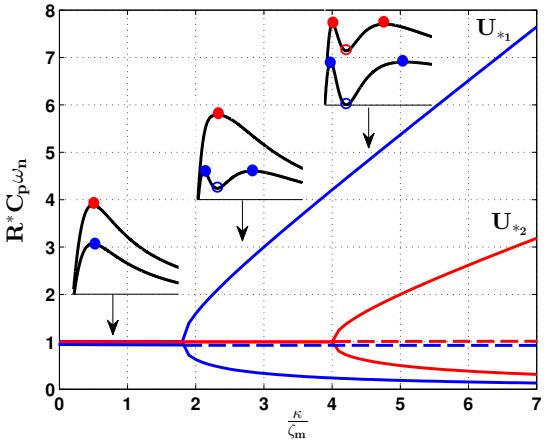

(a)

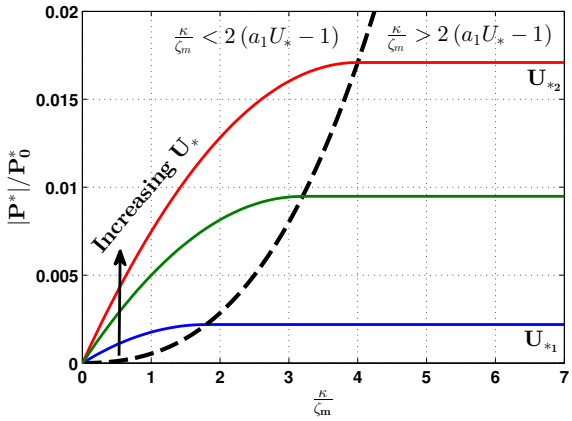

(b)

Figure 4.8: Variation of the optimal resistive load and the maximum output power with κ/ζ_m for different reduced wind speeds U_*: (a) Optimal resistive load. Solid-line represents maxima and dashed-lines represent minima. (b) Maximum harvested power. Dashed-lines represents the loci of optimal electromechanical coupling-to-mechanical damping ratio.

output power exhibits a single maximum. This maximum always occurs at the same optimal resistive load corresponding to $\alpha_{opt} = 1$, i.e. $R^* = 1/(C_p\omega_n)$ (piezoelectric) and $R^* = L\omega_n$ (electromagnetic). As κ/ζ_m is increased beyond the critical value $2\,(A_1U_* - 1)$, this maximum becomes a minimum, as represented by the dashed-lines in Fig. 4.8 (a), and two new optimal loads branch out. The value of these two loads

which depends on κ/ζ_m produces the same amount of maximum output power. As such, the harvesting circuit can be designed with two modes of operation; the high voltage/low current mode or the high current/low voltage mode by utilizing the small or the large optimal loads, respectively.

4.6.5 Optimal Electromechanical Coupling

Figure 4.8 (b) also reveals that, for a given U_*, the maximum output power increases with κ/ζ_m up to the critical value of $2\left(A_1 U_* - 1\right)$. This optimal coupling-to-damping ratio represents the optimal value beyond which the maximum attainable output power saturates and cannot be increased even if the electromechanical coupling is increased. This seemingly counterintuitive results can be explained by realizing that the electromechanical coupling acts as electric damping which, when increased significantly, shifts the cut-in flow speed into higher values as shown in Fig. 4.7 (a); thereby reducing the net energy transferred from the flow to the harvester.

4.6.6 Efficiency Estimation at the Optimal Conditions

The total aero-electro-mechanical efficiency of the harvester can be defined as the ratio of the generated electric power to the total input power available in a steady flow. The harvested power at the optimal electric design parameters is given by $|P^*|$ in Equation (4.36), while the total input wind power can be defined as $P_{in} = \frac{1}{2}\rho_a A_f U^3$, where A_f is the frontal area of the harvester in operation which can be related to tip deflection via $A_f = 2(D_t/2 + |y|)L_t$. After simplification, the total conversion

efficiency of the harvester can be written as

$$\eta = \frac{(A_1 U_* - 1)^2}{A_3 U_*^2 \left[2\sqrt{6}\left(\frac{\zeta_m}{\mu}\right)\sqrt{\frac{U_*}{A_3}(A_1 U_* - 1)} + 3\right]}. \tag{4.37}$$

For a given aerodynamic coefficients, A_1, and, A_3, which represent the shape of the bluff body and its ability to extract energy from the flow, i.e. its aeroelastic conversion efficiency, Equation (4.37) can be used to predict the total efficiency of the harvester in terms of two dimensionless parameters only; the wind speed U_* and the mechanical damping to mass ratio ζ_m/μ. Figure 4.9 depicts the total efficiency obtained for a harvester with a square-sectioned bluff body of $A_1 = 2.5$ and $A_3 = 70$. The figure shows that, for a given ζ_m/μ, there is an optimal reduced wind speed $\bar{U}$ at which the maximum efficiency of the harvester occurs. Furthermore, by inspecting the variation of the efficiency for a given $\bar{U}$, one realize that the efficiency increases significantly as the ratio ζ_m/μ decreases. This can be achieved by minimizing the mechanical damping in the system and/or by increasing the size of the bluff body while simultaneously reducing its mass.

4.7 Response in the Presence of Base Excitations:

In the presence of base excitations, the response equation is governed by only three dimensionless loading parameters; the flow U^*, the base displacement $|\bar{y}_b|^*$, and its frequency Ω^*. As such, the universal response of all harvesters of a given bluff body shape can be generated in the 4-dimensional parameter space $(a^* \times U^* \times |\bar{y}_b|^* \times \Omega^*)$ allowing the design of efficient harvesters subjected to concurrent loading. Two cases are discussed; the first studies the performance of the harvester under combined

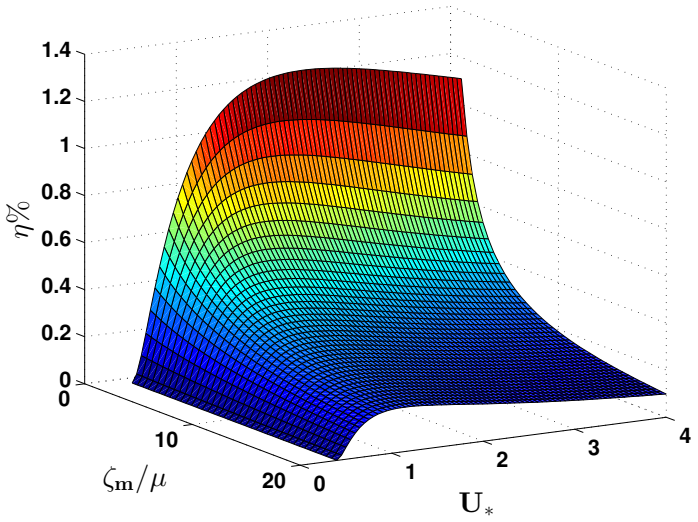

Figure 4.9: Variation of the total conversion efficiency with wind speed U_* and the mechanical damping to mass ratio ζ_m/μ. Results are obtained for square-sectioned bluff body with $A_1 = 2.5$ and $A_3 = 70$.

loading when the wind speed parameter is below the cut-in wind speed associated with the galloping instability, i.e. $U^* < 1/A_1$, while the second case studies the performance for wind speeds above the galloping speed $U^* \geq 1/A_1$.

4.7.1 Response below the cut-in wind speed:

When the velocity of the flow is below the galloping speed, i.e. $U^* < 1/A_1$, the self-sustained oscillations cannot be excited and the harvester's response only contains the frequency of excitation, Ω. As such, the response is always periodic with a frequency matching the excitation frequency. However, for a given wind speed, the amplitude of the harvester's response a^*, and, hence the output power can either be amplified or reduced depending on the sign of the aerodynamic damping represented by the polynomial $(-C_{a^*})$. More specifically, for small oscillations' amplitude, a^*, the posi-

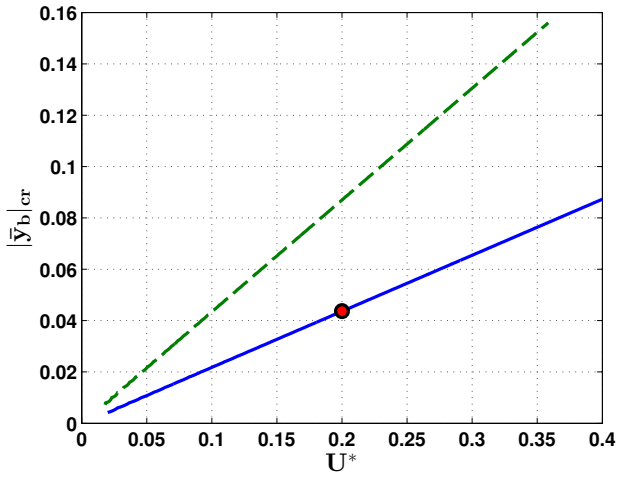

Figure 4.10: Variation of the critical base excitation loading term with wind speed U_*. (solid-line) for square-sectioned bluff body ($A_1 = 2.5$, $A_3 = -70$) and (dashed-line) for bluff body with trapezoidal section ($A_1 = 2.79$, $A_3 = -84.5$, $A_5 = 1.2388 \times 10^3$, $A_7 = -4.994 \times 10^3$).

tive low-order terms will dominate the negative high-order ones making the effective aerodynamic damping, C_{a^*}, negative. This, in turn, reduces the total damping in the system and causes response amplification. On the other hand, for larger amplitudes, a^*, the aerodynamic damping is positive which increases the total damping and causes response reduction.

To demonstrate the influence of the aerodynamic damping on the response of the harvester, a third-order polynomial expansion of C_{a^*} is considered, i.e. $C_{a^*} = A_1\left(\frac{a^*}{U^*}\right) + \frac{3}{4}A_3\left(\frac{a^*}{U^*}\right)^3$. Studying the sign of C_{a^*} reveals that, for a given wind speed, there is a critical base displacement, $|\bar{y}_b|_{cr}$ at which $C_{a^*} = 0$. At this critical value, the response of the harvester under base excitations is not influenced by the aerodynamic damping. For the case of $\Omega^* = 0$, this critical base displacement can be expressed as $|\bar{y}_b|_{cr} = \sqrt{-\frac{4A_1}{3A_3}}U^*$.

For further demonstration, a harvester of a square-sectioned bluff body with $A_1 = 2.5$

and $A_3 = -70$ is considered. If the harvester is subjected to flow velocity equals half of the cut-in wind speed, i.e. $U^* = 1/(2A_1) = 0.2$, the corresponding critical value of the base displacement is found to be $|\bar{y}_b|_{cr} = 4.36 \times 10^{-2}$, Fig. 4.10. Below this value the harvester's response is amplified due to the aerodynamics loading and vise versa.

Figure 4.11 depicts the frequency-response curves of the harvester for different values of the base displacement. Results are presented for both loading scenarios, i.e. base excitation only (dashed-line) and combined loading with $U^* = 1/(2A_1)$ (solid-line). Results clearly demonstrate that, for small values of $|\bar{y}_b|^*$, a harvester produces more power under the combined loading as compared to its output from vibratory excitations only. As the base excitation level is increased, the power amplification decreases until it approaches zero near $|\bar{y}_b|^* = |\bar{y}_b|_{cr}$. As the base excitation is increased further, response deamplification occurs. As a result, the harvester produces more power under vibratory excitations only as shown in Fig. 4.11 (b). It should be noted that the critical base displacement can also be defined for more complex bluff bodies requiring higher order polynomial expansion for the lift force. Such curve has been generated for a a bluff body with a trapezoidal-section, as shown by the dashed-line in Fig. 4.10.

Figure 4.12 shows different frequency response curves obtained at a fixed base excitation, when $|\bar{y}_b|^* < |\bar{y}_b|_{cr}$, and different wind speeds below the cut-in wind speed. As the wind speed is increased, the amplitude of the harvester's response increases from shifting the critical base displacement into higher values as shown in Fig. 4.10. When $U^* = 0$, the peak response at $\Omega^* \approx 0$ is simply given by $a^* = |\bar{y}_b|^*$. This means that the peak dimensionless response equals the dimensionless base displacement input. Moreover, in the case of a third order expansion of the aerodynamic coefficient, the

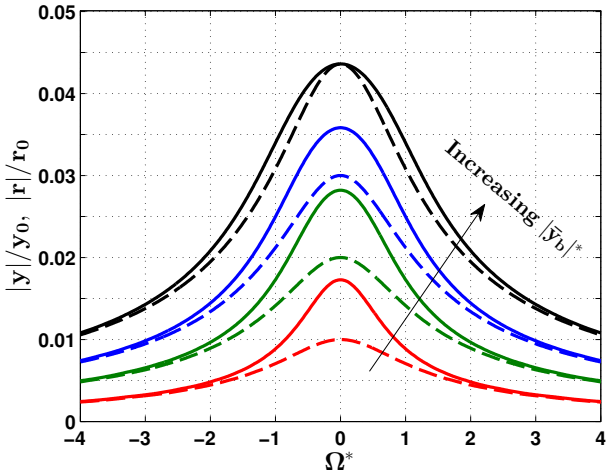

(a)

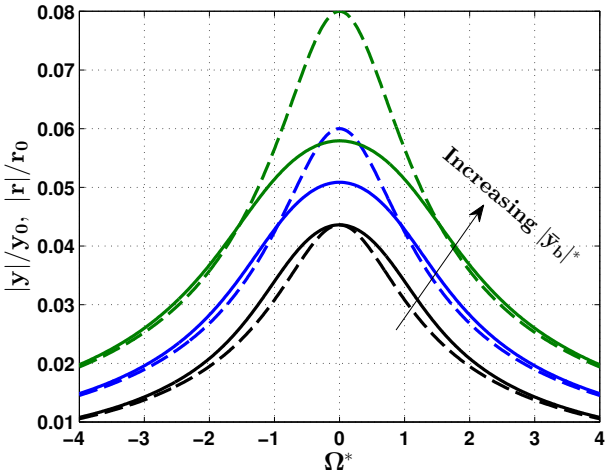

(b)

Figure 4.11: Frequency response curves for $U^* = 0.5/A_1 = 0.2$ and different base excitations $|\bar{y}_b|^*$. (a) below the critical excitation $|\bar{y}_b|_{cr}$, $|\bar{y}_b|^* = 0.01$, 0.02, 0.03, and 0.0436. (b) above the critical excitation $|\bar{y}_b|^* = 0.0436$, 0.06, and 0.08. Solid-line represents response from combined excitations and dashed-line represent response due to base excitation. Results are obtained for square-sectioned bluff body ($A_1 = 2.5$, $A_3 = -70$).

peak response equation is given by

$$\frac{3}{4U^*} A_3 a^{*3} + [1 - A_1 U^*]\, a^* = |\bar{y}_b|^*. \tag{4.38}$$

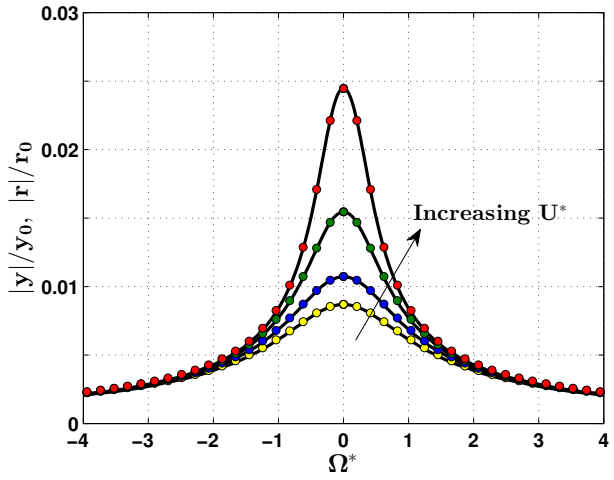

Figure 4.12: Frequency response curves for $|\bar{y}_b|^* = 8.7 \times 10^{-3}$ and different wind speeds $U^* = 0$, $0.25/A_1$, $0.5/A_1$, $0.75/A_1$. Results are obtained for a square-sectioned bluff body with $A_1 = 2.5$, $A_3 = -70$ with the rest of the A_n's equal to zero: analytically (solid-line) and numerically (circles).

Hence, one can define the amplification factor of the response under the combined loading with respect to that from base excitation only at the peak frequency as $f = a^*/|\bar{y}_b|^*$. Substituting f in Equation (4.38), the peak amplification factor equation can be given by

$$\frac{3}{4}A_3\frac{|\bar{y}_b|^{*2}}{U^*}f^3 + [1 - A_1U^*]\,f = 1. \tag{4.39}$$

Equation (4.39) is used to study the variation of the peak amplification factor with the input base displacement and wind speed as shown in Fig. 4.13. The contour lines in the figure represent all combinations of wind speed and base displacement that yield the same amplification factor with the line $f = 1$ representing the critical base displacement as function of wind speed. Figure 4.13 also serves as a tool to predict the peak response and the associated harvested power resulting from the combined loading for wind speeds below the cut-in wind speed by simply using $a^* = f \times |\bar{y}_b|^*$. At the cut-in wind speed, $U^* = 1/A_1$, Equation (4.39) can be solved for the

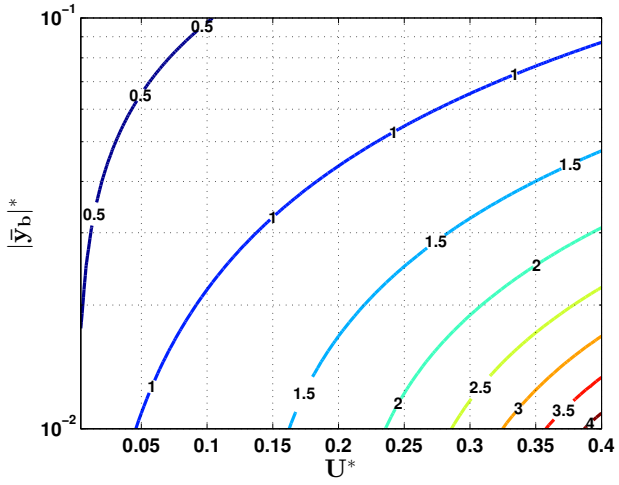

Figure 4.13: Contour plot of the peak amplification factor as function of wind speed U_* and base excitation $|\bar{y}_b|^*$.

peak amplification factor as $f = \sqrt[3]{\frac{4}{-3A_1A_3|\bar{y}_b|^{*2}}}$. This factor can reach up to 4.65 for the case shown in Fig. 4.12 indicating that the response of the harvester under base excitation can be amplified 4.65 times when the harvester is subjected to wind loading corresponding to the cut-in wind speed .

4.7.2 Response above the cut-in wind speed:

When the harvester is excited at its base and the wind speed is above the cut-in wind speed, $U^* > 1/A_1$, the response contains the excitation frequency, Ω, and the limit-cycle oscillation frequency, ω_n. Consequently, the response can be periodic or quasiperiodic in time depending on the stability of the fixed points, a^*. If a^* is stable then the solution is certainly periodic in time. Otherwise, the response can either undergo a secondary Hopf bifurcation which introduces additional frequencies to the dynamics leading to quasi-periodic responses, or other types of bifurcation that are of lesser importance to the present analysis (e.g. symmetry breaking, cyclic fold,

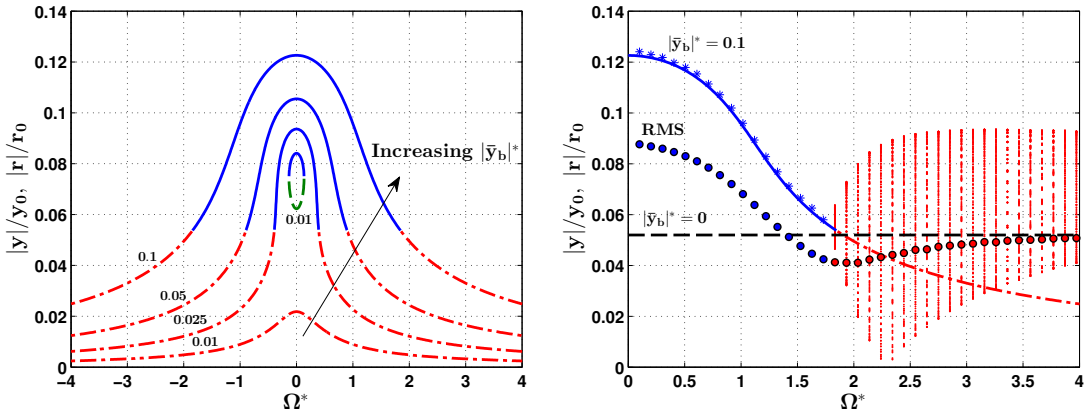

(a) (b)

Figure 4.14: (a) Frequency response curves for different base displacements $|\bar{y}_b|^*$: 0.01, 0.025, 0.05, 0.1 and fixed wind speed $U^* = 1.5/A_1$. Solid lines represent stable periodic solutions, dash-dot lines for unstable quasiperiodic solutions, and dashed line for saddle points. (b) The associated RMS value of the response: circles for $|\bar{y}_b|^* = 0.1$ and dashed-line for $|\bar{y}_b|^* = 0$. Results are obtained for a harvester with square-sectioned bluff body ($A_1 = 2.5$, $A_3 = -70$).

transcritical, etc.). The stability of the resulting solutions can be easily ascertained by the condition given in Equation (4.29) which depends on the three dimensionless parameters U^*, $|\bar{y}_b|^*$, and Ω^*.

Towards investigating the influence of these three parameters on the output of the harvester, the analytical approximation is used to generate the universal frequency-response curves of the harvester at $U^* = 1.5/A_1$ and different base displacements as depicted in Fig. 4.14 (a). Here, stable solutions are presented by solid lines while unstable solutions are presented by dash-dotted lines for the quasi-periodic solutions, and by dashed lines for unstable, physically unrealizable periodic orbits. Figure. 4.14 (a) demonstrates that, at a given $|\bar{y}_b|^*$ and for small $|\Omega^*|$, the response is always periodic where the free-oscillation component of the response is entrained by the forced component. This, in turn, results in a synchronized periodic response with

the response frequency matching the excitation frequency. On the other hand, when $|\Omega^*|$ is large, the periodic response loses stability via a secondary Hopf bifurcation, yielding quasiperiodic responses on either side of the symmetric frequency response curve.

Figure 4.14 (a) also demonstrates that for small values of $|\bar{y}_b|^*$, three branches of solution can coexist. The lower branch represents quasi-periodic responses that extend over the whole range of frequencies, while the higher amplitude solutions represent a branch of stable periodic orbits (upper branch) and a branch of unstable periodic orbits (lower branch) which collide and destruct each other in two cyclic fold bifurcations on either side of $\Omega^* = 0$. As $|\bar{y}_b|^*$ increases, only a single branch of solutions exists for all values of Ω^*. This branch is periodic near $\Omega^* = 0$ but becomes quasi-periodic as $|\Omega^*|$ becomes large. Evidently, the bandwidth of frequencies associated with periodic solutions increases with $|\bar{y}_b|^*$.

From a performance perspective, it should be noted that the total harvested average power will be maximum at resonance, $\Omega^* = 0$, and minimum near the frequency where a transition from stable to unstable response occurs. This can be seen by inspecting the associated RMS value of the response as depicted by circles in Fig. 4.14 (b). Far away from resonance, the average power corresponding to the quasiperiodic response approaches that resulting from aerodynamic loading only as presented by the $|\bar{y}_b|^* = 0$ dashed-line in Fig. 4.14 (b).

The analytical approximation can also be used to study the peak response at resonance, $\Omega^* = 0$, and generate the universal response curves for different U^* and $|\bar{y}_b|^*$ as shown in Fig. 4.15 (a). It is evident that, for the considered range of parameters, the harvester's response under the combined loading increases with U^* and $|\bar{y}_b|^*$. To measure the effective improvement in performance of the integrated harvester above

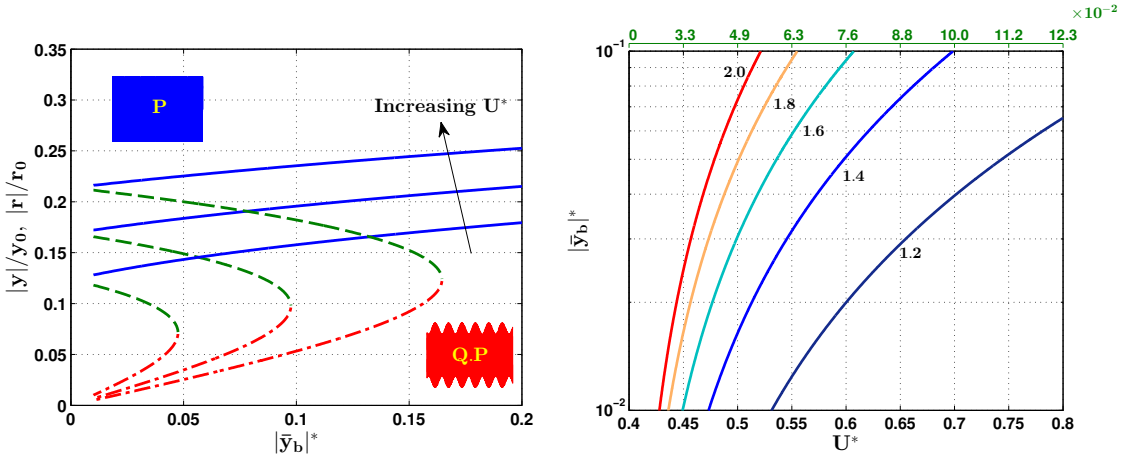

Figure 4.15: (a) Universal response curves as function of base displacement $|\bar{y}_b|^*$ and different wind speeds $U^* = 2/A_1$, $2.5/A_1$, $3/A_1$ for $\Omega^* = 0$. Solid lines represent stable periodic solutions, dash-dot lines for unstable quasiperiodic solutions, and dashed line for saddle points. (b) Contours of the peak amplification factor as function of base displacement $|\bar{y}_b|^*$ and wind speed U^*. Results are obtained for a harvester with square-sectioned bluff body ($A_1 = 2.5$, $A_3 = -70$).

the cut-in wind speed, a new peak amplification factor can be defined as the ratio between the responde under combined loading and the response from galloping excitation only. For the third-order expansion case, these are given by Equation (4.39) and Equation (4.33), respectively. Figure. 4.15 (b) depicts contours of the peak amplification factor as function of U^* and $|\bar{y}_b|^*$. For a given combination of loading conditions, the response of the harvester can be estimated by multiplying the corresponding amplification factor with the response resulting from galloping which is given by the top-axis for each wind speed.

Chapter 5

Modeling and Analysis Under Flutter and Base Excitations

This Chapter investigates the transduction of a piezoaeroelastic energy harvester under the combination of vibratory base excitations and aerodynamic loadings. The harvester which consists of a rigid airfoil supported by nonlinear flexural and torsional springs is placed in an incompressible air flow and subjected to a harmonic base excitation in the plunge direction. To capture the qualitative behavior of the harvester, a five-dimensional lumped-parameter model which adopts nonlinear quasi-steady aerodynamics is used. A linear stability analysis is carried out to determine the flutter speed of the harvester. A center manifold reduction is implemented to reduce the full model into one nonlinear first-order ordinary differential equation. The normal form of the reduced system is then derived to study slow modulation of the response amplitude and phase near the flutter instability. Subsequently, the analytical solution is used in conjunction with numerical simulations to investigate the harvester's performance below and above the flutter speed.

5.1 Model Formulation

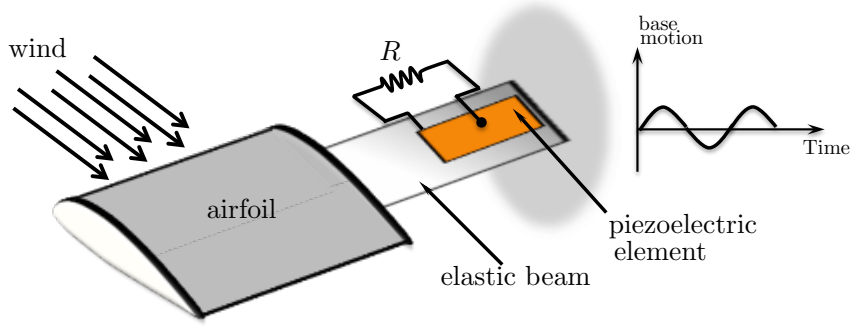

Figure 5.1: Schematic of piezoaeroelastic energy harvester.

A piezoaeroelastic energy harvester, which is generally placed on a structure can also undergo vibrations due to external base excitations. To shed some light onto the response behavior of the harvester under the combined loading, we consider an energy harvester similar to the one shown in Fig. 5.1. The external vibratory excitation is applied at the clamped end. The qualitative dynamics of the harvester can be captured using a lumped-parameter three-degree-of-freedom (two mechanical and one electrical) model as shown in Fig. 5.2. The harvester consists of a typical rigid airfoil supported by hardening flexural and torsional springs with stiffness, K_h, and, K_α, respectively, and the corresponding structural damping coefficients C_h, and, C_α. The airfoil has a mass, m_W, a mass moment of inertia, I_α, and is allowed to pitch about the elastic axis with an angle, α, positive nose up; and to plunge, or translate vertically, a distance, h, positive downward. The elastic axis is located at a distance, a, from the mid-chord, while the center of mass is located at a distance, χ_G, from the elastic axis. Both distances are positive when measured towards the trailing edge of the airfoil. The harvester is subjected to an external harmonic base motion, z, in the plunge direction, and placed in an incompressible uniform air flow with mean flow speed, U.

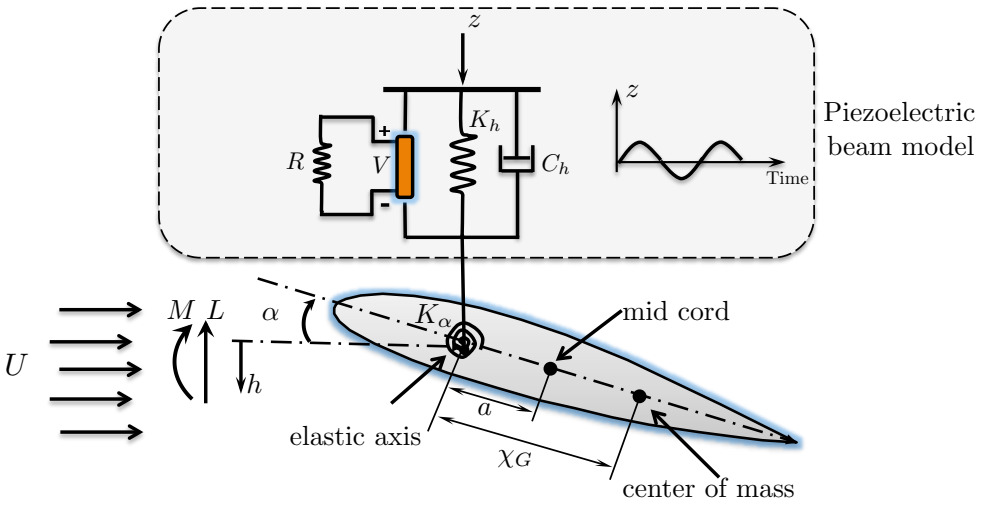

Figure 5.2: A schematic of a simplified model that captures the physical behavior of the energy harvester.

When the mean speed, U, exceeds the flutter speed, U_f, the harvester can undergo steady-state limit-cycle oscillations in addition to the oscillations induced by the base motion. These oscillations strain the piezoelectric element, which in turn, generates a voltage, V, across an electric load, R.

The non-dimensional equations governing the motion of this lumped-parameter system can be written as [66]:

$$\bar{h}'' + \chi_\alpha \alpha'' + 2\zeta_h\left(\bar{h}' - \bar{z}'\right) + \bar{F}_h - e_\theta \bar{V} = -\bar{L}, \tag{5.1a}$$

$$\alpha'' + \chi_h \bar{h}'' + 2\zeta_\alpha \alpha' + \bar{F}_\alpha = \bar{M}, \tag{5.1b}$$

$$\bar{V}' + e_R \bar{V} + (\bar{h}' - \bar{z}') = 0, \tag{5.1c}$$

where the prime denotes a derivative with respect to the non-dimensional time, τ, defined as $\tau = U_f t/b$, where, b, is the half chord length, and t is time. Here, $\bar{h} = h/b$, and, $\bar{z} = z/b$, are the non-dimensional plunge and base motion, respectively.

The first of the three equations, Equation (5.1a), represents the dynamics of the plunging mode which frequency is given by $\omega_h = (K_h/m_T)^{1/2}$ with m_T being the total mass of the airfoil and supporting structure. The equation accounts for the inertial forces in the plunge direction (first term); the inertial coupling to the pitch mode due to the static imbalance presented in χ_α (second term); the mechanical dissipative forces in the plunge direction presented in the damping ratio, $\zeta_h = \frac{C_h}{2\omega_h m_T \bar{u}_f}$ (third term), where $\bar{u}_f = U_f/(\omega_h b)$ is the non-dimensional flutter speed; and the nonlinear restoring forces (fourth term) which can be expressed in the polynomial form

$$\bar{F}_h = \frac{(\bar{h} - \bar{z})}{\bar{u}_f^2}(1 + f_h(\bar{h} - \bar{z})^2), \tag{5.2}$$

where f_h is a constant representing the hardening nonlinearity in the plunging mode. Furthermore, the equation accounts for the backward coupling due to the piezoelectric damping forces (fifth term). This is presented in the coefficient $e_\theta = \frac{\theta^2}{m_T \omega_h^2 C_p \bar{u}_f^2}$, where θ is the piezoelectric coupling and C_p is the piezoelectric capacitance.

The aforementioned internal forces in the plunge direction balance the lift force, $\bar{L}$, induced by the air flow. In this paper, this force is modeled using a quasi-steady approximation where the temporal aerodynamic loads depend only upon the effective angle of attack induced by the instantaneous motion. Using the stall model, NACA 0012, to represent the nonlinear loads, the non-dimensional aerodynamic lift can be written as [67]

$$\bar{L} = c_{L\alpha} \left(\frac{U}{U_f} \right)^2 \left(\alpha_{eff} - c_3 \alpha_{eff}^3 \right),$$

where $c_{L\alpha}$ is related to the aerodynamic lift coefficient and c_3 is a nonlinear parameter associated with the lift curve derived from wind tunnel tests. The effective angle of attack is given by

$$\alpha_{eff} = \alpha + \frac{1}{U/U_f}\bar{h}' + \frac{1/2 - \bar{a}}{U/U_f}\alpha'. \tag{5.3}$$

where $\bar{a} = a/b$. The second of the three equations, Equation (5.1b), represents the dynamics of the pitch mode which linear frequency is given by $\omega_\alpha = (K_\alpha/I_\alpha)^{1/2}$. The equation accounts for the inertial moment in the pitch direction (first term); the inertial coupling to the plunge mode due to the static imbalance, χ_h, (second term); the mechanical dissipative moment in the pitch direction (third term) presented in the damping ratio, $\zeta_\alpha = \frac{C_\alpha}{2\omega_h I_\alpha \bar{u_f}}$; and the nonlinear restoring moment (fourth term) which can be expressed in the polynomial form

$$\bar{F}_\alpha = \left(\frac{\omega_\alpha}{\omega_h \bar{u}_f}\right)^2 (\alpha + f_\alpha \alpha^3),$$

Here, f_α is a constant representing the hardening nonlinearity in the pitch mode. Note that the effect of piezoelectric backward coupling on the pitch motion is neglected. Again, these internal moments balance the external aeroelastic moment induced by the flow and given by

$$\bar{M} = \frac{1/2 + \bar{a}}{r_\alpha^2}\bar{L},$$

where $r_\alpha^2 = I_\alpha/(m_T b^2)$ is the radius of gyration of the cross section.

The third equation, Equation (5.1c), represents the harvesting circuit dynamics which assumes a purely resistive load, R, and no energy harnessed from the pitch motion. In this equation, $\bar{V} = V/V_c$ represents the non-dimensional voltage, where $V_c = \theta b/C_p$; and e_R is a time constant ratio given by $e_R = \frac{1}{C_p R \omega_h \bar{u}_f}$.

5.2 Flutter Speed

We find it convenient to convert the equations of motion into a standard Jordan canonical form (linearly decoupled). To that end, we introduce the state vector $X = [x_1, x_2, x_3, x_4, x_5]^T \equiv [\alpha, \alpha', \bar{h}, \bar{h}', \bar{V}]^T$. This yields

$$X' = F(X; \bar{z}). \tag{5.4}$$

where the components of the vector field $F(X; \bar{z})$ are defined in Appendix A. The right-hand side of Equation (5.4) is further expanded in a Taylor series around the system's fixed point, $X_0 = 0$, to obtain

$$X' = AX + G(X, \bar{z}), \text{ where } A = \left.\frac{\partial F}{\partial X}\right|_{X_0=0}, \text{and } G = F - A. \tag{5.5}$$

For a typical aeroelastic structure, the flutter phenomenon occurs at a wind speed, U_f, causing the structure to undergo limit-cycle oscillations as a result of a Hopf bifurcation. To study the dynamic response of the system near the bifurcation point, U_f, we introduce a perturbation parameter, δ, such that $U/U_f = 1/(1-\delta)$ and substitute it into Equation (5.5). For small values of δ, Equation (5.5) can be further expanded in a Taylor series around $\delta = 0$ to obtain

$$X' = A_0 X + \delta B X + G_0(X, \bar{z}), \tag{5.6}$$

where

$$A_0 = A\big|_{\delta=0}, \; B = \left.\frac{dA}{d\delta}\right|_{\delta=0}, \text{ and } G_0 = G\big|_{\delta=0}.$$

Next, we introduce the similarity transformation $Y = P^{-1}X$, where

$$Y = [y_1, y_2, y_3, y_4, y_5]^T,$$

and P is a transformation matrix obtained from the eigenspace of A_0, such that $P^{-1}A_0P = J$, where J is the Jordan canonical form of A_0. This yields

$$Y' = JY + \delta P^{-1}BY + P^{-1}G_0(PY, \bar{z}). \tag{5.7}$$

By construction of the state-space, some of the states of the vector Y can be directly related to each other such that y_2 is the complex conjugate of y_1, and y_4 is the complex conjugate of y_3. Hence, by determining y_1 and y_3, y_2 and y_4 can be easily obtained.

Equation (5.7) can now be used to analyze the linear stability of the system and determine the flutter speed which can be obtained by monitoring the eigenvalues of the Jacobian matrix A_0 of Equation (5.6) when evaluated at the equilibrium points. The parameters used in the simulations are based on the piezoaeroelastic energy harvester described in a prior work of Erturk et al. [49], and are listed in Table 5.2.

At the flutter speed, the Jacobian matrix $A_0 = J$ has five eigenvalues. Two pairs of complex conjugate eigenvalues corresponding to the dynamics of the aeroelastic system. One of those pairs represents purely imaginary eigenvalues, $\lambda_{1,2} = \pm j\omega_0$, resulting from the flutter condition, where ω_0 represents the frequency of the born limit cycle just beyond the flutter speed. The other pair, $\lambda_{3,4}$, consists of two complex conjugate eigenvalues with negative real parts corresponding to the other two states of the aeroelastic system. The fifth eigenvalue, λ_5, is always real and negative and corresponds to the dynamics of the harvesting circuit.

Table 5.1: Geometric and material properties of the piezoelectric flutter energy harvester (numerical validations).

Physical properties			
$b[m]$	0.125	ζ_α	0.0036
$a[m]$	-0.0625	$K_h[N/m]$	2370
$\chi_G[m]$	0.0325	f_h	0.0014
χ_h	1.0166	ζ_h	0.0043
χ_α	0.1001	$c_{L\alpha}$	0.1635
$m_W[kg]$	0.901	c_3	10.833
$m_T[kg]$	2.34	$C_p[\mu F]$	120
$I_\alpha[kg.m^2]$	0.0036	$\theta[mN/V]$	1.55
$K_\alpha[Nm/rad]$	0.848	$R[k\Omega]$	75
f_α	1.33		

Figure 5.3 (a) and (b) depict, respectively, variation of the real and imaginary parts of the first four eigenvalues with the air speed. As the speed is increased, the real part of the first pair of complex conjugate eigenvalues, $\lambda_{1,2}$, increases and approaches zero at the flutter speed, $U_f \approx 9.16m/sec$. The transversal crossing of the eigenvalues form the left- to the right-hand side of the complex plane represents transition from asymptotically stable, decaying response, to growing oscillations indicating the onset of a Hopf bifurcation. The reduction in the magnitude of the real part of the eigenvalues is accompanied by a reduction in the imaginary part corresponding to the oscillation frequency as depicted in Fig. 5.3 (b). For instance, the frequency of oscillation decreases from approximately 1.05 to approximately 0.42 at the onset of flutter. This signifies that the air flow reduces the effective stiffness of the system.

Once the flutter speed is determined, a numerical integration of Equations (5.1a-5.1c) is used to study time histories of the response just beyond it. Examples of the output voltage are presented in Fig. 5.4 for $U = 1.01U_f$ under harmonic base excitations of

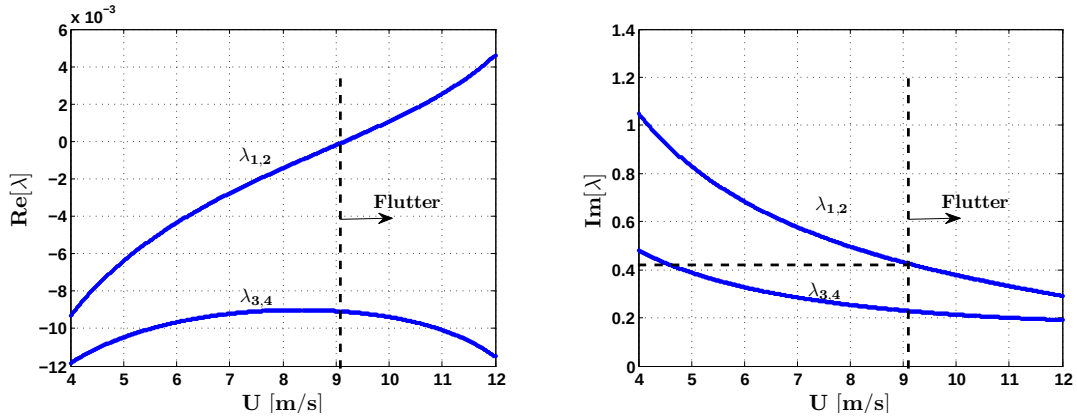

(a) (b)

Figure 5.3: Variation of the eigenvalues with the wind speed: (a) real part, and (b) imaginary part.

the form $\bar{z} = |\bar{z}|\cos(\Omega\tau)$. The corresponding root mean square (RMS) value which represents a better measure of the harvester's performance is also presented as dashed lines.

Figures 5.4 (a) represents the periodic output voltage of the harvester due to flutter only in the absence of base excitation. Figures 5.4 (b) and 5.4 (c) are obtained for equal values of the base excitation magnitude, $|\bar{z}| = 2.5 \times 10^{-3}$, and at different frequencies of $\Omega = 0.97\omega_0$ and $\Omega = 1.075\omega_0$, respectively. Time histories demonstrate the transition from almost periodic response of the harvester (small-amplitude modulation) to a two-period quasi-periodic response (large-amplitude modulation). The amplitude modulation causes the RMS value of the voltage to drop significantly even when similar peak voltages are realized. Quite interestingly, as depicted in Fig. 5.4 (d), when the base excitation is reduced to half its original value while keeping the excitation frequency constant at $\Omega = 1.075\omega_0$; the RMS voltage stays almost constant around 10 Volts when compared to Fig. 5.4 (c). This clearly indicates that, due to the

quasiperiodicity of the response, increasing the input excitation does not necessarily increase the RMS output voltage of the harvester.

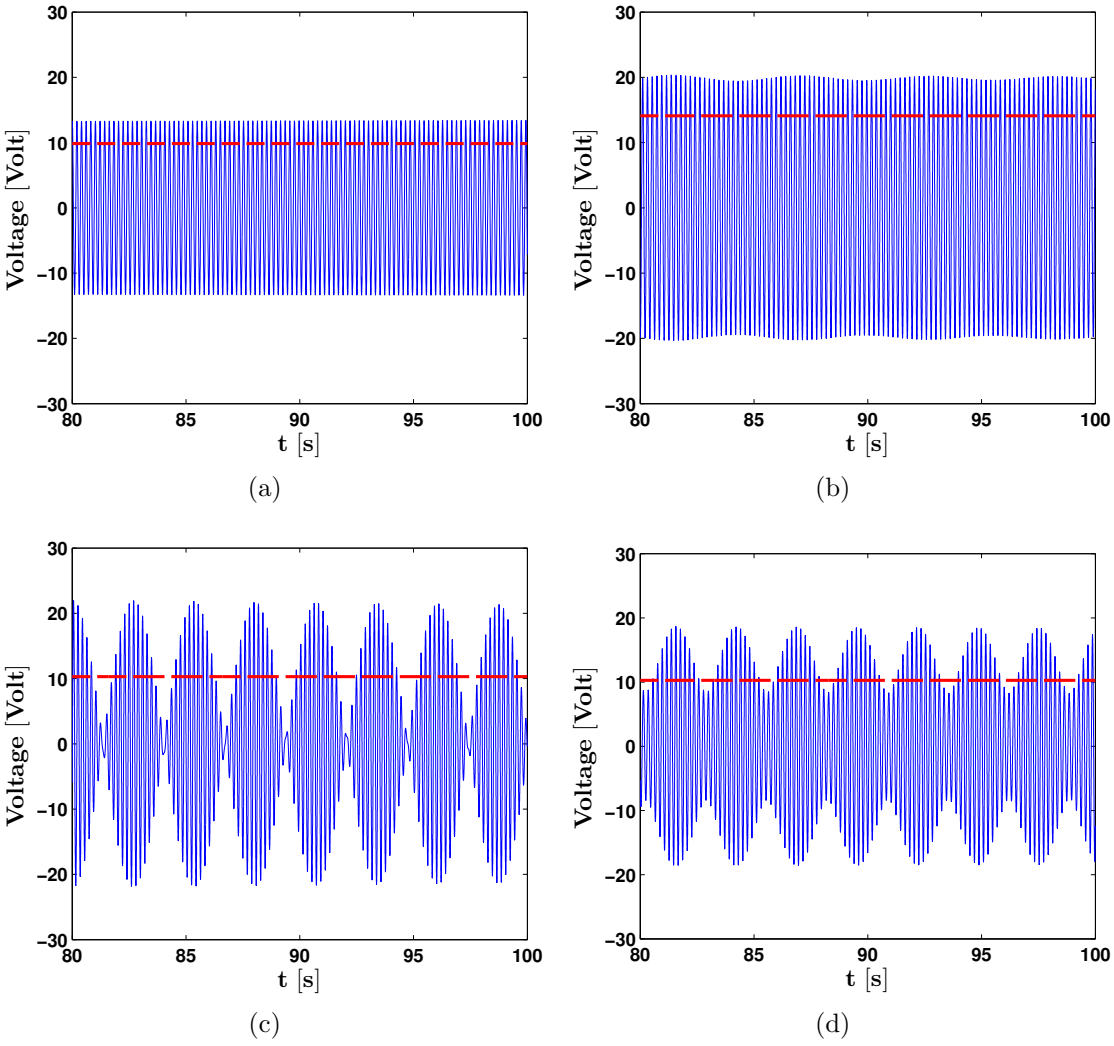

Figure 5.4: Time history of the output voltage and the corresponding RMS value for $\delta = 0.01$. (a) $|\bar{z}| = 0$, (b) $|\bar{z}| = 2.5 \times 10^{-3}$ and $\Omega = 0.97\omega_0$, (c) $|\bar{z}| = 2.5 \times 10^{-3}$ and $\Omega = 1.075\omega_0$, and (d) $|\bar{z}| = 1.25 \times 10^{-3}$ and $\Omega = 1.075\omega_0$.

The preceding examples reveal that the nature of the harvester's response is very complex to be understood based on a purely numerical study and simple time histories. To gain a deeper physical insight into the qualitative behavior of the harvester,

we reduce the order of the system using a center manifold reduction of Equation (5.7). The reduced system is then transformed into its simplest normal form using a coordinate transformation [68]. This permits the development of two first-order nonlinear ordinary differential equations that are better suited to study slow modulation of the amplitude and phase of the harvester's voltage output.

5.3 Approximate Analytical Solution

In general, analysis of the dynamics of an n-dimensional continuous system near one of its fixed points can be reduced to the analysis of the dynamics on its center manifold. At the flutter speed, $\delta = 0$, the origin, $X_0 = 0$, becomes a nonhyperbolic fixed point. Hence, there exists a local center manifold for the nonlinear system of Equation (5.7) near X_0. Moreover, since none of the eigenvalues of this fixed point lie in the right-half of the complex plane, the long-time dynamics of the system can be described by the dynamics on the center manifold, thereby reducing the dimensionality of the system. For the system at hand, this reduces the five-dimensional system of Equation (5.7) into one first-order nonlinear differential equation that approximates the system's dynamics. This equation can be further simplified by finding its normal form which represents a coordinate transformation in which the dynamics takes its simplest form.

Since the procedure associated with obtaining this reduced and simplified system is not the main scope of the work and tends to distract the reader from the main objective of this Chapter, we present the analysis in Appendices B and C. Upon completion of the analysis, an approximate solution for the transformed state $y_1(\tau)$

can be written in the following general form:

$$y_1(\tau) = a(\tau)\cos(\Omega\tau + \beta(\tau)), \tag{5.8}$$

where Ω is the base excitation frequency, and, $a(\tau)$ and $\beta(\tau)$ represent, respectively, the real-valued amplitude and phase of the systems' oscillations which, after keeping the slowly varying terms, are governed by

$$a' = \alpha_1\delta a + \alpha_2 a^3 + (\alpha_3 + \sigma\alpha_4)|\bar{z}|\cos\gamma + \alpha_5 a|\bar{z}|^2 + \alpha_6|\bar{z}|^3\cos\gamma + \alpha_7 a^2|\bar{z}|\cos\gamma, \tag{5.9}$$

$$a\gamma' = (1-\sigma)\omega_0 a - (\alpha_3 + \sigma\alpha_4)|\bar{z}|\sin\gamma - \alpha_6|\bar{z}|^3\sin\gamma - \alpha_9 a^2|\bar{z}|\sin\gamma, \tag{5.10}$$

where $\sigma = \Omega/\omega_0 - 1$, $|\bar{z}|$ is amplitude of base excitation, $\gamma = (\beta - \sigma\omega_0\tau)$, and α_i are constants that depend on the system's geometric and material parameters.

At steady-state, the fixed points of Equations (5.9) and (5.10) correspond to the steady-state amplitude and phase of the periodic solutions of the original system of Equations (5.7). To find the fixed points, we set $a' = \gamma' = 0$ and solve Equation (5.9) and (5.10) numerically for the fixed points a_0 and γ_0. The stability of the resulting solutions can then be assessed by evaluating the eigenvalues of the Jacobain matrix associated with Equations (5.9) and (5.10). If all the eigenvalues of the Jacobian matrix are in the left-hand plane, then (a_0, γ_0) are stable and there exists a stable periodic solution such that

$$y_1(\tau) = a_0\cos(\Omega\tau + \gamma_0), \tag{5.11}$$

On the other hand, when two complex conjugate eigenvalues transversally cross the imaginary axis, the periodic solution loses stability giving way to a two-period solution

which can be quasi-periodic if the two periods are incommensurate.

With the knowledge of (a_0, γ_0), and using the transformation $X = PY$, the non-dimensional pitch, plunge, and output voltage of the harvester can be, respectively, related to y_1 via

$$\alpha(\tau) = |P(1,1)|a_0 \cos\big(\Omega\tau + \gamma_0\big), \tag{5.12}$$

$$\bar{h}(\tau) = |P(3,1)|a_0 \cos\big(\Omega\tau + \gamma_0\big), \tag{5.13}$$

$$\bar{V}(\tau) = |P(5,1)|a_0 \cos\big(\Omega\tau + \gamma_0\big), \tag{5.14}$$

where $|P(i,j)|$ represent the i,j-th elements of the transformation matrix P. The preceding analytical solutions represent a first-order approximation for the nonlinear response of Equations (5.1a-5.1c).

In the absence of the base excitation, the modulation equations take the simpler form

$$a' = \alpha_1 \delta a + \alpha_2 a^3, \tag{5.15}$$

$$a\gamma' = (1-\sigma)\omega_0 a, \tag{5.16}$$

which represents the normal form of a pitchfork bifurcation in the $a - \gamma$ plane or a Hopf bifurcation in the $y_1 - y_2$ plane. The steady-state amplitude of the response is obtained by sitting a' equals to zero. This yields

$$a_0 = 0, \qquad a_0 = \pm\sqrt{\frac{-\delta\alpha_1}{\alpha_2}} \tag{5.17}$$

The nontrivial solutions only exist when the quantity under the square root is positive. It turns out that for the set of parameters used in the simulation, $\alpha_1 > 0$ and $\alpha_2 < 0$. Hence, the nontrivial solutions only exist when $\delta > 0$, or when $U > U_f$. Such solutions

turn out to be stable indicating that the Hopf bifurcation is supercritical. As such, in the absence of the base excitation, the harvester is said to be self excited and generates periodic steady-state voltages with amplitude $|\bar{V}| = |P(5,1)|\sqrt{\frac{-\delta\alpha_1}{\alpha_2}}$ when $U > U_f$.

5.4 Validity of the Analytical Solution

Before delving into the response behavior of the harvester, we demonstrate the accuracy of the analytical approximation obtained via Equations (5.12-5.14) by comparing the analytical predictions with solutions obtained via numerical integration of the original equations of motion, Equations (5.1a-5.1c).

Figure 5.5 depicts a comparison between the analytical approximation (dashed lines) obtained via Equations (5.12-5.14) and the numerical solutions (solid lines) obtained using Equations (5.1a-5.1c) for increasing values of the wind speed represented by the bifurcation parameter, δ. Two cases are considered; the free response case in the absence of the external base excitation, and the forced case which shows the steady-state response due to a combination of aerodynamic and base excitations. The base displacement is set to $\bar{z} = 2.5 \times 10^{-3}\cos(\omega_0\tau)$ with a forcing frequency matching the oscillation frequency, ω_0 (primary resonance).

The steady-state amplitudes demonstrate good agreement between the analytical and numerical solutions for moderate values of δ. As δ increases away from $\delta = 0$, the analytical solution starts to deviate from the numerical integration due to the previous assumption that δ and σ are small, see Appendix B for details. As such, while analyzing the response of the harvester using the analytical approximation, it is important to bear in mind that the solutions acquired via the combination of center

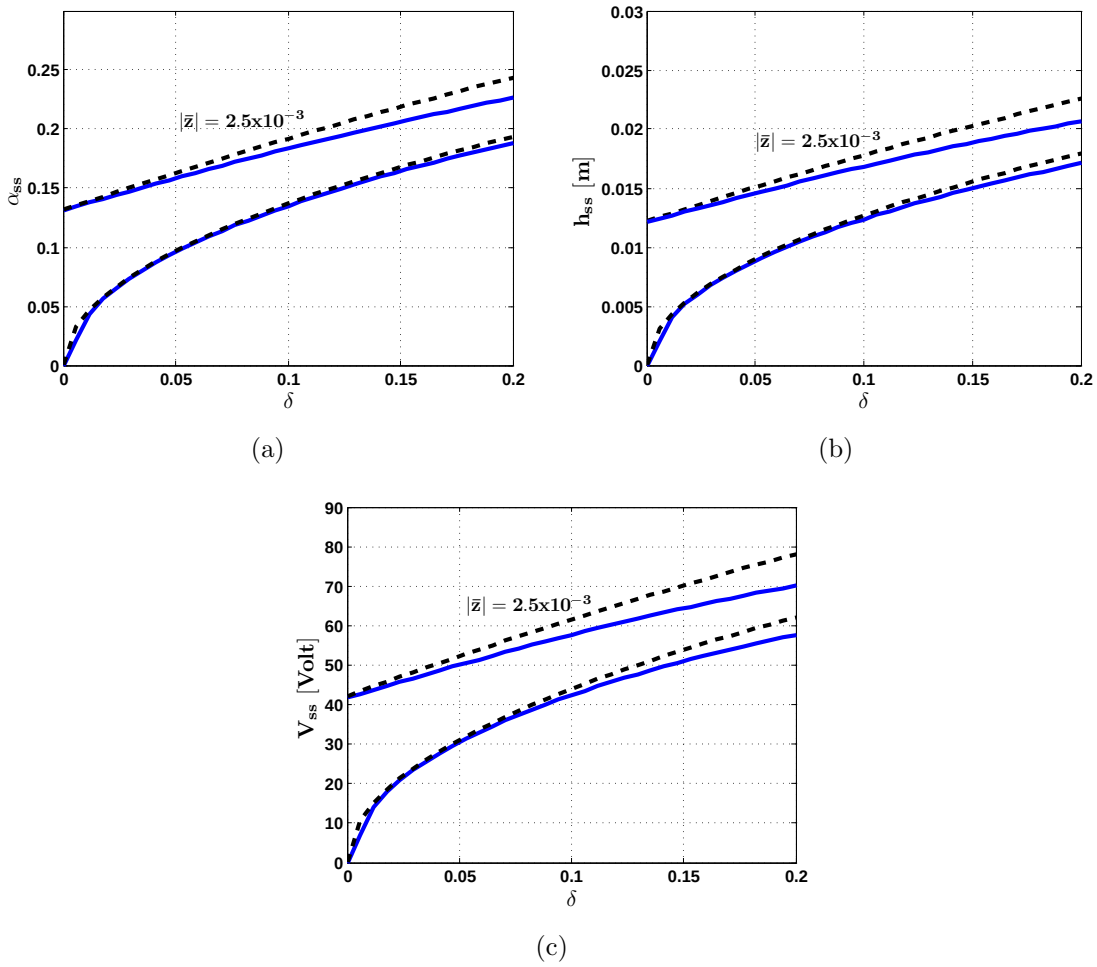

Figure 5.5: Comparison between the analytical prediction (dashed) and the numerical solution (solid): (a) pitch angle, (b) plunge deflection, and (c) output voltage.

manifold reduction and the method of normal forms are accurate for a small range of the bifurcation parameters. Hence, the accuracy is expected to deteriorate as δ and/or σ become arbitrarily large.

5.5 Response Behavior Below the Flutter Speed

When the velocity of the flow is below the flutter speed, i.e. $U < U_f$, the self-sustained oscillations cannot be excited and the harvester's response only contains the frequency of excitation, Ω. As such, the response is always periodic with a frequency matching the excitation frequency. Figure 5.6 depicts the voltage frequency-response behavior of the harvester for wind speeds that are below the flutter speed. For $U = 0$, the harvester exhibits a linear frequency response similar to that seen for a base-excited linear harvester. As the wind speed is increased, the amplitude of the steady-state voltage increases and the curves bend to the right due to the hardening nonlinearity in the plunge and pitch restoring forces which becomes prevalent as the amplitude of motion increases. Due to the bend in the frequency response curves, a region of multivalued solutions exists. In this region, three branches of solutions coexist, one branch of unstable and physically unrealizable saddles (stars), and two branches of stable solutions corresponding to the large and small amplitude branch of solutions. Initial conditions determine which of the solutions represents the actual motion.

Since the oscillation frequency of the harvester decreases with the wind speed as shown previously in Fig. 5.3 (b), the peak of the voltage-response curves shifts towards smaller frequencies as depicted in Fig. 5.6. The reduction in the frequency which is caused by a reduction in the effective stiffness and damping of the system due to the flow of air has the desired influence of increasing the steady-state voltage amplitude for the same value of input excitation. For instance, a 50% improvement in the output voltage can be attained when the harvester is placed in an air flow with a speed approximately half of the flutter speed, $U = 4.6\ m/s$. The amplification becomes even more prevalent as the speed is increased further toward $U = 8.6\ m/s$. Such result has a critical implication since it clearly indicates that the output voltage

of a base-excited harvester can be significantly improved if it is subjected to an air flow with a speed below the flutter speed.

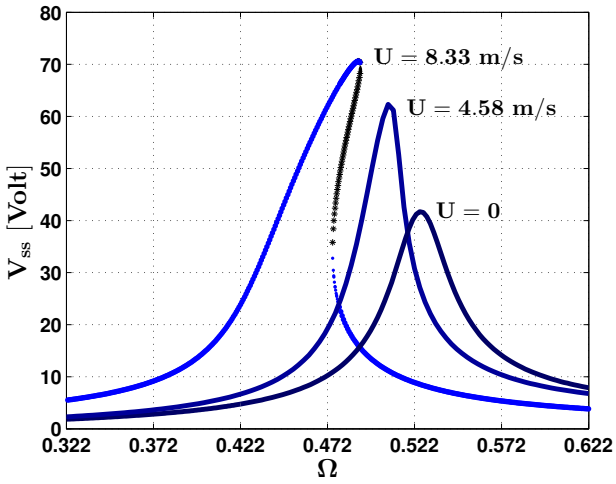

Figure 5.6: Variation of the steady-state output voltage amplitude with the excitation frequency for different wind speed, U, below the flutter speed. Results are obtained for $|\bar{z}| = 2.5 \times 10^{-3}$.

Variations of the root mean square (RMS) output power of the harvester with the amplitude of the base excitation for wind speeds below the flutter speed are shown in Fig. 5.7. Results are obtained for a resistive load of $75k\Omega$ and $\sigma = 0$, i.e., when the excitation frequency is equal to the frequency of the self-sustained oscillations at the given wind speed. Again, Fig. 5.7 clearly demonstrates that the air flow amplifies the influence of the base-excitation on the harvester. The amplification can be substantial for wind speeds just below flutter. Furthermore, the dependence of the power on the amplitude of the base excitation is quadratic in nature. This is similar to what is seen in vibration energy harvesters indicating that the base excitation governs the nature of the response with the air flow serving to amplify its amplitude by reducing the effective stiffness and damping.

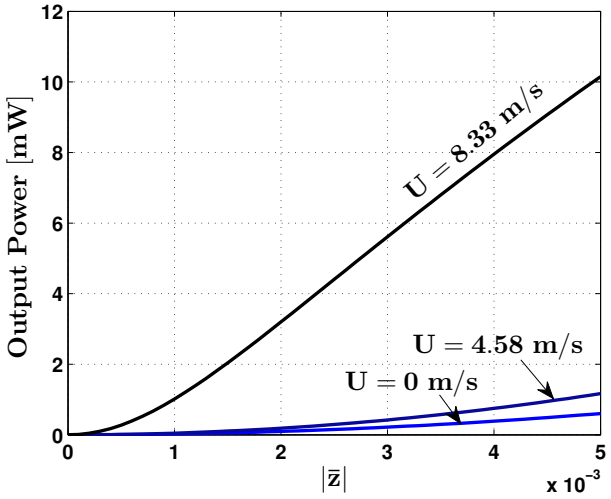

Figure 5.7: Variation of the RMS output power of the harvester with the excitation amplitude $|\bar{z}|$. Results are obtained for $\sigma = 0$, and $R = 75\ k\Omega$.

5.6 Response Behavior Above the Flutter Speed

5.6.1 Characteristics of the Output Voltage

In general, when the harvester is excited at its base and the wind speed is above the flutter speed, one would expect the response to contain the excitation frequency, Ω, and the limit-cycle oscillation frequency, ω_0. Consequently, as shown previously in Fig. 5.4, the voltage across this resistor can be periodic or quasiperiodic in time depending on the wind speed, the magnitude of the base excitation, and its frequency.

Towards investigating the influence of these parameters on the output voltage of the harvester, Equations (5.9) and (5.10) are used to generate the frequency-response curves of the harvester just beyond the flutter instability as shown in Fig. 5.8 (a). When Ω is close to ω_0 ($|\sigma|$ is small), the response is periodic and characterized by the frequency Ω (solid-line). In this case, the free-oscillation component of the response is entrained by the forced component, resulting in a synchronized periodic

output voltage. On the other hand, when Ω is far from ω_0 ($|\sigma|$ is large), a pair of complex conjugate eigenvalues associated with the Jacobian of the modulation equations transversally crosses the imaginary axis from the left- to the right-hand side. Consequently, the periodic response loses stability via a secondary Hopf bifurcation. This yields a two-period quasiperiodic output voltage indicated by the dashed-line.

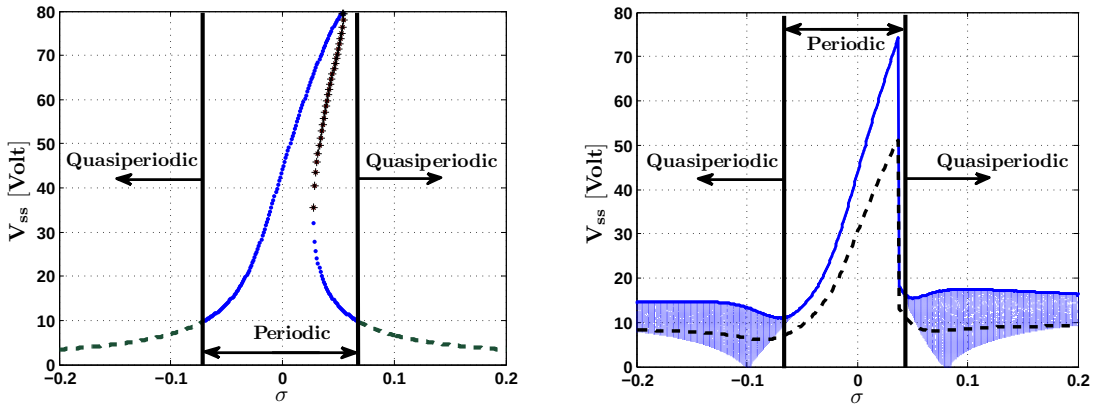

(a) (b)

Figure 5.8: Variation of the steady-state amplitude of the output voltage with the excitation frequency. (a) Analytical; solid line represents stable periodic solutions, stars represent unstable solutions, and dashed lines represent quasiperiodic solutions. (b) A numerical Poincarè map (frequency sweep up) with the dashed lines representing the RMS voltage. Results are obtained for $\delta = 0.01$ and $|\bar{z}| = 2.5 \times 10^{-3}$.

The analytical results are further confirmed in Fig. 5.8 (b) which depicts a stroboscopic Poincarè map obtained by long-time integration of the original equations of motion for the same set of parameters. Clearly, the analytical results are in good agreement with those obtained numerically. The transition from periodic to quasiperiodic responses at the critical frequencies, which are also know as the *lock-out* frequencies, is well predicted. Further, for the given wind speed and base excitation amplitude, it is demonstrated that the frequency bandwidth which produces a periodic output

voltage yields a significantly higher voltage level as compared to the quasiperiodic region.

5.6.2 Influence of the Base Excitation

Figure 5.9 investigates the effect of the amplitude of base excitation on the output voltage just beyond the flutter speed for $\delta = 0.01$. It is evident that, for small values of $|\bar{z}|$, a large bandwidth of quasiperiodic responses exists. The bandwidth decreases and diminishes as $|\bar{z}|$ increases and exceeds a threshold value. Furthermore, as the amplitude of the excitation increases, the steady-state output voltage of the harvester increases and the frequency-response curves bend further to the right. Consequently, the peak voltage is harnessed at a higher frequency.

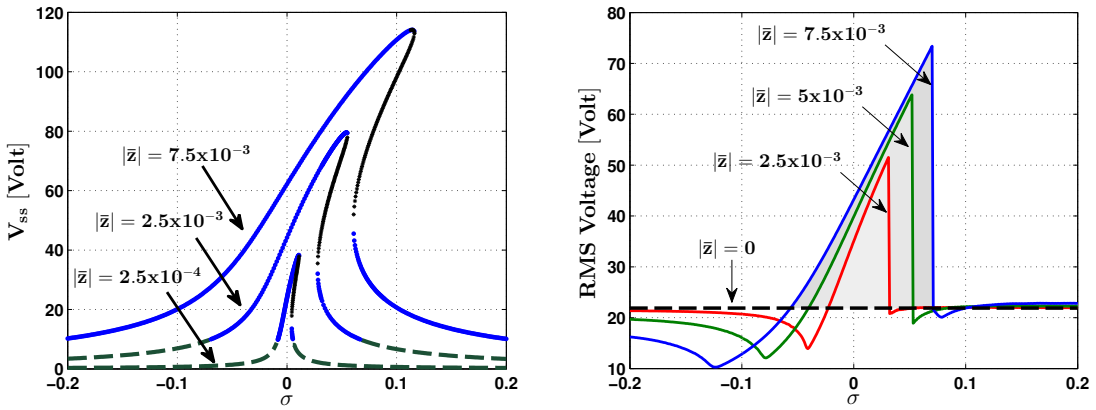

(a) (b)

Figure 5.9: Variation of the output voltage with the excitation frequency for different excitation amplitudes $|\bar{z}|$: (a) Steady-state voltage obtained analytically for $\delta = 0.01$. Solid lines represent stable periodic solutions and dashed lines represent unstable periodic solutions. (b) RMS voltage obtained numerically for $\delta = 0.05$.

Due to the quasiperiodicity of the response away from the resonant frequency, im-

provement in the output voltage with the magnitude of the input excitation as demonstrated in Fig. 5.9 (a) does not necessarily imply enhanced performance under the combined loading for all values of the excitation frequency. To better understand the effect of adding the base excitation on the overall performance, variation of the RMS voltage with the frequency is studied for $\delta = 0.05$ and different values of $|\bar{z}|$. Results are then compared to the RMS output voltage of the harvester when $|\bar{z}| = 0$ as shown in Fig. 5.9 (b). When $|\bar{z}| \neq 0$, there is a range of frequencies within which the external excitation is beneficial producing a positive voltage gain (shaded-area). This occurs when the RMS voltage due to the combined loading is higher than the 22 Volts resulting from the aerodynamic loading alone (dashed-lines). This frequency bandwidth always occurs within the periodic response range near the resonance peak and increases as the amplitude of the base excitation increases. Additionally, for excitation frequencies that are sufficiently lower than the resonant frequency, the RMS voltage is always less than the 22 Volts obtained using the aerodynamic loading. In such cases, the air flow serves to dissipate energy from the external excitation, thereby reducing the output voltage.

A stroboscopic Poincaré map of the steady-state output voltage of the harvester with the amplitude of base excitation and the corresponding RMS voltage are presented in Fig. 5.10 (a) and (b), respectively. The figures demonstrate that quasiperiodic responses only occur for small values of $|\bar{z}|$ due to the presence of two incommensurate frequencies in the voltage response. As $|\bar{z}|$ is increased beyond a certain threshold, a transition to periodic responses is always observed. At the transition point, both frequencies lock into each other and the increase in the energy provided by the external excitation eliminates (quenches) the quasiperiodic response. For higher wind speeds, the transition to quasiperiodic solutions is delayed to larger base excitations because

the base excitation has to supply higher energy to quench the response. As the excitation amplitude approaches the quenching boundary, the RMS voltage increases rapidly as shown in Fig. 5.10 (b). Consequently, higher wind speed require larger base excitations for enhanced performance.

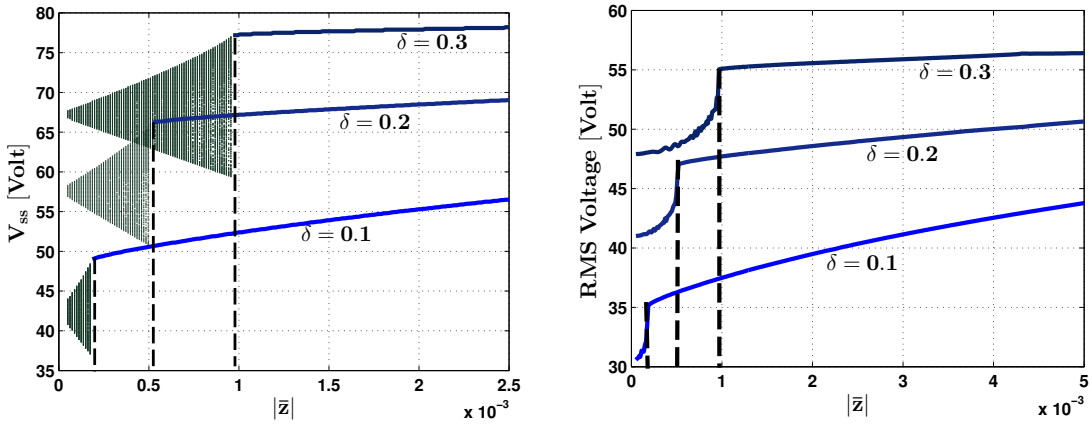

(a) (b)

Figure 5.10: Variation of the steady-state output voltage with the excitation amplitude. Results are obtained by numerical integration of the equations of motion for $\sigma = 0$ and different values of δ. (a) Poincaré map and (b) the corresponding RMS voltage. Vertical dashed-lines represent the quenching boundary.

Variation of the quenching boundary with the excitation frequency for different values of δ as calculated via the stability of Equations (5.9) and (5.10) is shown in Fig. 5.21. The regions filled with circles (red) represent amplitude-frequency combinations leading to quasiperiodic responses (generally lower output voltage) and the star-filled regions (blue) represent periodic responses (generally higher output voltage). Figure 5.21 also shows regions where the two responses overlap as a result of the bend in the frequency response curves. In such regions, initial conditions determine the actual performance of the harvester. The solid-line represents the locus of peaks at which the maximum output voltage can be attained.

For wind speeds below the flutter instability, $\delta \leq 0$, the response is always periodic and stable as shown in Fig. 5.21 (a). As expected, the peak voltage shifts towards larger frequencies as $|\bar{z}|$ increases due to the bend in the frequency response curves . When the wind speed crosses the flutter boundary, $\delta = 0.01$, two regions where quasiperiodic responses develop can be observed on either side of the $\sigma = 0$ axis. As $|\sigma|$ increases, Ω is away from ω_0, larger base excitations become necessary to quench the quasiperiodic responses.

When the wind speed is increased further to $\delta = 0.1$, a region where coexisting periodic and quasiperiodic responses coexist develops. In this region, the initial conditions determine whether the harvester will generate large RMS voltage (periodic response) or small RMS voltage (quasiperiodic response). The size of this region increases as δ is increased further to $\delta = 0.3$.

5.6.3 Influence of the Wind Speed

Another important factor influencing the response of the harvester is the wind speed. Figure 5.12 (a) depicts the voltage-frequency response curves for a base excitation of magnitude $|\bar{z}| = 2.5 \times 10^{-3}$ and different wind speeds. As the wind speed increases, the voltage-frequency response curves shift toward lower frequencies and higher output voltages are realized. As far as performance is concerned, the total RMS voltage of the harvester is compared to the RMS voltage due to flutter only (dashed lines) as demonstrated in Fig. 5.12 (b). It is evident that there exists a bandwidth of frequencies right around resonance in which the RMS voltage resulting from the combined loading exceeds that obtained via only the aerodynamic loading. However, for excitation frequencies that are below resonance, the RMS voltage drops significantly

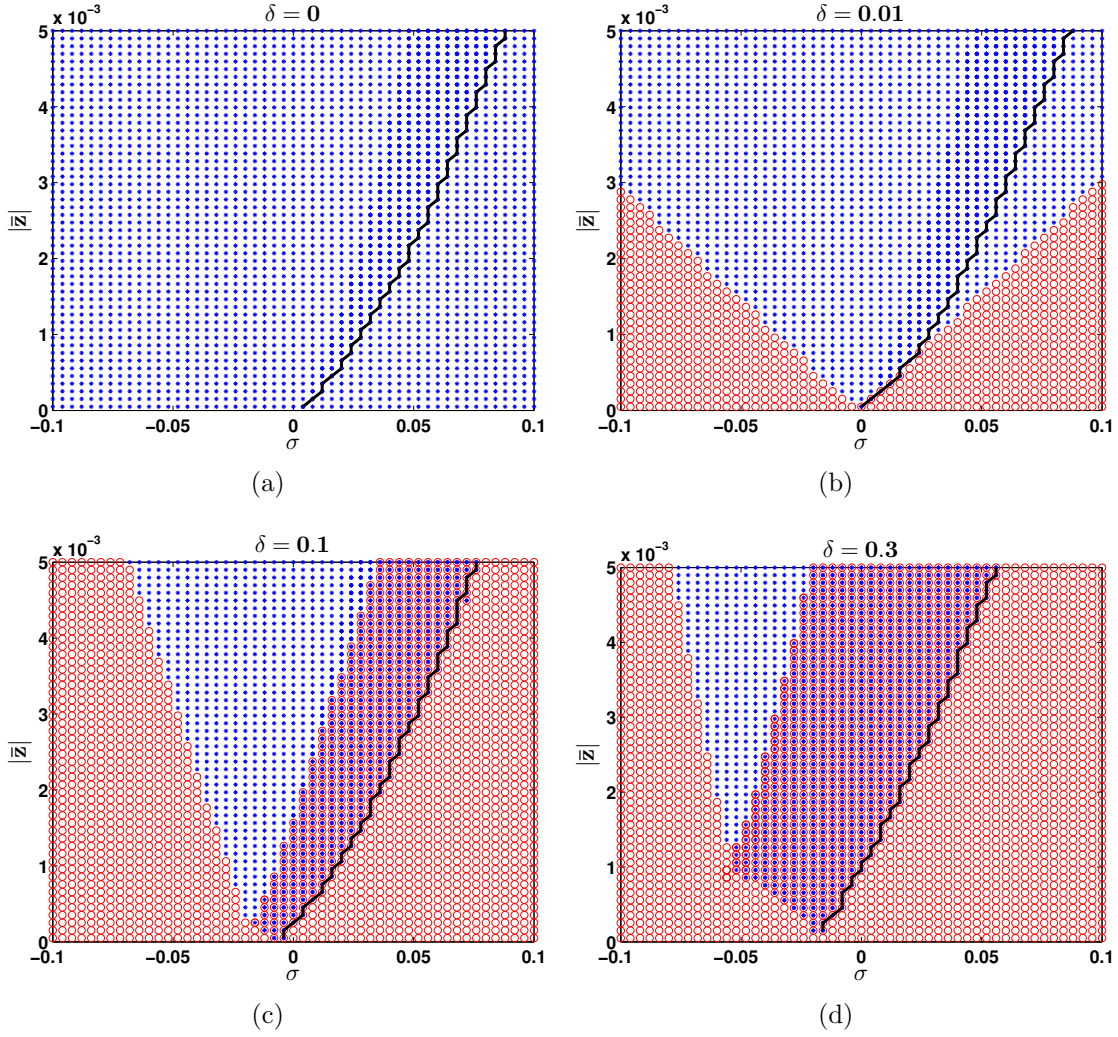

Figure 5.11: Quenching boundary as a function of the excitation frequency. Circles represent quasiperiodic solutions and stars represent periodic solutions. Results are obtained for (a) $\delta = 0$, (b) $\delta = 0.01$, (c) $\delta = 0.1$, and (d) $\delta = 0.3$.

below the values obtained from flutter. This clearly indicates that the nearness of the excitation frequency to the flutter frequency plays a significant role in characterizing the performance of the harvester under the combined loading.

Variation of the RMS output power of the harvester with the amplitude of the base excitation for different wind speeds is shown in Fig. 5.13. Results are obtained for

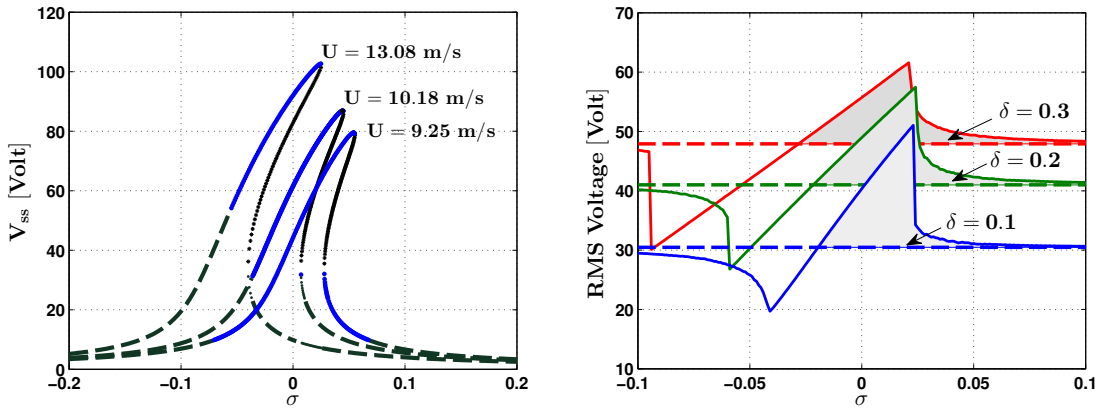

(a) (b)

Figure 5.12: Variation of the output voltage with the excitation frequency for $|\bar{z}| = 2.5 \times 10^{-3}$ and different wind speeds: (a) Steady-state voltage obtained analytically. Solid lines represent stable periodic solutions and dashed lines represent unstable periodic solutions. (b) RMS voltage obtained numerically. Dashed lines represent output voltage for $|\bar{z}| = 0$

.

a resistive load of $75k\Omega$ and $\sigma = 0$, i.e., when the excitation frequency is equal to the frequency of the self-sustained oscillations at the given wind speed. As the wind speed is increased beyond the flutter boundary, two distinct regions appear in the RMS power curves. In the first region, which occurs for small values of $|\bar{z}|$, a substantial variation of the power with the base excitation is observed. It is in this region where the response is quasiperiodic and the dynamics of the harvester depends significantly on the amplitude of excitation. In the second region, a transition from quasiperiodic oscillations to periodic oscillations occurs at the quenching boundary causing the RMS power to increase and become less dependent on the amplitude of excitation.

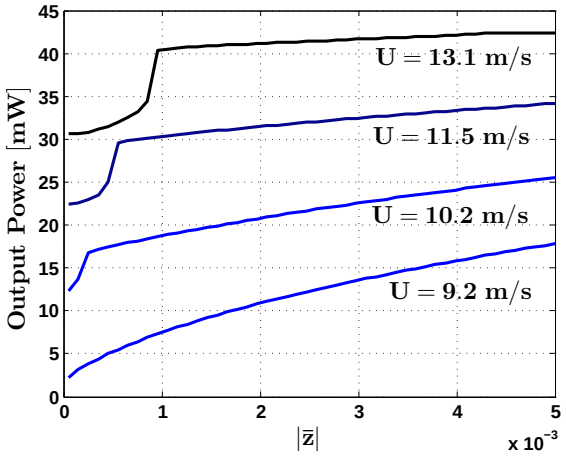

Figure 5.13: Variation of the RMS output power of the harvester with the excitation amplitude $|\bar{z}|$. Results are obtained for $\sigma = 0$, and $R = 75\ k\Omega$.

5.7 Optimal Load Resistance

In this section, we investigate the influence of the electric load on the output power. In the absence of external base excitations, and for wind speeds just beyond the flutter speed ($\delta = 0.01, 0.05$), the RMS output power increases and exhibits a peak for a certain load resistance as shown in Fig. 5.14 (a). Notably, the RMS output power drops sharply to zero just beyond the optimal load. This behavior can be understood by inspecting the influence of the load resistance on the flutter speed of the harvester as depicted in Fig. 5.14 (b). Since the energy dissipated in the load is equivalent to an electric damping, the wind speed necessary to initiate flutter increases near the optimal resistance. As a result, close to the optimal load, oscillations cease to exit for the lower wind speeds ($\delta = 0.01, 0.05$) and the power drops to zero. As the load resistance continues to increase away from the optimal load, the electric damping decreases and another peak appears. This behavior is clearly evident when $\delta = 0.05, 0.06$, and 0.075. For wind speeds sufficiently larger than the flutter instability,

e.g. $\delta = 0.125$, and 0.15, the power exhibits only one peak at a single optimal load.

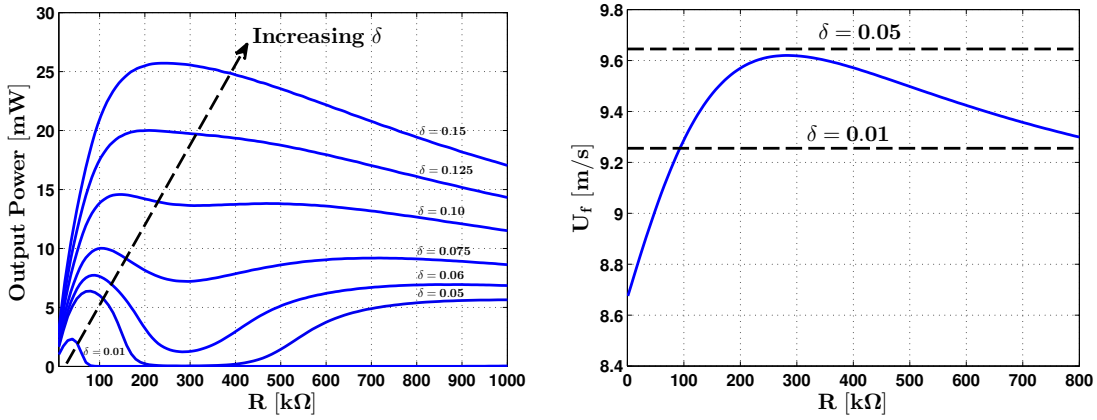

(a) (b)

Figure 5.14: (a) Variation of the RMS output power of the harvester with the electric load R. Results are obtained for increasing values of the wind speed, $\delta = 0.01$, 0.05 , 0.06, 0.075, 0.1, 0.125, 0.15, and $|\bar{z}| = 0$. (b) Variation of the flutter speed with the load resistance.

Figure 5.15 shows variation of the RMS output power with the electric load for a fixed base excitation amplitude, $|\bar{z}| = 2.5 \times 10^{-3}$, and different frequencies, σ. Results are obtained for $\delta = 0.01$. When $|\sigma|$ is small and the limit cycle oscillations due to flutter are entrained by the forced response, the RMS power exhibits a single peak as shown in Fig. 5.15 (a) and (b). Following the concept of impedance matching for linear systems, the peak power occurs at an electric load which is very close to the optimal load that maximizes the output power of a vibratory energy harvester when $U = 0$. On the other hand, due to the quasiperiodicity of the response, another peak appears near the optimal load of a flutter-based energy harvester when $|\sigma|$ is relatively large (dashed-lines). Increasing the excitation frequency away from resonance reduces the influence of the base excitation on the output power causing the amplitude of the second peak in the output power to drop as shown in Fig. 5.15 (d).

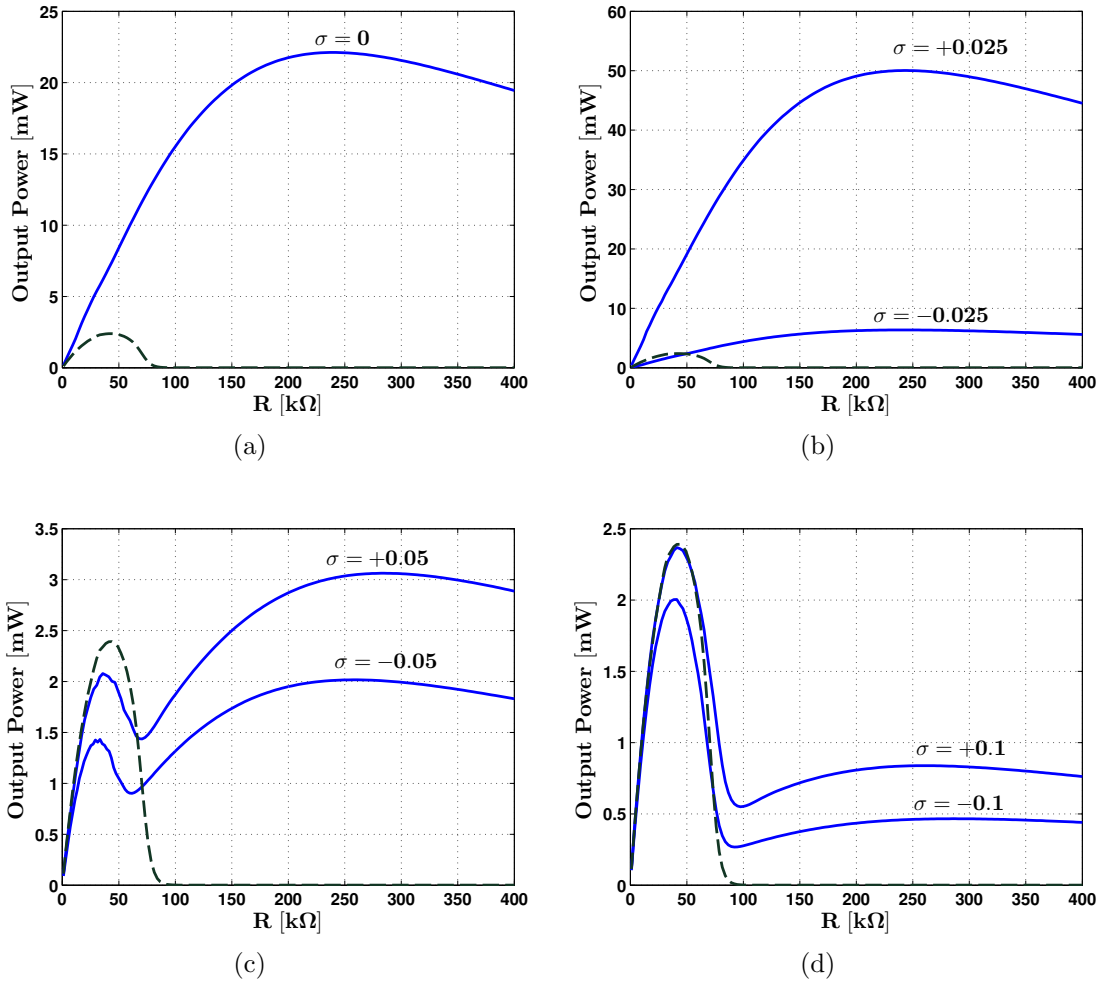

Figure 5.15: Variation of the RMS output power of the harvester with the electric load R. Results are obtained for $\delta = 0.01$, $|\bar{z}| = 2.5 \times 10^{-3}$ and different values of excitation frequency σ. (a) $\sigma = 0$, (b) $\sigma = \pm 0.025$, (c) $\sigma = \pm 0.05$, and (d) $\sigma = \pm 0.1$. Dashed lines represent output power for $|\bar{z}| = 0$.

5.8 Efficiency

The total energy conversion efficiency of the harvester under combined loading is shown in Fig. 5.16. The efficiency is calculated for the same design parameters given in Table. 5.2 with constant base acceleration of 0.5 m/s^2 and different excitation frequencies. The average input power given to the system through base excitation

and aerodynamic loading is estimated by $P_{in} = \frac{1}{T}\int_{t_0}^{t_0+T}(m_T\ddot{z}\dot{z} - L\dot{h} + M\dot{\alpha})dt$. The time-averaged power dissipated across the load R is given by $P_{out} = \frac{1}{T}\int_{t_0}^{t_0+T}\frac{V^2}{R}dt$. Here T is the period of the system. The efficiency of conversion from mechanical energy to electrical energy is then found by $\eta = \frac{P_{out}}{P_{in}}$. The figure clearly shows that, below the flutter speed 9.16 m/s, the efficiency is strongly dependent on the nearness of the excitation frequency to the resonant frequency and decreases as the wind speed increases. When flutter occurs, the efficiency becomes less dependent on the excitation frequency and the maximum efficiency is obtained right after the flutter speed.

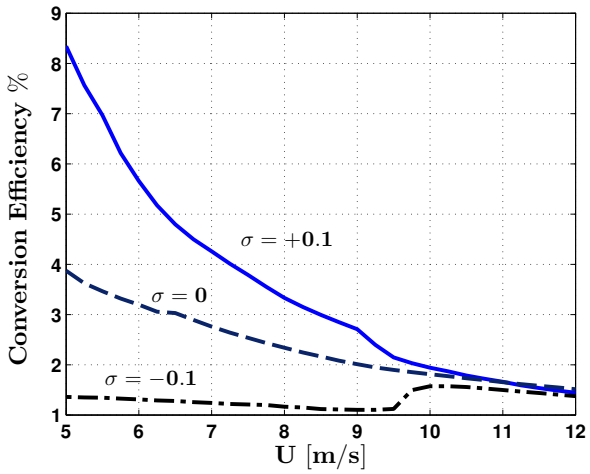

Figure 5.16: Variation of the conversion efficiency of the harvester with the wind speed. Results are obtained for a constant base acceleration 0.5 m/s^2 and different σ.

5.9 Experimental Validations

5.9.1 Experimental Setup

Figure 5.17 depicts the experimental setup used to investigate the response of the integrated vibratory and aeroelastic energy harvester (IVAEH) . The airfoil is con-

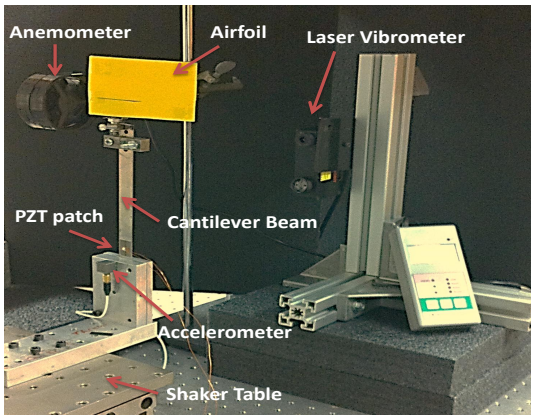

Figure 5.17: A view of the experimental setup.

structed out of lightweight wood and mounted on the tip of the beam with a torsional spring assembly that can be manually adjusted. A load resistance is connected across the electrodes of the piezoelectric laminate. The generator is attached to a seismic shaker which provides the harmonic base excitation, and the whole setup is placed in a wind tunnel to provide the aerodynamic loading. The control of the shaker and the collection of data are accomplished by use of a DS1103 controller board in conjunction with dSPACE. Acceleration at the base of the cantilever is measured using an accelerometer, and the velocity response of the cantilever is recorded using a laser vibrometer. The wind speed is measured by a conventional anemometer. Numerical parameters corresponding to the experimental setup are listed in Table 5.2.

5.9.2 Flutter Speed

In the absence of the base excitation, the IVAEH has two distinctive regions of operation defined by the flutter wind speed, U_f. When the flow velocity is below the flutter speed, the linear component of the lift produced by the flow over the airfoil cannot

Table 5.2: Geometric and material properties of the piezoelectric flutter energy harvester (experimental validations).

Physical properties			
$b[cm]$	4.2	ζ_α	0.12
$a[cm]$	-2.1	$K_h[N/m]$	26.6
$\chi_G[mm]$	3	ζ_h	0.005
$S[cm]$	5.2	C_L	2π
$m_W[g]$	31.4	c_3	6.5
$m_T[g]$	72.5	$C_p[\mu F]$	120
$I_\alpha[g.cm^2]$	97.2	$\theta[mN/V]$	0.11
$K_\alpha[mN.m/rad]$	1.9	$R[k\Omega]$	99.5

overcome the intrinsic damping present in the system. Hence, any initial disturbances decay in time and the harvester cannot maintain the steady-state oscillations necessary for energy harvesting. On the other hand, when the flow speed is above the flutter speed, the linear component of the lift overcomes the system's intrinsic damping and the harvester undergoes self-sustained periodic oscillations whose amplitude and frequency depends on the flow velocity. As shown in Fig. 5.18, it was observed that the harvester is capable of maintaining fixed amplitude periodic steady-state oscillations for any set of initial conditions as long as the wind speed is slightly above $U = 2.3\ m/s$, which corresponds to the flutter velocity, U_f. The point is also known as a super-critical Hopf bifurcation where a smooth transition from no oscillations to small amplitude steady-state oscillations is observed as the wind speed (bifurcation parameter) is slightly increased above U_f.

In the presence of the base excitation, the IVAEH is also expected to have a qualitatively different dynamic behavior within these two regions. Therefore, it is convenient

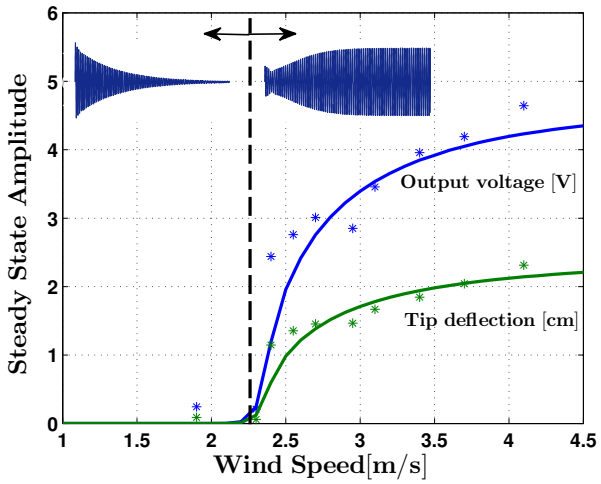

Figure 5.18: Variation of the steady-state amplitude of the output voltage and beam tip deflection with wind speed. Asterisks represent experimental data.

to divide the performance analysis into two distinctive regions based on the flutter speed.

5.9.3 Response Behavior Below the Flutter Speed

We first investigate the frequency response of the harvester below the flutter speed, $U < U_f$, for a fixed base acceleration of 0.1 m/s^2 as shown in Fig. 5.19. The response of the harvester is observed to be always periodic with the air flow serving to amplify the magnitude of the steady-state response. The power amplification is accompanied by a reduction in the resonant frequency due to a reduction in the effective stiffness as clearly evident by the shift of the peak frequency towards lower values. This reduction in stiffness amplifies the output power for the same level of input acceleration. Such results, which are also confirmed experimentally, indicate that the air flow over the airfoil improves the transduction capabilities of the harvester

in the presence of base excitations even when the flow velocity is much below the flutter speed. A 150% improvement in the RMS output power per unit acceleration is observed experimentally as the wind speed is increased from 0 to $2m/sec$. To put these numbers in a better perspective, we compare the results obtained using a single IVAEH to a scenario where two separate energy harvesters, one vibratory (VEH) and the other aeroelastic (AEH), are used to independently harvest energy from their respective excitation source. In other words, the VEH can only harvest energy from the available base excitation, while the AEH can only harvest energy from wind. In this case, and since the wind speed is below the flutter speed, $U < U_f$, the AEH cannot harvest any energy. On the other hand, the VEH which is not augmented with the airfoil can only produce the maximum power produced at zero wind speed. Thus, using two separate harvesters will reduce the RMS output power by 150% as compared to the IVAEH, not to mention the reduction in the power density due to using two separate harvesters instead of a single one.

5.9.4 Response Behavior Above the Flutter Speed

When the wind speed exceeds the flutter speed, $U > U_f$, the response of the IVAEH under the dual loading becomes much more complex due to the presence of two frequencies, namely, the base excitation frequency and the frequency of self-sustained oscillations. Consequently, the voltage across the electric load can be periodic or quasi-periodic in time. To demonstrate this fact, Equations (5.1a)-(5.1c) are used to generate a stroboscopic Poincarè map representing the voltage-response curve of the harvester just beyond the flutter instability for $U = 3\ m/s$ and a base acceleration of 0.15 m/s^2. In the stroboscopic map shown in Fig. 5.20 (a), the response under the combined loading is periodic with the same period as the excitation *only* when

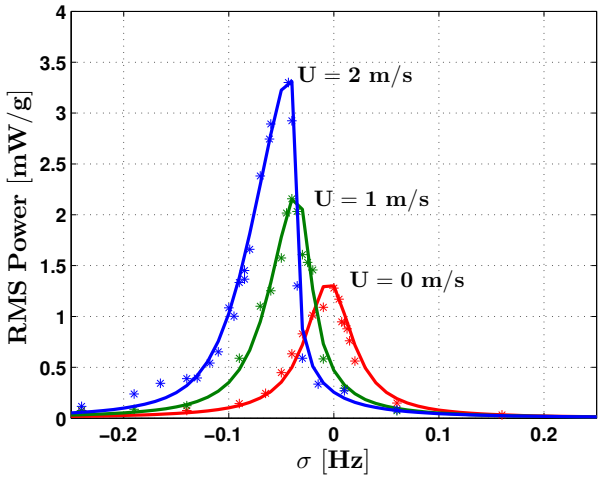

Figure 5.19: Variation of the RMS output power with the excitation frequency for different wind speeds below the flutter speed. Results are shown per unit g. Asterisks represent experimental data. Here, σ represents the shift between the excitation frequency and the first modal frequency of the system.

the map yields one point in the frequency response curve. This appears to be the case when the frequency of excitation is close to the frequency of the self-sustained oscillations, i.e. when $|\sigma|$ which represents the shift between the excitation frequency and the first modal frequency of the system is small. In this case, the self-sustained oscillation component of the response is entrained by the forced component, resulting in a synchronized periodic output voltage. On the other hand, when $|\sigma|$ becomes large, the voltage becomes two-period quasi-periodic with amplitude modulation as depicted in the time histories shown in Fig. 5.20 (a). This is due to the presence of two incommensurate frequencies in the response.

As far as performance is concerned, the total RMS voltage of the IVAEH (solid line) is compared to the RMS voltage due to flutter only (dashed lines). It is evident that there exists a bandwidth of frequencies right above resonance wherein the RMS

voltage resulting from the combined loading exceeds that obtained from the air flow only. However, for excitation frequencies that are slightly below resonance, the RMS voltage drops below the values obtained from the air flow. Away from resonance, the effect of the base excitation diminishes and the output voltage resulting from the combined loading approaches that resulting from the wind speed. These results are further confirmed experimentally in Fig. 5.20 (b) clearly indicating that the nearness of the excitation frequency to the flutter frequency is key for enhanced performance under the combined loading.

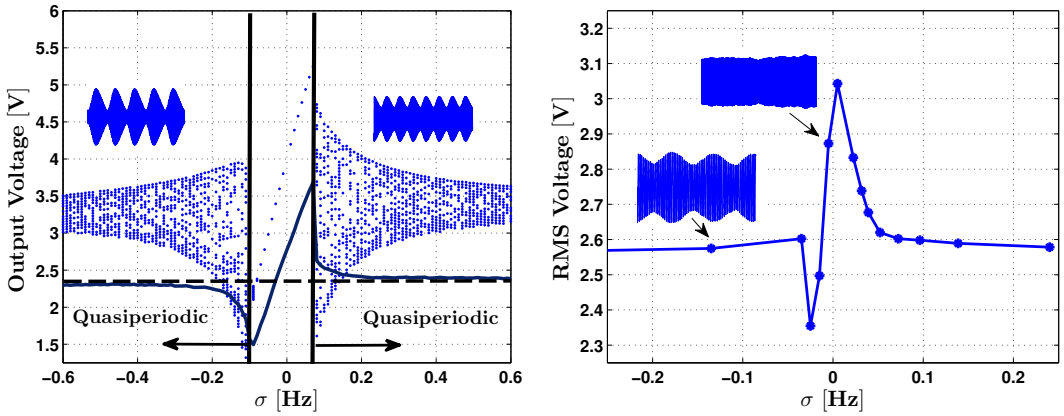

(a) (b)

Figure 5.20: Variation of the RMS output voltage with the excitation frequency: (a) Theoretical with the dashed line representing the RMS voltage when $z = 0$. (b) Experimental.

The magnitude of the base excitations also plays a critical role in improving the performance of the IVAEH by defining the bandwidth of frequencies where the desired periodic solutions exist. As the magnitude of the base excitation increases, the external excitation has more energy to quench the self-sustained oscillations resulting from the airflow causing the two frequencies to lock into each other. This broadens the bandwidth of frequencies where the desired periodic solutions exist. Figure 5.21 clearly illustrates this fact by showing that the bandwidth of frequencies where the

periodic solutions exist becomes wider as the magnitude of the base excitation increases.

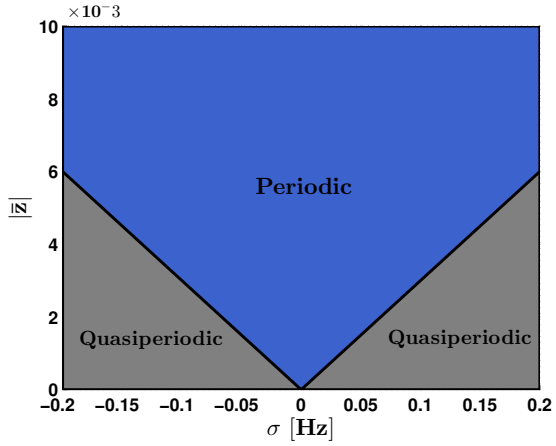

Figure 5.21: Quenching boundary as a function of the excitation frequency. Here, $|\bar{z}| = |z|/b$.

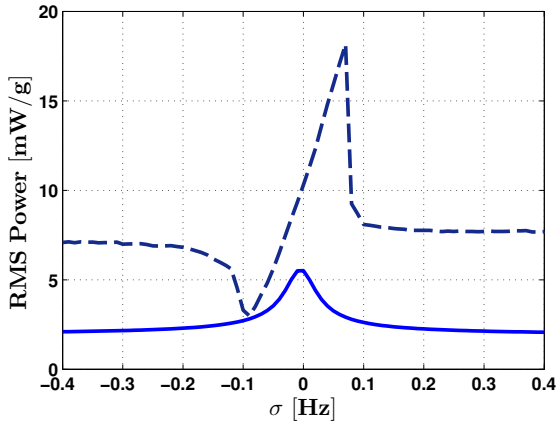

Figure 5.22: Variation of the RMS output power with the excitation frequency for two harvesting units. (Dashed): two IVAEHs, and (solid): combined power resulting from one AEH and one VEH.

For the purpose of performance comparison, the total RMS output power harvested using two IVAEHs is compared to that harvested using two separate energy harvesters, one VEH and the other AEH. Figure 5.22 clearly demonstrates the superiority of using a IVAEH to harvest energy from the combined loading with improvements in the RMS

output power reaching as much as three times that obtained from the AEH and VEH together.

Chapter 6

Conclusions

This Chapter presents the concluding remarks for this Dissertation and a summary of potential future research.

In general the research in this Dissertation focused on investigating the potential of concurrent energy harvesting from combination of vibratory base excitations and aerodynamic loading. As a platform to achieve the Dissertation objectives, two categories of aeroelastic energy harvesters were considered. The first category investigates galloping-based harvesters in which a bluff body, which is only allowed to plunge or translate vertically, is attached to the free end of a cantilever beam representing a one (mechanical) degree-of-freedom instability. The second category studies flutter-based harvesters. The harvesting beam in this case is attached to an airfoil section which is allowed to pitch about an elastic axis and to plunge representing two degree-of-freedoms instability. The following sections summarize the different tasks and conclusions drawn from each case.

6.1 Galloping-based Harvesters

An experimentally-validated model of a piezoelectric energy harvester under a combination of galloping and base excitations was developed. A nonlinear electromechanical distributed-parameter model of the harvester was first derived using the energy approach and by adopting the nonlinear Euler-Bernoulli beam theory, linear piezoelectricity, and the quasi-steady assumption for the aerodynamic loading. The partial differential equations were then discretized and a reduced-order model was obtained using a Galerkin expansion. The model was validated by conducting a series of experiments in which the harvester was attached to an electrodynamic shaker to provide the base excitations. The whole set up was then placed in a wind tunnel such that the bluff body is facing the air flow. In the experiments, the loading conditions in terms of the wind speed, base excitation amplitude, and excitation frequency were varied to study the harvester's response under the combined loading below and above the galloping speed. Results demonstrating the overall agreement between the predicted and experimental response were presented for both cases. It was shown that, when the wind speed is below the galloping speed, the response is always periodic containing only the frequency of excitation and a substantial amplification in the harvester's response was observed due to a reduction in the effective damping of the system. On the other hand, when the wind speed is above the galloping speed, the harvester's response can be periodic or quasi-periodic in time due to the presence of two frequencies in the response and the overall performance can be analyzed based on the nearness of the two frequencies.

A generalized formulation, analysis, and optimization was then presented. A nonlinear analysis based on perturbation theory was carried out to obtain an approximate analytical solution of the reduced-order model. A dimensional analysis was performed

to identify the important parameters that affect the system's response. The analysis was divided into two parts; the first for a harvester subjected to galloping excitations only. It was shown that, for a given shape of the bluff body and under quasi-steady flow conditions, the harvester's dimensionless response can be described by a single universal curve irrespective of the geometric, mechanical, and electrical design parameters. In the second part, a harvester under concurrent galloping and base excitations was analyzed. The total output power was shown to be dependent on three dimensionless loading parameters, namely, wind speed, base excitation amplitude, and excitation frequency. The response curves of the harvester were generated in terms of the loading parameters serving as a complete design guide for scaling and optimizing the performance of galloping-based harvesters under combined loading.

6.2 Flutter-based Harvesters

A lumped-parameter five-dimensional model representing the dynamics of the plunge and pitch motions of a piezoelectric energy harvester under the combined loading was considered. The elastic restoring forces in the plunge and pitch direction are assumed to be nonlinear and are represented by hardening flexural and torsional springs, respectively. A nonlinear quasi-steady approximation of the aerodynamic lift and moment was utilized and a harmonic external excitations was applied at the base. To study the response characteristics of the harvester near the flutter speed, center manifold reduction was used to reduce the original five-dimensional system into an equivalent first-order nonlinear ordinary differential equation. Subsequently, the method of normal forms was applied to obtain an approximate analytical solution of the resulting equation when the frequency of excitation is close to the frequency

of the self-sustained limit-cycle oscillations. Steady-state approximate analytical expressions for the pitch angle, plunge deflection, and output voltage were derived and validated against a numerical integration of the original equations of motion. The resulting expressions were then used to investigate how the base excitation influences the steady-state response of the harvester. It was observed that below the flutter speed, the response of the harvester is always periodic with the air flow serving to amplify the influence of the base excitation on the response by reducing the effective stiffness and damping of the system, and hence, increasing the RMS output power. Beyond the flutter speed, two distinct regions were observed. The first occurs when the base excitation is small and/or when the excitation frequency is far from the frequency of the self-sustained oscillations induced by the flutter instability. In this case, the response of the harvester is two-period quasiperiodic with amplitude modulation due to the presence of two incommensurate frequencies in the response. This amplitude modulation reduces the RMS output power. The second region occurs when the amplitude of excitation is large enough to quench the quasiperiodic response by causing the two frequencies to lock into each other. In this region, the response becomes periodic and the output power increases exhibiting little dependence on the amplitude of base excitation. The performance of the piezoelectric was then studied experimentally below and above the flutter speed and found to exhibit qualitative agreement with the theory. In terms of its transduction capabilities and power density, the integrated device was shown to have a superior performance under the combined loading when compared to utilizing two separate devices to harvest energy independently from the two available energy sources. Even below its flutter speed, the proposed device was able to provide 1.5 times the power obtained using two separate harvesters.

6.3 Directions for Future Research

Although galloping-based and flutter-based harvesters exhibit the same qualitative performance enhancement characteristics under combined loading, from a design perspective, the multiplicity of variables in a two-degree-of-freedom flutter harvester makes progress in understanding and analysis of the problem very difficult. Unlike galloping, there are several parameters in addition to the aerodynamic loading coefficients that have to be carefully chosen. For instance, a weak coupling between the pitch and plunge modes shifts the flutter speed into higher wind speeds. At the same time, increasing this coupling by increasing the mass of the airfoil can lead to a static divergence instability rather than flutter oscillations [69]. Hence, investigating the relative performance of energy harvesters with different aeroelastic excitation mechanisms represents an interesting topic for future work. For instance, a relative performance study can be conducted to determine whether the two degrees-of-freedom flutter harvester can outperform the single degree-of-freedom galloping harvester. This can be achieved by comparing the root mean square output power of both harvesters for the same loading conditions. For a fair comparison, the same piezoelectric beam should be used. The tip body, i.e square-sectioned bluff for galloping harvester and an airfoil for flutter harvester, should be designed to have the same mass, span, and operational volume. The elastic axis or the coupling between the pitch and plunge modes can also be designed such that the wind speed of flutter instability and galloping instability are the same. The analysis can be extended to include the influence of base excitations. Results of this study can be utilized as a basis to develop performance metrics and provide conclusions about which harvester is favorable for the given loading conditions.

Investigating the role of nonlinearities in the transduction of aeroelastic energy har-

vesters forms another avenue for future research. Different nonlinear configurations such as softening, hardening, and bi-stability can be introduced to the harvester by exploiting nonlinear magnetic interactions. As numerical simulations might not be sufficient to understand the influence of system parameters, analytical approximations that predict the response behavior of harvesters with mono- and bi-stable potentials need to be obtained. These approximations can then by utilized to provide a new insight into the dynamics favorable for energy harvesting.

Appendices

Appendix A State-Space Formulation

The equations governing the dynamics of the harvester, Equation (5.1a)-(5.1c), can be transformed into state space by introducing the state vector

$$X = [x_1, x_2, x_3, x_4, x_5]^T \equiv [\alpha, \alpha', \bar{h}, \bar{h}', \bar{V}]^T.$$

This yields the following five dimensional system:

$$\begin{aligned}
x_1' &= x_2, \\
x_2' &= \left[a_{21} - a_{22}\left(\frac{U}{U_f}\right)^2\right]x_1 + \left[a_{23} - \left(\frac{1}{2} - \bar{a}\right)a_{22}\left(\frac{U}{U_f}\right)\right]x_2 \\
&\quad -a_{24}x_3 - \left[a_{25} + a_{22}\left(\frac{U}{U_f}\right)\right]x_4 + \chi_\alpha a_{26}x_5 + f_2(X;\bar{z}), \\
x_3' &= x_4, \\
x_4' &= \left[a_{41}\left(\frac{U}{U_f}\right)^2 - \chi_\alpha a_{21}\right]x_1 + \left[\left(\frac{1}{2} - \bar{a}\right)a_{41}\left(\frac{U}{U_f}\right) - \chi_\alpha a_{23}\right]x_2 \\
&\quad +a_{42}x_3 + \left[a_{43} + a_{41}\left(\frac{U}{U_f}\right)\right]x_4 - r_\alpha^2 a_{26}x_5 + f_4(X;\bar{z}), \\
x_5' &= -x_4 - e_R x_5 + \bar{z}'.
\end{aligned} \tag{A.1}$$

where the nonlinear functions of the state variables and base displacement are expressed as

$$\begin{aligned}
f_2(X;\bar{z}) &= a_{21}f_\alpha x_1^3 + a_{24}\bar{z} + a_{25}\bar{z}' - a_{24}f_h(x_3 - \bar{z})^3 + a_{22}\Psi, \\
f_4(X;\bar{z}) &= -\chi_\alpha a_{21}f_\alpha x_1^3 - a_{42}\bar{z} - a_{43}\bar{z}' + a_{42}f_h(x_3 - \bar{z})^3 - a_{41}\Psi.
\end{aligned}$$

and

$$\Psi = c_3\left(\frac{U}{U_f}\right)^2\left[x_1 + \frac{x_4}{U/U_f} + \frac{(1/2 - \bar{a})}{U/U_f}x_2\right]^3.$$

The constants a_{ij} appearing in Equation (A.1) are given by

$$a_{21} = \frac{r_\alpha^2}{\mathcal{D}}\left(\frac{\bar{\omega}}{\bar{u}_f}\right)^2,\ a_{22} = \frac{c_{L\alpha}}{\mathcal{D}}\left(\frac{1}{2} + \bar{a} + \chi_\alpha\right),\ a_{23} = 2\zeta_\alpha \frac{r_\alpha^2}{\mathcal{D}},$$
$$a_{24} = \frac{\chi_\alpha}{\bar{u}_f^2 \mathcal{D}},\ a_{25} = 2\zeta_h \frac{\chi_\alpha}{\mathcal{D}},\ a_{26} = \frac{e_\theta}{\mathcal{D}}, \quad a_{41} = \frac{c_{L\alpha}}{\mathcal{D}}\left(r_\alpha^2 + \chi_\alpha\left(\frac{1}{2} + \bar{a}\right)\right),$$
$$a_{42} = \frac{r_\alpha^2}{\bar{u}_f^2 \mathcal{D}}, \quad a_{43} = 2\zeta_h \frac{r_\alpha^2}{\mathcal{D}}, \quad \mathcal{D} = \left(\chi_\alpha^2 - r_\alpha^2\right).$$

Appendix B Center Manifold Reduction

According to the center-manifold theorem, analysis of the dynamics of an n-dimensional continuous system near one of its fixed points can be reduced to the analysis of the dynamics on its center manifold. At the flutter speed, $\delta = 0$, the origin, $X_0 = 0$, becomes a nonhyperbolic fixed point. Hence, there exists a local center manifold for the nonlinear system of Equation (5.7) near X_0. Moreover, since none of the eigenvalues of this fixed point lies in the right-half of the complex plane, the long-time dynamics of the system can be described by the dynamics on the center manifold, thereby reducing the dimensionality of the system.

Since the base excitation is harmonic of the form $\bar{z}(\tau) = |\bar{z}|\cos(\Omega\tau)$, Equation (5.7) represents a non-autonomous system of equations. To facilitate the implementation of the center manifold reduction, we transform Equation (5.7) into an autonomous form by introducing an additional state variable into the vector Y, such that

$$y_6 = |\bar{z}|e^{j\Omega\tau},\ \text{and} \qquad y_7 = |\bar{z}|e^{-j\Omega\tau}. \tag{B.1}$$

where the tilde denotes the complex conjugate. With that, we can write $y_6' = j\Omega y_6$, and $y_7' = -j\Omega y_7$ Using Equation (B.1), the five-dimensional nonautonomous system

of Equation (5.7) is transformed into a seven-dimensional autonomous system.

Since the influence of the base excitation on the harvester's response is mostly pronounced when the excitation frequency, Ω is close to the limit-cycle frequency ω_0, we limit the analysis to such scenarios and describe the nearness of Ω to ω_0 by introducing the detuning parameter, σ, such that

$$\Omega = (1 + \sigma)\omega_0. \tag{B.2}$$

To capture the dependence of the center manifold dynamics on δ and σ, we make use of the suspension trick [70]; that is, we augment Equation (5.7) with the additional equations

$$\delta' = 0, \text{ and } \qquad \sigma' = 0. \tag{B.3}$$

Next, we construct the center manifold in the neighborhood of the fixed point. To this end, we separate the center and the stable subspaces by dividing the vector Y into a center subspace (non-decaying dynamics), $Y_c = [y_1, y_2, y_6, y_7, \delta, \sigma]^T$, and a stable subspace (decaying dynamics) $Y_s = [y_3, y_4, y_5]^T$. This yields

$$Y_c' = J_c Y_c + F_c(Y_c, Y_s), \tag{B.4}$$

$$Y_s' = J_s Y_s + F_s(Y_c, Y_s), \tag{B.5}$$

where J_c and J_s are coefficient matrices associated with the center and stable dynamics, respectively; and F_c and F_s are nonlinear functions of Y_c and Y_s.

Since the stable subspace is three-dimensional, we seek a three-dimensional center manifold emanating from the origin in the form $Y_s = \mathbf{CM}(Y_c)$, where $\mathbf{CM} = (CM_1, CM_2, CM_3)^T$. The goal here is to describe the decaying dynamics of Y_s

in terms the center dynamics, Y_c. Noting that the center manifold is invariant, $Y_s(\tau) = \mathbf{CM}(Y_c(\tau))$, we can write

$$Y_s' = \frac{\partial Y_s}{\partial \tau} = \frac{\partial \mathbf{CM}}{\partial Y_c}\frac{\partial Y_c}{\partial \tau} = \frac{\partial \mathbf{CM}}{\partial Y_c}Y_c'. \tag{B.6}$$

Substituting Equation (B.4) and (B.5) into Equation (B.6), we obtain the center manifold dynamics as

$$\frac{\partial}{\partial Y_c}\mathbf{CM}(Y_c)\big[J_cY_c + F_c(Y_c, \mathbf{CM}(Y_c)\big] - \big[J_s\mathbf{CM}(Y_c) + F_s(Y_c, \mathbf{CM}(Y_c)\big] = 0. \tag{B.7}$$

The boundary conditions are obtained from the fact that the center manifold is tangent to the center eigenspace at the origin, that is

$$\mathbf{CM}(0) = 0, \text{ and } \qquad \frac{\partial}{\partial Y_c}\mathbf{CM}(0) = 0. \tag{B.8}$$

To solve Equation (B.7) with boundary conditions (B.8) , we approximate the components of $\mathbf{CM}(Y_c)$ with polynomials. The polynomial approximations are taken to be cubic since the nonlinear terms in Equation (5.7) start first at a third order. Additionally, the polynomials do not contain constant or linear terms, such that the conditions of Equation (B.8) are satisfied. Assuming that σ and δ are of order y_i^2, the assumed polynomial approximation CM_i will have twenty eight unknown coefficient multiplying a cubic-order combination of the center state variables, i.e., $[y_1^3, y_2^3, y_6^3, y_1^2y_6, \sigma y_1, \delta y_6, \ldots]$. This yields a total of eighty four unknown coefficients for the three-dimensional center manifold. These coefficients can be obtained by substituting the assumed polynomial approximation for CM_i into Equation (B.6) and equating the coefficients associated with the basis of the polynomial approximation to zero.

Once the coefficients are obtained, the stable dynamics becomes a known cubic polynomial expansion of the center states. Specifically, y_3, y_4 and y_5 can now be described as a polynomial function of $y_1, y_2, y_6, y_7, \sigma$, and δ. Substituting these expressions back into Equation (B.4), we obtain the following first order nonlinear differential equation which accurately describes the y_1 dynamics on the center manifold:

$$y_1' = j\omega_0 y_1 + \kappa_1 y_6 + \kappa_2 y_7 + F_c(\delta, \sigma, y_1, y_2, y_6, y_7), \tag{B.9}$$

where F_c is a nonlinear function that involves all the cubic combinations of its variables $(\delta, \sigma, y_1, y_2, y_6, y_7)$ multiplied by known coefficients keeping in mind that δ and σ are assumed to be of quadratic order.

The solution of the original five-dimensional system, Equation (5.7), near the origin and the bifurcation value can now be studied by analyzing the one-dimensional system of Equation (B.9).

Appendix C Normal Form Analysis

The method of normal forms can now be implemented to find a coordinate system in which Equation (B.9) takes the simplest form [68]. This coordinate transformation is found by solving a sequence of linear problems. To keep track of the different orders of magnitude, we use a non-dimensional parameter ϵ as a bookkeeping device and scale the nonlinearity, such that

$$y_1' = j\omega_0 y_1 + \epsilon\big[\kappa_1 y_6 + \kappa_2 y_7 + F_c(\delta, \sigma, y_1, y_2, y_6, y_7)\ \big]. \tag{C.1}$$

To obtain the normal form, we introduce the coordinate transformation (near identity transformation) [68]

$$y_1 = \eta + \epsilon h_1(\delta, \sigma, \eta, y_2, y_6, y_7) + ... \tag{C.2}$$

Substituting Equation (C.2) into Equation (C.1), using $y_6' = j\Omega y_6$, and $y_7' = -j\Omega y_7$, and equating the coefficients of ϵ on both sides, we obtain the following homology equations for h_1

$O(\epsilon^0)$:

$$\eta' = j\omega_0 \eta, \tag{C.3}$$

$O(\epsilon^1)$:

$$j\omega_0\left(\frac{\partial h_1}{\partial \eta}\eta - \frac{\partial h_1}{\partial y_2}y_2\right) + j\Omega\left(\frac{\partial h_1}{\partial y_6}y_6 - \frac{\partial h_1}{\partial y_7}y_7\right) = j\omega_0 h_1(\delta, \sigma, \eta, y_2, y_6, y_7) + \kappa_1 y_6 + \kappa_2 y_7 + F_c(\delta, \sigma, \eta, y_2, y_6, y_7). \tag{C.4}$$

Next, we choose h_1 to eliminate as many terms as possible from Equation (C.4). It turns out that h_1 can be chosen to eliminate all nonresonant terms from Equation (C.4). The resonant and near-resonant terms remain yielding the following equation for y_1.

$$y_1' = j\omega_0 y_1 + \tfrac{1}{2}(\alpha_3 + \sigma\alpha_4)y_6 + \delta\alpha_1 y_1 + \big(4\alpha_2 y_1^2 y_2 + (\alpha_7 - \alpha_9)y_1^2 y_7 + \alpha_8 y_2 y_6^2 + \tfrac{1}{2}\alpha_6 y_6^2 y_7 + (\alpha_7 + \alpha_9)y_1 y_2 y_6 + \alpha_5 y_1 y_6 y_7\big). \tag{C.5}$$

Equation (C.5) represents the simplest form of Equation (B.9) and can be used to study the dynamics of the harvester near the flutter instability under the condition that the frequency of external excitation is close to the frequency of the limit cycle.

Bibliography

[1] A.J. duPlessis, M.J. Huigsloot, and F.D. Discenzo. Resonant Packaged Piezoelectric Power Harvester for Machinery Health Monitoring. In *Proceedings of Smart Structures and Materials Conference, SPIE*, page 5762, San Diego, CA, 2005.

[2] D. J. Inman and B. L. Grisso. Towards Autonomous Sensing. In *Smart Structures and Materials*, pages 61740T–61740T. International Society for Optics and Photonics, 2006.

[3] R. S. Sanders and M. T. Lee. Implantable Pacemakers. *Proceedings of the IEEE*, 84(3), 1995.

[4] I. D. Capel, H. M. Dorrell, E. P. Spencer, and M. W. Davis. The Amelioration of the Suffering Associated with Spinal Cord Injury with Subperception Transcranial Electrical Stimulation. *Spinal Cord*, 41:109–117, 2003.

[5] G. Renzenbrink and M. J Jzerman. Percutaneous Neuromuscular Electrical Stimulation for Treating Shoulder Pain in Chronic Hemiplegia. Effects on Shoulder Pain and Quality of Life. *Clinical Rehabilitation*, 18:359–365, 2004.

[6] S. Roundy, P.K. Wright, and J. Rabaey. A Study of Low Level Vibrations as a Power Source for Wireless Sensor Nodes. *Computer Communications*, 26:1131–1144, 2003.

[7] S. Roundy and P.K. Wright. A Piezoelectric Vibration-Based Generator for Wireless Electronics. *Journal of Intelligent Materials and Structures*, 16:809–823, 2005.

[8] S. W. Arms, C. P. Townsend, D. L. Churchill, G. H. Galbreath, and S. W. Mundell. Power Management for Energy Harvesting Wireless Sensors. In *Proceedings of the Smart Structures and Materials Conference, SPIE*, pages 5763 267–75, San Diego, CA, 2005.

[9] S. P. Gurav, A. Kasyap, M. Sheplak, L. Cattafesta, R. T. Haftka, J. F. L. Goosen, and F. Van Keulen. Uncertainty-based Design Optimization of a Micro Piezoelectric Composite Energy Reclamation Device. In *Proceedings of the 10th AIAA/ISSSMO Multidisciplinary Analysis and Optimization Conference*, pages 3559–70, 2004.

[10] W. Zhou, W. H. Liao, and W. J. Li. Analysis and Design of a Self-powered Piezoelectric Microaccelerometer. In *Proceedings of the Smart Structures and Materials Conference, SPIE*, pages 5763 233–240, San Diego, CA, 2005.

[11] S. Gregori, Y. Li, H. Li, J. Liu, and F. Maloberti. 2.45 GHz Power and Data Transmission for a Low-Power Autonomous Sensors Platform. *ISLPED 04*, pages 269–273, 2004.

[12] J. W. Kim, H. Takao, K. Sawada, and M. Ishida. Integrated Inductors for RF Transmitters in CMOS/MEMS Smart Microsensor Systems. *Sensors*, 7:1387–1398, 2007.

[13] W. Bracke, P. Merken, R. Puers, and C. Van Hoof. Generic Architectures and Design Methods for Autonomous Sensors. *Sensors and Actuators A*, 135:881–888, 2007.

[14] K. Baerta, B. Gyselinckxa, T. Torfsa, V. Leonova, F. Yazicioglua, S. Brebelsa, S. Donnaya, J. Vanfleterena, E. Beyna, and C. Van Hoof. Technologies for Highly Miniaturized Autonomous Sensor Newtorks. *Microelectronics Journal*, 37:1563–1568, 2006.

[15] J. A. Paradiso and Starner T. Energy Scavenging for Mobile and Wireless Electronics. *IEEE Pervasive Computing*, 4:18–27, 2005.

[16] O. Soykan. Power Sources for Implantable Medical Devices. London, UK, 2002.

[17] H. Sodano, D.J. Inman, and G. Park. A Review of Power Harvesting from Vibration Using Piezoelectric Materials. *The Shock and Vibration Digest*, 36:197–205, 2004.

[18] H. Sodano, D. J. Inman, and G.Park. Generation and Storage of Electricity from Power Harvesting Devices. *Journal of Intelligent Material Systems and Structures*, 16:67–75, 2005.

[19] S. Roundy. On the Effectiveness of Vibration-based Energy Harvesting. *Journal of Intelligent Materials and Structures*, 16:809–823, 2005.

[20] Y. B. Jeon, R. Sood, J. H. Jeong, and S. G. Kim. MEMS Power Generator with Transverse Mode Thin Film PZT. *Sensors and Actuators A (Physical)*, 122:16–22, 2005.

[21] W. J. Choi, Y. Jeon, J. H. Jeong, R. Sood, and S. G. Kim. Energy Harvesting MEMS Device Based on Thin Film Piezoelectric Cantilevers. *Journal of Electroceramics*, 17:543–548, 2006.

[22] S. Roundy, E. S. Leland, J. Baker, E. Carleton, E. Reilly, E. Lai, B. Otis, J. M. Rabaey, P. K. Wright, and V. Sundararajan. Improving Power Output for Vibration-Based Energy Scavengers. *IEEE Pervasive Computing*, 4:28–36, 2005.

[23] H. B. Fang, J. Q. Liu, Z. Y. Xu, L. Dong, D. Chen, B. C. Cai, and Y. Liu. A MEMS-Based Piezoelectric Power Generator for Low Frequency Vibration Energy Harvesting. *Chinese Physics Letters*, 23:732–734, 2006.

[24] N. E. duToit and B. L. Wardle. Performance of Microfabricated Piezoelectric Vibration Energy Harvesters. *Integrated Ferroelectrics*, 83:13–32, 2006.

[25] N. duToit and B. Wardle. Experimental Verification of Models for Microfabricated Piezoelectric Energy Harvesters. *AIAA Journal*, 45:1126–1137, 2007.

[26] A. Erturk and D. Inman. A Distributed Parameter Electromechanical Model for Cantilevered Piezoelectric Energy Harvesters. *Journal of Vibration and Acoustics, Transaction of ASME*, 130:1–14, 2008.

[27] S. Roundy and Y. Zhang. Toward Self-Tuning Adaptive Vibration-Based Micro-Generators. In *Smart Materials, Nano- and Micro-Smart Systems*, Sydney, Australia, 2005.

[28] N. G. Stephen. On Energy Harvesting from Ambient Vibration. *Journal of Sound and Vibration*, 293:409–425, 2006.

[29] J. Renno, M. F. Daqaq, J. Farmer, and D. J. Inman. Parameter Optimization of a Vibration-Based Energy Harvester. In *Proceedings of the ASME International Design and Engineering Technical Conference, IDETC2007.*, Las Vegas, NV, 2007.

[30] T. Osorio and M. F. Daqaq. Effect of Bias Conditions on the Optimal Energy Harvesting Using Magnetostrictive Materials. In *Proceedings of the SPIE*, page 69280B, San Diego, CA, 2008.

[31] Z. Yang and J. Yang. Connected Vibrating Piezoelectric Bimorph Beams as a Wide-band Piezoelectric Power Harvester. *Journal of Intelligent Material Systems and Structures*, 20(5):569–574, 2009.

[32] B. P. Mann and N. D. Sims. Energy Harvesting from the Nonlinear Oscillations of Magnetic Levitation. *Journal of Sound and Vibration*, 319(1):515–530, 2009.

[33] J. M. Renno, M. F. Daqaq, and D. J. Inman. On the Optimal Energy Harvesting from a Vibration Source. *Journal of Sound and Vibration*, 320(1):386–405, 2009.

[34] R. Masana and M. F. Daqaq. Electromechanical Modeling and Nonlinear Analysis of Axially Loaded Energy Harvesters. *Journal of vibration and acoustics*, 133(1), 2011.

[35] L. Tang and Y. Yang. A Nonlinear Piezoelectric Energy Harvester with Magnetic Oscillator. *Applied Physics Letters*, 101(9):094102–094102, 2012.

[36] S. Zhou, J. Cao, A. Erturk, and J. Lin. Enhanced Broadband Piezoelectric Energy Harvesting Using Rotatable Magnets. *Applied Physics Letters*, 102(17):173901–173901, 2013.

[37] P. Mitcheson, E. Yeatman, K. Rao, S. Holmes, and T. Green. Energy Harvesting from Human and Machine Motion for Wireless Electronic Devices. *Proceedings of the IEEE*, 96:1457–1486, 2008.

[38] P. Lissaman. Low-Reynolds-Number Airfoils. *Annual Review in Fluid Mechanics*, 15:223–239, 1983.

[39] H. D. Akaydın, N. Elvin, and Y. Andreopoulos. Wake of a Cylinder: a Paradigm for Energy Harvesting with Piezoelectric Materials. *Experiments in Fluids*, 49(1):291–304, 2010.

[40] H. J. Jung and S. W. Lee. The Experimental Validation of a New Energy Harvesting System Based on the Wake Galloping Phenomenon. *Smart Materials and Structures*, 20(5):055022, 2011.

[41] A. Mehmood, A. Abdelkefi, M. R. Hajj, A. H. Nayfeh, I. Akhtar, and A. O. Nuhait. Piezoelectric Energy Harvesting from Vortex-Induced Vibrations of Circular Cylinder. *Journal of Sound and Vibration*, 2013.

[42] A. Barrero-Gil, G. Alonso, and A. Sanz-Andres. Energy Harvesting from Transverse Galloping. *Journal of Sound and Vibration*, 329(14):2873–2883, 2010.

[43] S. D. Kwon. A T-Shaped Piezoelectric Cantilever for Fluid Energy Harvesting. *Applied Physics Letters*, 97(16):164102–164102, 2010.

[44] J. Sirohi and R. Mahadik. Piezoelectric Wind Energy Harvester for Low-Power Sensors. *Journal of Intelligent Material Systems and Structures*, 22(18):2215–2228, 2011.

[45] H. D. Akaydin, N. Elvin, and Y. Andreopoulos. The Performance of a Self-Excited Fluidic Energy Harvester. *Smart Materials and Structures*, 21(2):025007, 2012.

[46] A. Abdelkefi, M. R. Hajj, and A. H. Nayfeh. Piezoelectric Energy Harvesting from Transverse Galloping of Bluff Bodies. *Smart Materials and Structures*, 22(1):015014, 2013.

[47] Y. Yang, L. Zhao, and L. Tang. Comparative Study of Tip Cross-Sections for Efficient Galloping Energy Harvesting. *Applied Physics Letters*, 102:064105, 2013.

[48] L. Tang, M. P. Païdoussis, and J. Jiang. Cantilevered Flexible Plates in Axial Flow: Energy Transfer and the Concept of Flutter-mill. *Journal of Sound and Vibration*, 326(1):263–276, 2009.

[49] A. Erturk, W. G. R. Vieira, C. De Marqui, and D. J. Inman. On the Energy Harvesting Potential of Piezoaeroelastic Systems. *Applied Physics Letters*, 96(18):184103–184103, 2010.

[50] C. De Marqui, A. Erturk, D. J. Inman, et al. Piezoaeroelastic Modeling and Analysis of a Generator Wing with Continuous and Segmented Electrodes. *Journal of Intelligent Material Systems and Structures*, 21(10):983–993, 2010.

[51] M. Bryant and E. Garcia. Modeling and Testing of a Novel Aeroelastic Flutter Energy Harvester. *Journal of vibration and acoustics*, 133(1), 2011.

[52] A. Abdelkefi, A. H. Nayfeh, and M. R. Hajj. Modeling and Analysis of Piezoaeroelastic Energy Harvesters. *Nonlinear Dynamics*, 67(2):925–939, 2012.

[53] A. Abdelkefi, J. M. Scanlon, E. McDowell, and M. R. Hajj. Performance Enhancement of Piezoelectric Energy Harvesters from Wake Galloping. *Applied Physics Letters*, 103(3):033903, 2013.

[54] K. Wardhana and F. C. Hadipriono. Study of Recent Building Failures in the United States. *Journal of Performance of Constructed Facilities*, 17(3):151–158, 2003.

[55] J. W. Kim, H. Takao, K. Sawada, and M. Ishida. Integrated Inductors for RF Transmitters in CMOS/MEMS Smart Microsensor Systems. *Sensors*, 7, 2007.

[56] N. Elvin, N. Lajnef, and A. Elvin. Feasibility of Structural Monitoring with Vibration Powered Sensors. *Smart Materials and Structures*, 15:977–986, 2006.

[57] T. Galchev, J. McCullagh, R. L. Peterson, and K. Najafi. Harvesting Traffic Induced Bridge Vibrations. In International Solid-State Sensors. *Actuators and Microsystems*, pages 1661–1664, 2011.

[58] A. H. Nayfeh and P. F. Pai. *Linear and Nonlinear Structural Mechanics*. Wiley.com, 2008.

[59] G. V. Parkinson and N. P. H. Brooks. On the Aeroelastic Instability of Bluff Cylinders. *Journal of applied mechanics*, 28:252, 1961.

[60] D. M. Tang, H. Yamamoto, and E. H. Dowell. Flutter and Limit Cycle Oscillations of Two-Dimensional Panels in Three-Dimensional Axial Flow. *Journal of Fluids and Structures*, 17(2):225–242, 2003.

[61] L. Tang and M. P. Paidoussis. On the Instability and the Post-Critical Behaviour of Two-Dimensional Cantilevered Flexible Plates in Axial Flow. *Journal of Sound and Vibration*, 305(1):97–115, 2007.

[62] J. M. Kluger, F. C. Moon, and R.H. Rand. Shape Optimization of a Blunt Body Vibro-Wind Galloping Oscillator. *Journal of Fluids and Structures*, 40:185–200, 2013.

[63] M. P. Païdoussis, S. J. Price, and E. De Langre. *Fluid-Structure Interactions: Cross-Flow-Induced Instabilities*. Cambridge University Press, 2011.

[64] M. Abramowitz and I. A. Stegun. *Handbook of Mathematical Functions: with Formulas, Graphs, and Mathematical Tables*. Number 55. Courier Dover Publications, 1972.

[65] M. Novak. Aeroelastic Galloping of Prismatic Bodies. *ASCE Journal of the Engineering Mechanics Division*, 96:115–142, 1969.

[66] L. Liu, Y. S. Wong, and B. H. K. Lee. Application of the Centre Maniflod Theory in Non-linear Aeroelasticity. *Jounal of Sound and Vibration*, 234:641–659, 2000.

[67] Y.C. Fung. *An Introduction to the Theory of Aeroelasticity*. Wiley, New York, 1955.

[68] A. H. Nayfeh. *The Method of Normal Forms*. Wiley-VCH, New York, 2nd edition, 2011.

[69] M. Bryant, E. Wolff, and E. Garcia. Aeroelastic Flutter Energy Harvester Design: the Sensitivity of the Driving Instability to System Parameters. *Smart Materials and Structures*, 20(12):125017, 2011.

[70] J. Carr. *Applications of Center Manifold Theory*. Springer Verlag, New York, 1981.